EFFECT OF PROCESSING ON THE BEHAVIOUR OF LAMINATED COMPOSITE STRUCTURES: A NUMERICAL AND PROBABILISTIC APPROACH

by

ABDUL RAHIM AHAMED ARAFATH

B.Sc. (Civil Engineering), University of Peradeniya, Sri Lanka, 1998

A THESIS SUBMITTED IN PARTIAL FULFILMENT OF

THE REQUIREMENTS FOR THE DEGREE OF

MASTER OF APPLIED SCIENCE

in

THE FACULTY OF GRADUATE STUDIES

(Department of Civil Engineering)

We accept this thesis as conforming
to the required standard

THE UNIVERSITY OF BRITISH COLUMBIA

February 2002

In presenting this thesis in partial fulfilment of the requirements for an advanced degree at the University of British Columbia, I agree that the Library shall make it freely available for reference and study. I further agree that permission for extensive copying of this thesis for scholarly purposes may be granted by the head of my department or by his or her representatives. It is understood that copying or publication of this thesis for financial gain shall not be allowed without my written permission.

Department of _Civil Engineering_

The University of British Columbia
Vancouver, Canada

Date _Feb, 20th 2002_

ABSTRACT

The manufacturing of composite structures made of fibre-reinforced thermoset matrix materials generally results in residual stress build-up during the curing process. As a consequence, the precise geometry and material properties of the final structure after tool (mould) removal are often difficult to control. To account for such process-induced variations, engineers either have employed empirical knockdown factors, which are determined experimentally for a range of distinct structures, materials and manufacturing processes or have incorporated the measured variations as input into sophisticated finite element analyses. The first approach may lead to an unconservative design while the second approach is not suitable for normal design practice.

In this study, a combined deterministic-stochastic simulation approach is presented to demonstrate the manner in which manufacturing-induced variabilities in composite structures can be controlled to achieve targeted reliability levels in structural performance. A finite element code, COMPRO, which deterministically simulates the various physical phenomena during manufacturing of composite structures, is integrated with non-linear structural analysis and reliability analysis to compute the statistics of the parameters that must be controlled at the manufacturing level in order to result in an optimum or reliable structural performance during service. The methodology is demonstrated through a case study that examines the buckling behaviour of a composite plate in the presence of manufacturing-induced imperfections.

The intrinsic and extrinsic process parameters that affect the dimensional stability of more complex composite structures such as L- and C-shaped angular laminate sections, are

numerically investigated using COMPRO. The predictive capability of COMPRO is examined by comparing the simulation results with available experimental measurements.

Finally, to account for all sources of residual stress build-up required for accurate assessment of failure, the micro-level stresses arising from the mismatch between the coefficient of thermal expansions of the fibre and the matrix and the matrix cure shrinkage are computed through micromechanical finite element analysis of a representative volume of the fibre and the matrix. The ply- and laminate-level residual stresses computed by COMPRO during the curing process are then transferred to the micro-level using suitably derived stress magnification factors.

TABLE OF CONTENTS

LIST OF TABLES

LIST OF FIGURES

ACKNOWLEDGEMENTS

CHAPTER 1: INTRODUCTION

1.1 BACKGROUND

Fibre-reinforced plastic composite materials are replacing traditional ones in many of today's structural engineering applications. When using composites, unlike their metallic counterparts, the complete (large-scale) structure is manufactured from the raw materials in one step. Our focus is high-performance structural components made of advanced thermoset matrix composites typically employed in the aerospace industry. An autoclave process is commonly used to manufacture such structures. Broadly speaking, this process involves stacking of pre-impregnated sheets of unidirectional fibres (commonly called prepreg) at various orientations over a tool of desired shape and then subjecting the whole assembly to a controlled cycle of temperature and pressure inside an autoclave. The process results in the compaction and curing of the composite part. However, because of the residual stresses that build up during the process, the precise shape and dimensions of the final part after tool removal are often difficult to control. In thin-walled composite structures spring-back and warpage are commonly observed process-induced imperfections. In addition to the detrimental effect on the dimensional accuracy, process-induced residual stresses are also critical to the performance of the manufactured parts. Sometimes, the residual stresses are so severe that transverse matrix cracks and delaminations are introduced within the component after processing, and the parts fail earlier than expected. Therefore, the manufacturing process and its consequences on the material and geometrical properties of the final structure must be taken into account when considering the response to, and reliability under, the applied loads. Otherwise, the designer of composite structures is forced to

use empirical safety factors, which may result in a conservatism that, in many cases, nullifies the benefits that are offered by composite materials.

There has been work done to develop more sophisticated analytical and numerical models to predict the residual stress development in cured composite parts. These models range from one-dimensional analysis (Loos et al., 1983), two-dimensional analysis (Bogetti et al., 1992), to three-dimensional analysis (Chen et al., 1988). In the same front, a comprehensive, multi-physics, 2D finite element code, COMPRO, has been developed to analyze industrial autoclave processing of composite structures of intermediate size and complexity. The model caters for a number of important processing parameters and the development of residual stress and deformation. This model advances previous work by other researchers and, in addition, accounts for the effects of tool/part interactions, which have been neglected by other investigators. The model assumptions, theoretical background, solution strategies and case studies demonstrating its predictive capabilities have been documented in a recent article by Johnston et al (2001). A brief review of the software will be given in Section 1.2.

Historically, engineers have employed empirical knockdown factors to account for the large discrepancies between experimentally measured loads and analytical values due to the presence of geometric imperfections. Knockdown factors are often determined experimentally for a range of distinct structures, materials, and manufacturing processes. But these knockdown factors should be constantly updated to include new experimental results. A more sophisticated approach to determine the knockdown factors is the use of finite element analysis with experimentally measured imperfections as input (Starnes, 1999, Li et al, 1995). However, these approaches depend on availability of experimental measurements for a given processed

composite part and therefore cannot be used in a general manner to study the effect of imperfections on structural behaviour.

Up to the present time, little work has been done on modelling of the composite processing and incorporating the process effects into the structural analysis and design. Furthermore, these manufacture-induced phenomena cannot be accounted for in the current so-called "building block approach" to design of composite structures, where the behaviour and properties of the final, full-scale structure are estimated from smaller scale coupon tests and sub-structure analyses. The objective of this work is to present a computational framework for analysing the complete sequence of events from the manufacturing stage to the in-service structural performance of a composite structure.

There are many input process parameters that influence, to various degrees, the outcome of the manufacturing, influencing, in turn, the structural performance. Many of these parameters have inherent stochastic variability that result in uncertainty in the final part geometry and material properties. By coupling *stochastic* and *deterministic* computational models of the physical events one can study the effect of those variabilities as they propagate through the various stages of the analyses, and eventually influence the response of the composite structure to in-service loading. This would ultimately allow process variables to be controlled or manipulated at the outset (manufacturing level) to result in an optimum or reliable structural performance during service. In this study, we present how process-induced uncertainties can be included in the analysis of composite structures and how the processing parameters can be controlled to achieve a certain reliability level in structural performance. The deterministic process simulation software, COMPRO, the commercial structural analysis software, ABAQUS, and the inverse reliability software, IRELAN, are used here to determine the process parameters that must be controlled to

meet structural performance standards with target reliabilities. In the following section, a brief review of the two software packages developed at UBC, COMPRO and IRELAN, and used in this study is given.

1.2 SOFTWARE TOOLS USED IN THIS STUDY

1.2.1 COMPOSITE PROCESS MODELLING SOFTWARE – COMPRO

In this section, a brief review of the software used in this study to simulate the autoclave processing of a composite structure is given. A more detailed description of the software can be found in Johnston (1997).

A modular approach, first introduced by Loos and Springer (1983), is adopted for process modelling. As illustrated in Figure 1.1, using this approach, the problem is divided into a series of 'sub-models', or 'modules', each responsible for performing a related set of tasks such as prediction of temperature and resin degree of cure etc. Coupling between these modules is maintained by solving each in sequence as the solution marches forward in time. In this way, the predictions of one module can be used by another. A brief description of each module is given below:

1. *Autoclave Simulation* Module: At the beginning of each time step, this module simulates the automated autoclave control and response and updates all autoclave environmental variables including autoclave air temperature and pressure, and vacuum bag pressure.

2. *Thermochemical* Module: This module is responsible for calculation of temperature in the structure of interest and the modelled tooling as well as the degree of cure in composite component.

3. *Flow* Module: This module uses a percolation model to predict resin flow and fibre bed compaction in composite components (see Hubert, 1996).

4. *Stress* Module: This module is responsible for modelling the internal stresses and stress-induced deformations developed within a component during the processing. Through integration of this module with analyses of component temperature and resin degree of cure (thermochemical module) and resin flow and fibre bed compaction (flow module), this model can examine all five major sources of process-induced stress and deformation identified in the literature (Johnston, 1997). These are:

   i.   Thermal expansion

  ii.   Resin cure shrinkage

 iii.   Gradients in component temperature and resin degree of cure

  iv.   Resin pressure gradients (resulting in resin flow)

   v.   Mechanical constraints due to tooling

5. *Input* Module: controls acquisition of all input parameters required for a program run. This may include translation of the problem finite element description from an external preprocessor to a form used internally by COMPRO.

There are 8 input files that a user has to specify:

Batch file: Contains a list of all projects to be run in a batch.

Project file: contains a list of the input files containing the project description.

Finite element description file: contains the finite element description (node, element, region, boundary etc.) of the problem.

Boundary and initial condition specification file: contains specification of all model boundaries (thermochemical, stress and flow) and initial conditions (initial temperature, initial resin degree of cure).

Program control data files: contain all information used by COMPRO to control its internal operation including modules to be executed, time step control data, output time intervals, etc.

Process cycle definition files: contain all information related to specification of the autoclave process cycle including controller specifications, virtual instruments, etc.

Lay-up definition files: contain ply lay-up specification information for all composite material regions.

Material identification files: contain the identification names of the materials in each model region.

6. *Output* Module: controls output of all parameters to external devices, for example, to the screen and hard drive.

All three major solution modules (thermochemical, flow and stress/deformation) employ the finite element method to solve for the component state variables during processing. The component finite element description can be created using virtually any finite element pre-processor which can generate an output text file.

Element Type

The previous version of COMPRO employed four-noded isoparametric quadrilateral elements as shown in Figure 1.2a. The new version of COMPRO can employ both four-noded and eight-noded isoparametric quadrilateral elements as shown in Figure 1.2b. For the eight-noded

analysis, the user only needs to define the four-noded finite element mesh. COMPRO internally converts the four-noded elements to eight-noded elements (Osooly, 2001).

Region Definition

In COMPRO, a region is defined as a collection of elements containing a single type of material. In addition to defining element material type, regions are used in combination with reference boundaries (next section) to define ply lay-up and element local axes orientation. Regions are also used to define which elements represent process tooling, usually removed at the end of the processing cycle, and which are part of the composite structure (whether specifically defined as composite materials or not).

To minimize the number of elements required to discretize a given problem, multiple plies of any orientation may be contained within each composite material element as shown in Figure 1.3. It is not required that a whole number of plies be contained within an element (e.g., a ply can contain 2.6 plies), but the ply plane must be parallel to the element local coordinate x'-axis. Ply orientation is defined according to the right-hand rule with the angle measured from the positive x' axis. Ply lay-up in a region is defined with respect to the reference boundary for that region (i.e. ply 1 starts at the reference boundary).

Boundary Definition

In COMPRO, a boundary is defined by node groups (never by element 'faces' as in some finite element codes). Boundaries are used for three main purposes: to specify 'boundary conditions' (e.g. heat flux, vacuum pressure), for definition of ply lay-up, and for definition of the element local axes orientation as shown in Figure 1.4.

Material Property Definition

Each time a module is run, the relevant material properties for each element are recalculated from state variable values (e.g., temperature, degree of cure and volume fraction) at the element centroid. Orthotropic material behaviour is assumed in all cases. Orthotropic composite properties may be either specified directly or calculated from micromechanics models which use as input fibre volume fraction, isotropic resin properties and transversely isotropic fibre properties. All materials are assumed to be 'instantaneously linear elastic'. This means that, although the modulus may not be constant during processing, at any given instant (i.e., during any time step), they exhibit linear elastic behaviour.

Virtual Autoclave Simulation

Virtual autoclave simulation is one of the main special features of COMPRO. The autoclave simulation includes the simulation of the behaviour of the autoclave during processing including all environmental control hardware (i.e. heating, cooling, pressurizing etc.).

Tool Part Interaction

The amount of stress transferred between the tool and the part is controlled by including a thin elastic shear-layer into the finite element mesh. Depending on the value of the elastic modulus assigned to the shear layer, a range of tool part interface conditions can be simulated. At the one extreme, if the properties of the shear layer are the same as the tooling, high shear stresses arise between the tool and the part (perfect bonding). At the other extreme, by giving the shear layer low values for E_{11} and G_{13} (i.e. longitudinal Young's modulus and transverse shear modulus),

relatively little stress is transferred between the tool and the part. The shear layer is considered to be part of the tooling and it is removed during the final tool removal step.

Tool Removal Simulation

At the end of the process cycle, a simulation of the tool removal from the component is performed to determine post-processing component shape. The tool removal simulation is performed in a single elastic step and the calculated changes in displacements are added to the pre-tool-displacements to give the final component shape.

1.2.2 INVERSE RELIABILITY ANALYSIS SOFTWARE – IRELAN

In this section, a brief review of the theory behind the inverse reliability analysis software IRELAN is given. The software was developed in the Department of Civil Engineering, at UBC. A more detailed description of the software can be found in Foschi and Li (1999b).

In combination with an analytical model for the system, safety assessment requires *forward reliability methods* for estimating the reliability or the probability that it will perform as intended. On the other hand, engineering design requires an *inverse reliability approach* of determining the design parameters to achieve pre-specified target reliabilities. In general, an inverse problem involves finding either a single design parameter to achieve a given single reliability constraint or multiple design parameters to meet specified multiple reliability constraints.

Forward Reliability Method

The implementation of the reliability analysis is based on a description of the limit state of interest by a performance function $G(x)$ as follows:

$$G(\boldsymbol{x}) = G(x_1, x_2, ..., x_n) \tag{1.1}$$

where the $\boldsymbol{x} = (x_1, x_2, ..., x_n)^{\mathrm{T}}$ is an n-dimensional vector of intervening random variables. Some of these may affect the demand on the system, denoted by D, while the others may influence the system capacity C to withstand the demand. By convention, the performance function (Equation 1.1) may be written as

$$G = C - D \tag{1.2}$$

Thus, the system will not perform as intended (failure) if the combination of the intervening random variables results in $G < 0$. The corresponding probability of such event (Prob($G < 0$)) is then called the probability of failure. Conversely, the combination of the intervening random variables resulting in $G > 0$ will make the system perform as required (survival) and the corresponding probability (Prob($G > 0$)) is termed the reliability. The situation $G = 0$ is a limit-state between failure and survival and the corresponding surface, $G(\boldsymbol{x}) = 0$, is called the limit-state failure surface. Since, in general, there could be a number of random variables involved in G, the exact calculation requires the joint probability density function of all random variables and integration over the failure region $G < 0$,

$$P_f = \int\limits_{G<0} f_{123...n}(x_1, x_2, ...x_n)dx_1 dx_2 ...dx_n \tag{1.3}$$

However, this exact approach can hardly be applied since the joint probability function f is unknown and very difficult to find. An alternative method is the straightforward, standard computer simulation (Monte Carlo method) which is simple to implement and can converge to the exact solution. However, it could be very computationally demanding, especially when dealing with a low probability of failure. To overcome this, different methods have been

proposed to increase the simulation efficiency such as importance sampling, adaptive important sampling, etc. Both the importance sampling technique and the adaptive importance sampling technique concentrate on sampling points in the region which mainly contributes to the failure probability, instead of spreading them out evenly across the whole range of possible values of each random variable.

A second alternative is the use of approximate methods that have been developed during the last three decades, such as the FORM/SORM procedures (First Order or Second Order Reliability Methods), and which are based on the calculation of the reliability index β ($\beta = \mu_G / \sigma_G$ where μ_G and σ_G are the mean and standard deviation of the G function). From this index, by use of the Standard Normal probability distribution function $\Phi(\ )$, the probability of failure P_f and the reliability P_r can be estimated approximately

$$P_f = \Phi(-\beta) \tag{1.4}$$

and

$$P_r = 1 - \Phi(-\beta) = \Phi(\beta) \tag{1.5}$$

A forward reliability software, called RELAN was developed to carry out a variety of reliability calculations (Foschi, et al., 1999a).

FORM/SORM Procedure

These methods are the most complex, both mathematically and conceptually, among all probabilistic analysis methods and will therefore not be described in detail. More details of these methods can be found in Li (1999).

The approach of these methods is to transform the integral given in Equation 1.3 to an approximately equal integral that can be efficiently evaluated. This is done in the following step-by-step procedure:

1. Transform the design variable into standard normal distributions. That is, transform $G(x)$ = 0 into $G(u)$ = 0 where u is a vector of independent standard normal variables.

2. Identify the most probable point or design point. For a given limit state function, the main contribution to failure probability comes from the region where G is closest to the origin in the transformed design variable space (u-space). The design point is the closest point to the origin in the transformed space (Figure 1.5).

3. Develop a polynomial approximation to the performance function (G) around the design point (linear function in FORM and quadratic function in SORM). Compute the probability of failure using the newly defined G – function.

Response Surface Method

For complex structures, the performance function is not available as an explicit function of the random design variables. The performance of the structure can only be evaluated numerically through a structural analysis procedure such as the finite element method. The goal of the response surface methodology (RSM) is to find a predictive equation (such as Equation 1.6) relating a response to a number of input variables.

$$G_R(x) = a + \sum_{i=1}^{n} b_i x_i + \sum_{i=1}^{n} c_i x_i \qquad (1.6)$$

where x_i, (i = 1,......,n) are the basic variables and the parameters a, b_i, c_i, (i = 1, ...,n) are to be found. Then this equation can be used to determine the response to given values of input variables, instead of having to repeatedly run the time-consuming deterministic structural analysis.

Inverse Reliability Method

The objective of the inverse procedure is to find, directly, the design vector, d, so that the target reliability level corresponding to each specified limit state would be satisfied. In general, these are also regarded as random variables, with corresponding mean values and standard deviations. The problem may include the determination of the mean alone when the coefficients of variation are specified, the standard deviations when the means are given, or both means and standard deviations. The inverse reliability problem can be solved by trial and error by repeating forward reliability analyses such as FORM/SORM, interpolating the design parameters being sought. This is inefficient and time consuming, especially when multiple design parameters and multiple reliability constraints are involved. To approach the inverse reliability problem directly, an efficient method based on FORM/SORM methods is proposed by Foschi and Li (1999b). For cases requiring an intensive computational effort or having a non-smooth limit state function, a response surface method for inverse analysis is also proposed and implemented to speed up the calculations.

Performance-Based Probabilistic Design

This is a newly added feature to the IRELAN software based on the neural network method. A full detail of this feature is given in Foschi and Li (2000). A brief review is given in this section.

Performance-based design of a structural system implies the definition of a set of limit states or performance requirements, with corresponding target reliabilities for each state.

$$G_n(x_i, d) = 0 \text{ with target reliability } \beta_n \tag{1.7}$$

With these requirements, the designer must consider the uncertainty in the intervening variables, *x*, and calculate values for specific design parameters, *d*, to achieve the desired reliabilities, *β*. For multiple performance criteria, the problem may not have an exact solution, since the target reliabilities for each limit state may not be all achieved as prescribed. In this case, an optimization procedure is used to minimize the difference between the achieved reliabilities and the corresponding targets reliabilities (Equation 1.8).

$$\Psi = \sum_{j=1}^{NP} \left(\beta_j^T - \beta_j(d) \right)^2 \tag{1.8}$$

where Ψ is the objective function to be minimized, β_j^T is the target reliability corresponding to the jth limit state, and $\beta_j(d)$ is the reliability index obtained with the design parameter *d*.

This approach requires, for the given performance criteria and associated target reliability levels, the determination of a set of design parameters. This can be achieved using any of the inverse methods discussed in Foschi and Li (1999b).

When the response is highly non-linear, the convergence and the robustness of procedure like FORM will be adversely affected. So, this software uses simulation technique (importance sampling technique or adaptive sampling technique) following the calculation of a design point using FORM on an approximate quadratic response surface. The required evaluation of the

performance function is carried out with a local interpolation using a response database obtained independently through deterministic analysis.

1.3 RESEARCH OBJECTIVE AND SCOPE OF THESIS

The objective of this research is twofold.

1) To present the effect of process-induced stresses and deformations on structural performance.

2) To present a computational framework for analysing the complete sequence of events from the manufacturing stage to the in-service structural performance of a composite structure, while taking into account the stochastic nature of the parameters involved. In this case, we combine a deterministic model for the manufacturing process and structural analysis with a probability-based reliability model to determine the process parameters that must be controlled to meet structural performance standards with target reliabilities.

The deterministic process simulation software, COMPRO, the commercial structural analysis software, ABAQUS, and the inverse reliability software, IRELAN, are used for the analysis.

The research presented in this thesis is organized as follows:

1) Chapter 2 – A case study is presented to illustrate the processing effects on structural performance and the probability approach to determine the manner in which processing variables can be controlled to meet structural performance standards with target reliabilities.

2) Chapter 3 – The effect of various parameters on spring-in of curved composite parts are predicted numerically using COMPRO and, where possible, compared with experimental

data. The case study considered, that of L- and C-shaped composite parts, serve to demonstrate the range of process parameters that have to be taken into account for more complex shaped composite structures.

It also highlights the advantages of having a numerical model that can capture the effects of many of these parameters in a virtual manufacturing environment. Such detailed quantitative information on a processed part can then easily be transported to a structural analysis program as input, thereby accounting for processing effects in assessment of structural performance.

3) Chapter 4 – The residual stress development during the curing process both at the ply level and the micro-level due to CTE mismatch and cure shrinkage are quantified. The ability to compute these residual stresses at all level is vital for subsequent failure analysis of composite structures.

4) Chapter 5 – Conclusion and future work.

1.4 FIGURES
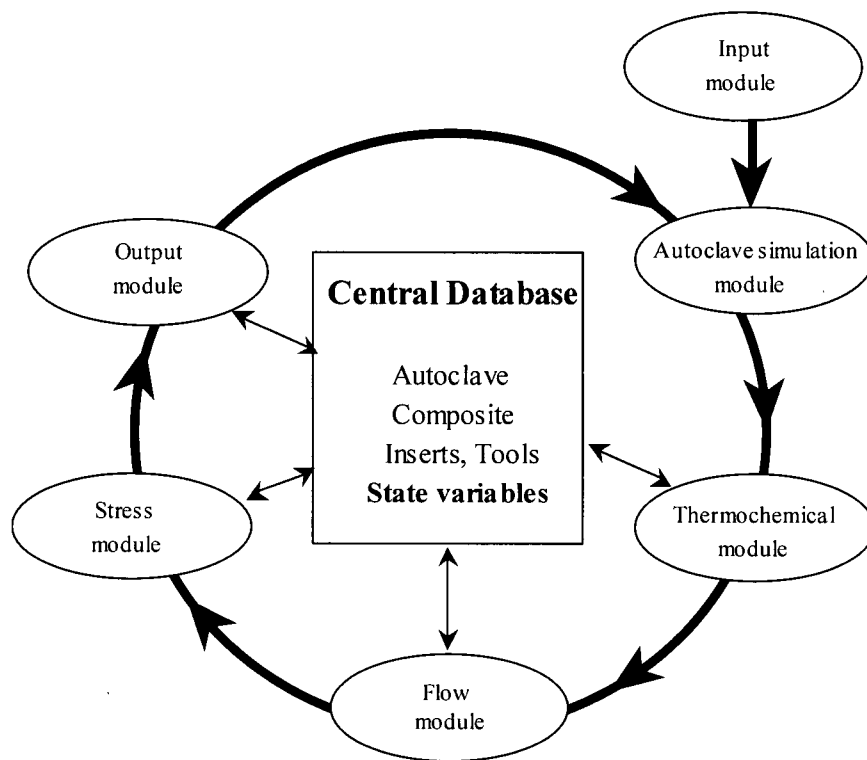
Figure 1.1: Schematic of COMPRO structure and program flow (Johnston, 1997).

(a)

(b)
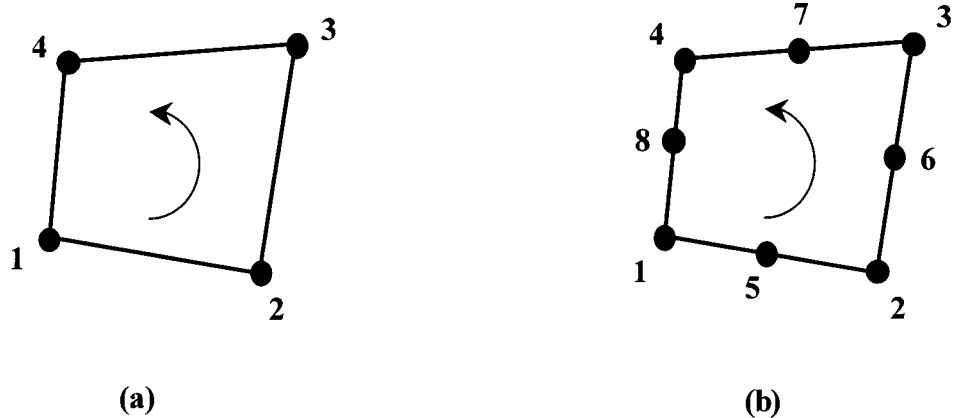
Figure 1.2: Four-noded and eight-noded isoparametric quadrilateral elements employed in COMPRO.
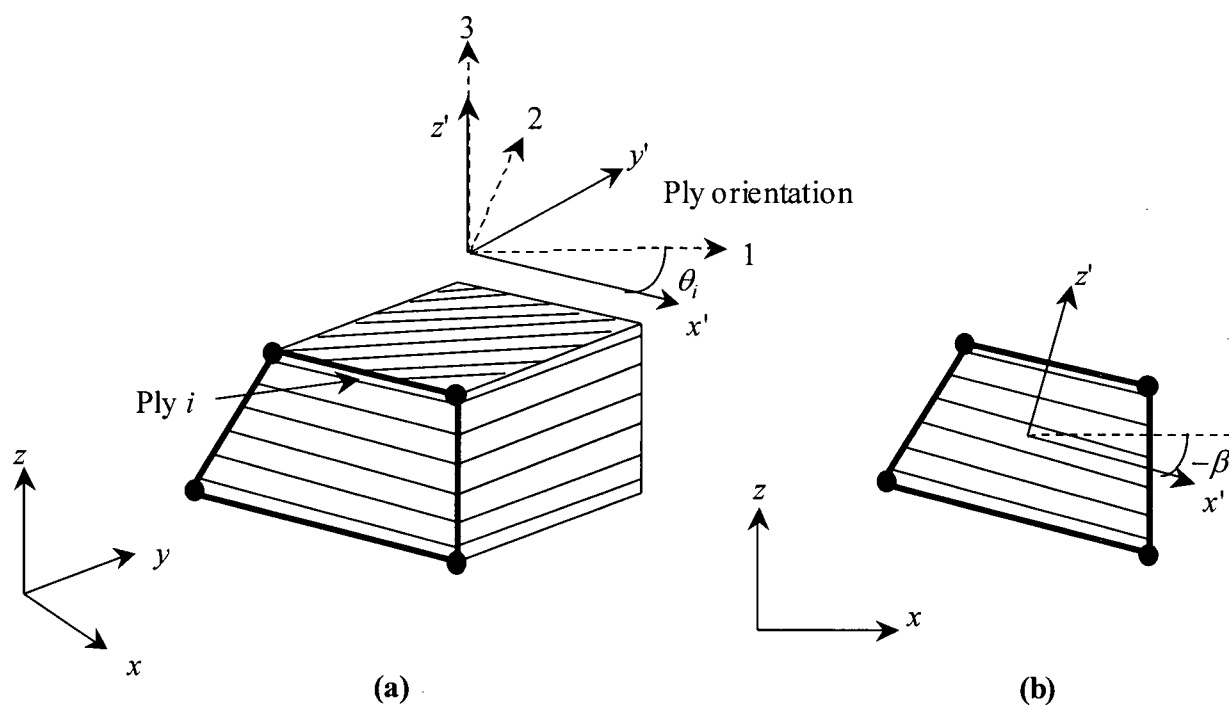
Figure 1.3: Composite element (a) isometric view (b) 2D view (orientation of element local axis is also shown) (Johnston, 1997).
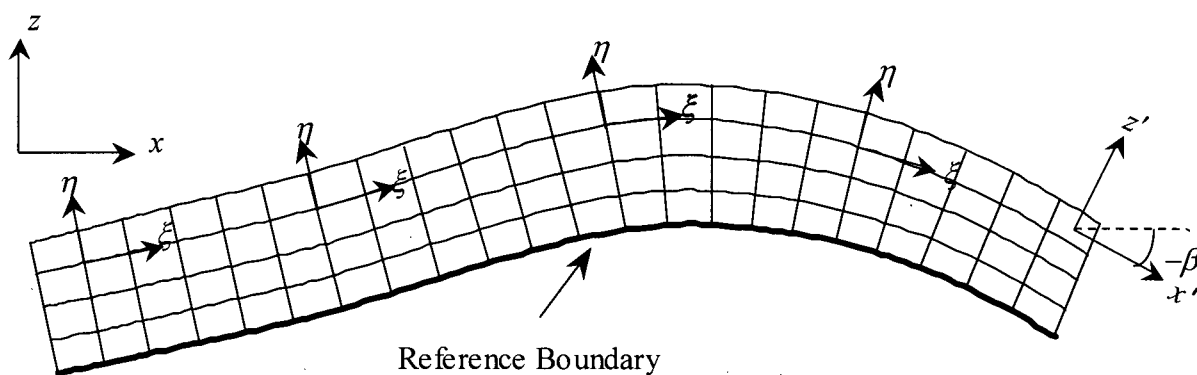
Figure 1.4: Curved region, showing element local coordinates, local axes orientation and the region reference boundary (Johnston, 1997).
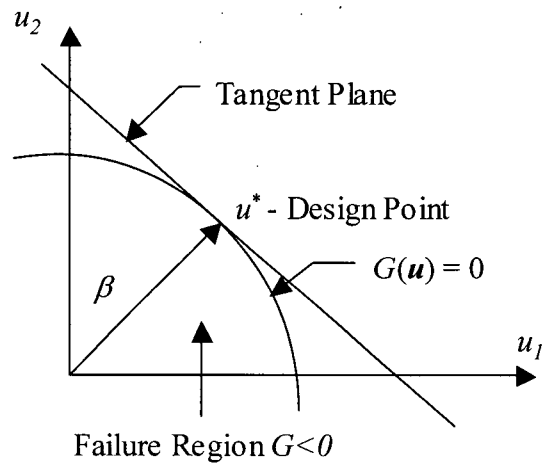
Figure 1.5: Geometric representation of reliability calculation for FORM (Li, 1999).

CHAPTER 2: PROBABILISTIC DESIGN OF A COMPOSITE PLATE AGAINST BUCKLING

2.1 INTRODUCTION

The basic structure of an aircraft is made of three types of elements: shells, plates, and beams (stiffeners). The fuselage of the aircraft is made of stiffened shells and the top and bottom surface of the wings are made of stiffened plates as shown in Figure 2.1. The major design goal is to produce a light structure which is strong enough to withstand the aerodynamic loads. Since the skins on the wings and the fuselage of an aircraft are fairly thin due to the weight requirement, their likely mode of failure under the aerodynamic loading is buckling.

The traditional way of designing a thin-walled metallic structure against buckling is to determine the buckling load by a simple deterministic analysis and to reduce this buckling load by a knockdown factor. This knockdown factor is to account for the difference between the predicted buckling load and the actual buckling load measured from a test (Starnes et al, 1999). A linear bifurcation analysis is often used for this deterministic analysis on a geometrically perfect shell structure with the nominal values of material properties and idealized boundary conditions. A simply supported boundary condition is often used to simplify the analysis and because of its relatively low structural stiffness it is also the worst case scenario.

The fabrication process generally introduces initial imperfections in metallic shell structures and accounts for the difference between the predicted and actual buckling load. The effect is

particularly severe when the imperfection shape coincides with the buckling mode of the structure (Chryssanthopoulos et al, 1995).

The current practice of incorporating the initial imperfection into the design is to include the measured imperfection data in the analysis if these data are available or to include some approximate imperfection shape function if these data are not available (Starnes et al, 1999). For a prototype, the imperfection can be measured experimentally and then can be incorporated into the theoretical analysis to predict the buckling load. But in normal production runs, this approach is impractical due to variability in manufacturing methods, material properties etc. The realization that any further advances towards more accurate buckling load predictions of thin shells depend on the availability of extensive information about realistic imperfections data and their correlation with manufacturing processes has led to the establishment of an International Imperfection Data Bank for metallic structures (Arbocz, 1991). In this data bank, the characteristic initial imperfection distribution that a given fabrication process is likely to produce is established and then this information is combined with some kind of statistical analysis of both the initial imperfection and the corresponding critical buckling load.

In recent past, metallic thin-walled structures have been replaced by composite structures, especially in high-performance aerospace structural applications, due to their superior specific strength and stiffness. Compared to its metallic counterparts, the analysis of a composite shell structure becomes more complex due to the complex nature of its manufacturing process and the high variability of their material properties. Due to a variety of uncertainties that are involved in fabrication of composite panels, it is impossible to determine the amplitude and the shape of imperfection. The traditional knockdown factor design approach will not be conservative if the composite shell structural behaviour is not fully understood and the traditional sources of design

knockdown factors for predicting shell buckling loads do not include data for composite shell structures (Starnes et al., 1999). The effects of traditional initial geometric shell-wall imperfections on the buckling response of unstiffened thin-walled graphite-epoxy cylindrical shells is analysed by Starnes et al. (1999) in which the initial geometrical imperfections and the thickness variations are experimentally measured and incorporated in non-linear structural analysis. As mentioned earlier, the above approach is impractical in normal production runs.

The best way to handle the above problem is to model the manufacturing process of the composite structures in order to predict the processing imperfection accurately and to combine this process model with structural analysis codes. To this end, a two-dimensional finite element code, COMPRO, has been developed by the Composites Group at the University of British Columbia for modelling the autoclave processing of complex composite structures (Johnston et al., 2001). In addition to the complexity of this manufacturing process, variability of composite structures at both the material and the processing level are important and need to be considered. Handling these uncertainties in the traditional knockdown factor method normally leads to an overly conservative or unconservative design.

The probabilistic design approach is an alternative to the traditional knockdown factor approach to account for the uncertainties. In the literature, many probabilistic based design approaches are proposed to account for the uncertainties involved in material and manufacturing levels (Shiao et al., 1999; Elseifi et al, 1999; Cederbaum et al, 1996). All these probabilistic methods are used to analyse the reliability of the composite structures for the given uncertainties at the material and manufacturing levels. But in actual design practice, we need to solve the inverse problem i.e. for the given reliability targets, the material properties and the processing condition should be found

with certain statistical distribution. For this purpose, Foschi and Li (1999b) have developed a probabilistic design software, IRELAN, which can handle the inverse problem.

The acceptable probability of failure is the criterion that is used to determine whether the design is acceptable. Legal, technical and socio-economic considerations are involved in deciding this target reliability level. It should not be decided by the engineer performing the probabilistic analysis rather it should be specified by the agency certifying the structure. The target reliability level for aircraft structure is generally very high and this issue remains unresolved at the present time (Long and Narciso, 1999).

In performance-based design of a structural system, the design parameters should be calculated to meet one or more performance requirements with specified target reliabilities. For this multiple performance criteria, the problem may not have an exact solution, since the target reliabilities for each limit state may not be achieved as prescribed. An optimization procedure is proposed by Foschi and Li (2000) in which the difference between the achieved reliabilities and the corresponding targets are minimized.

In this case study, a combined deterministic-stochastic simulation approach is presented to demonstrate the manner in which manufacturing-induced variability in composite structures can be controlled to achieve targeted reliability levels in structural performance. The processing finite element code, COMPRO, is integrated with the non-linear structural analysis and reliability analysis software to compute the statistics of parameters that must be controlled at the manufacturing level in order to achieve an optimum structural performance during service. In the literature, thin-walled composite panels are identified as highly sensitive to geometric imperfections. For illustrative purposes, the buckling behaviour of a composite plate in the

presence of process-induced residual stresses and deformations is examined. Since process modelling is not an established source and research is still being carried out in this area, we have chosen this relatively simple problem for which a large body of experimental results have already been generated at UBC. These results serve as a validation of the process modelling undertaken here and therefore ensure confidence in using the output of the process model as input for structural modelling and reliability analysis. Buckling is a potential failure mechanism for thin-walled structural components commonly employed in aircraft structures.

2.2 PROBLEM DEFINITION

A unidirectional, carbon fibre-reinforced plastic (CFRP) composite laminate with a span of 1200 mm, a width of 100 mm and a thickness of 1.6 mm (consisting of 8 plies each of thickness 0.2 mm) is considered for this study. This is the most slender of many geometries of flat plates studied experimentally by Twigg (2001). The plate is manufactured in an autoclave under the temperature and pressure cycle shown in Figure 2.2 on an aluminum tool. In the ideal case, the plate is assumed to be straight and stress free and therefore there is no deformation prior to buckling. But in reality, due to processing, various stresses and deformations are induced in the structure. The resulting initial imperfection affects the lateral response of the plate when subjected to a certain axial compressive load (Figure 2.3).

The amount of the initial imperfection may depend on many processing parameters such as curing temperature, pressure, heating rate, cooling rate, holding period, fibre volume fraction etc. Some of these parameters are more influential than others. Practically, it is impossible and costly to keep all these processing parameters constant. In this design problem, first, the processing parameters that the imperfections are most sensitive to are identified and then the variability of

these processing parameters are found so that the plate withstands the applied axial load without exceeding the given deformation limit.

2.3 PROCESS MODELLING

The part and the tool in COMPRO are modelled using 4200 four-noded isoparametric quadrilateral elements under plane strain condition as shown in Figure 2.4. Because of the symmetry, only half of the geometry is modelled. As discussed in Chapter 1, an elastic shear layer is incorporated into the finite element mesh in order to simulate the tool-part interaction. The shear layer properties are adjusted to match the experimental warpage results of Twigg, (2001). In the experiment, two layers of FEP sheets were placed between the tool and the part to reduce the tool-part interaction. In this case, using a shear layer modulus of 5.52 kPa resulted in an accurate prediction of the deflection profile as shown in Figure 2.5.

2.4 STRUCTURAL MODELLING

The predicted deformation, stresses and material properties of the composite at the end of the process modelling are transferred as input to a 3D non-linear structural analysis software, ABAQUS (ABAQUS 5.8). The material properties transferred over to ABAQUS were fully cured properties of the laminate computed using the micromechanical models in COMPRO (Johnston et al., 2001). These properties for the nominal case are listed in Table 2.1. Being a 2D plane strain model, COMPRO can only provide information on a 2D plane strain section of the composite part. Therefore, to obtain the 3D spatial distribution of residual stresses and deformations necessary for the structural analyses, the output from COMPRO have to be mapped onto the 3D elements of ABAQUS. This is accomplished through a superposition method in which the deformations and stresses from COMPRO are assigned as initial conditions to

structural elements in ABAQUS. This method is explained in detail in the next section (Section 2.5).

The virtually manufactured structure is considered to be simply supported and subjected to progressively increasing compressive load P as shown in Figure 2.6. First the critical Euler buckling load, P_{cr}, of a perfect plate, free of imperfection and with nominal material properties, is calculated using the eigenvalue analysis option in ABAQUS and this value is found to be 29.5 N. Then this critical load is applied to the plate with initial imperfections. The non-linear relation between the axial load P and the out-of-plane displacement w is obtained by increasing the load P incrementally up to the limiting buckling load P_{cr} and computing the corresponding displacement. In general design practice, a structure is designed to its maximum capacity. A load larger than the capacity of the structure results in failure and a load lower than the capacity of the structure results in over-conservative design. In this case, the application of the critical buckling load leads to the buckling failure of the structure and a lower load leads to an over-conservative design. Hence, 75 percent of the critical buckling load, which gives a moderate deformation, is considered as the applied load and the deflection at this load level is considered for the subsequent reliability study.

2.5 PREDICTION OF THE 3D STATE OF STRESS

This section will discuss the procedure for predicting the three-dimensional state of stress in an element using the knowledge of stresses obtained from a plane strain type analysis such as COMPRO.

2.5.1 PLANE STRAIN

In plane strain problems, it is assumed that the out-of-plane strain is zero. The assumption is valid under the following conditions:

1. There is no loading in the out-of-plane direction and the in-plane loads are independent of the out-of-plane coordinate.

2. The out-of-plane dimension is very large compared to the in-plane dimensions.

Under thermal loading conditions, a plane strain element, by virtue of its constraints, will not allow any thermal expansion in the out-of-plane direction thus resulting in higher out-of-plane stresses and more deformation in the plane of the element.

2.5.2 THREE DIMENSIONAL PREDICTION

Since the complete state of stress (i.e. all six components of stress) is required in our case studies, an approach based on superposition principle is proposed here to predict the 3D states of deformation and stress using results obtained from 2D plane strain computations.

It is well known that the principle of superposition is only valid for linear elastic materials. Since the deformation of the part is constrained by the tool and most of the residual stresses develop during the cooling down part of the process cycle when the evolution of the elastic modulus of the resin has terminated, the application of the superposition method is justifiable. All the following calculations are carried out using ABAQUS.

(a) For applied mechanical load

First consider a cube of an isotropic material (the material properties used in ABAQUS are $E = 2$ GPa, $v = 0.25$, $\alpha = 25$ μm/m/°C, however the results are expressed here symbolically) under an applied mechanical load, P, in all three direction as shown in Figure 2.7(a). In a three dimensional problem, the cube is allowed to deform freely in all three directions. From Hooke's law and the equilibrium equation, the relation between the loads and the displacements can be written as

$$
\left\{ \begin{array}{c} \dfrac{P}{l^2} \\[2mm] \dfrac{P}{l^2} \\[2mm] \dfrac{P}{l^2} \end{array} \right\} = \frac{E(1-v)}{(1+v)(1-2v)} \begin{bmatrix} 1 & \dfrac{v}{(1-v)} & \dfrac{v}{(1-v)} \\[2mm] \dfrac{v}{(1-v)} & 1 & \dfrac{v}{(1-v)} \\[2mm] \dfrac{v}{(1-v)} & \dfrac{v}{(1-v)} & 1 \end{bmatrix} \left\{ \begin{array}{c} \dfrac{u}{l} \\[2mm] \dfrac{v}{l} \\[2mm] \dfrac{w}{l} \end{array} \right\}
\tag{2.1a}
$$

which results in

$$
u = v = w = \delta = \frac{P(1-2v)}{lE}
\tag{2.1b}
$$

It will be shown that the same results can be obtained by applying the loads separately in two steps and superposing the results.

Step 1

On the cube, only the loads in 1 and 2 directions are applied and the cube is allowed to deform freely in 1 and 2 directions but it is constrained in the 3rd direction (similar to plane strain condition) as shown in Figure 2.7(c). The displacements can then be obtained from the following equation (Equation 2.2a).

$$
\left\{ \begin{array}{c} \dfrac{P}{l^2} \\[2mm] \dfrac{P}{l^2} \\[2mm] \dfrac{P_3}{l^2} \end{array} \right\} = \dfrac{E(1-v)}{(1+v)(1-2v)} \begin{bmatrix} 1 & \dfrac{v}{(1-v)} & \dfrac{v}{(1-v)} \\[2mm] \dfrac{v}{(1-v)} & 1 & \dfrac{v}{(1-v)} \\[2mm] \dfrac{v}{(1-v)} & \dfrac{v}{(1-v)} & 1 \end{bmatrix} \left\{ \begin{array}{c} \dfrac{\delta_1}{l} \\[2mm] \dfrac{\delta_1}{l} \\[2mm] \dfrac{w}{l} = 0 \end{array} \right\}
\tag{2.2a}
$$

solving for δ_1 results in

$$
\delta_1 = (1+v)\frac{P(1-2v)}{lE} = (1+v)\delta
\tag{2.2b}
$$

It can be noted that the displacements are $(1+v)$ times higher than the actual three-dimensional displacements. The constraint in the 3rd direction results in an internal stress, $\sigma_3 = P_3 / l^2$, in that direction, such that

$$
P_3 = 2vP
\tag{2.2c}
$$

Step 2

In the 2nd step, the load in the 3rd direction, P, with the stress calculated in the previous step, considered as an initial stress, is applied to the cube as shown in Figure 2.7(d) and the cube is allowed to deform freely in all three directions. The load-displacements relation can then be written as

$$
\left\{ \begin{array}{c} \dfrac{P_1}{l^2} = 0 \\[2mm] \dfrac{P_2}{l^2} = 0 \\[2mm] \dfrac{(P-P_3)}{l^2} \end{array} \right\} = \dfrac{E(1-v)}{(1+v)(1-2v)} \begin{bmatrix} 1 & \dfrac{v}{(1-v)} & \dfrac{v}{(1-v)} \\[2mm] \dfrac{v}{(1-v)} & 1 & \dfrac{v}{(1-v)} \\[2mm] \dfrac{v}{(1-v)} & \dfrac{v}{(1-v)} & 1 \end{bmatrix} \left\{ \begin{array}{c} \dfrac{\delta_2}{l} \\[2mm] \dfrac{\delta_2}{l} \\[2mm] \dfrac{w}{l} \end{array} \right\}
\tag{2.3a}
$$

resulting in the following displacements

$$w = \frac{P(1-2v)}{lE} = \delta$$

$$\delta_2 = -v\frac{P(1-2v)}{lE} = -v\delta$$

(2.3b)

Now, the actual three-dimensional results (Equation 2.1b) can be obtained by combining (superposing) the results of both step 1 and step 2 (Figure 2.7(b)).

(b) For thermal load

The superposition principle for thermal loads is similar to mechanical loads, but instead of the applied load, the thermal expansions are superposed. First consider the same cube as in the previous case (Figure 2.8(a)) under thermal load (temperature increment $\Delta T = 100$ °C). If the cube is allowed to expand freely (Figure 2.8(b)), there will be no stresses in the cube and the deformation will be given by

$$\delta = l\alpha\,\Delta T$$

(2.4)

But in the plane strain case (Figure 2.8(c)), since the expansion in the out-of-plane direction (axis 3) is prevented, the out-of-plane stress will be nonzero and the in–plane deformations are (1+v) times greater than the actual deformations, i.e.

$$\sigma_1 = \sigma_2 = 0$$

$$\sigma_3 = -E\alpha\,\Delta T$$

(2.5a)

Therefore, the deformations are given by

$$\delta_1 = \delta_2 = (1+v)l\alpha\,\Delta T$$

$$\delta_3 = 0$$

(2.5b)

Now, if these stresses are introduced as initial stresses in a cube (Figure 2.9(a)) and the cube is allowed to expand freely, it will expand in the out-of-plane direction and contract in the in–plane direction such that (Figure 2.9(b)):

$$\delta_1 = \delta_2 = -v\,l\alpha\,\Delta T$$
$$\delta_3 = l\alpha\,\Delta T$$

$$(2.6)$$

The combination of Equations 2.5b and 2.6 (Figure 2.8(c) and Figure 2.9(b)) will give the actual deformation state. The above method can be extended to different numbers of elements by simply dividing the cube into several elements (Figure 2.9(c) and (d)).

The same is true for shell elements although there is no plane strain shell element available. This statement can be explained through an example. Consider a plate made of the same material as before, simply supported at all four corners and subjected to thermal loading. The dimensions of the plate and the number of shell elements used to model this plate are given in Figure 2.10. Due to the symmetry, only a quarter of the problem is considered for analysis.

First only a row of elements along the x direction is considered for the analysis as shown in Figure 2.11(a). To make it similar to a plane strain solid element, the displacement in the y direction and the rotations about the x and z axes are constrained to be zero. The stresses and deformations of these elements are found for a temperature increment of 10 °C. Then similar columns of elements with initial stresses are combined to form the full structure and allowed to equilibrate under the specified boundary conditions (Figure 2.11 (b)).

The results of the above method are compared with the full 3D analysis of the plate in Figures 2.12 – 2.13. An excellent agreement between the superposition method and the full 3D analysis can be observed.

The above method is a 2D shell to 3D shell mapping. But, if this problem is to be modeled in COMPRO, it should be modeled using plane strain elements as shown in Figure 2.14 (a). From this 2D plane strain analysis, the three dimensional results can be obtained in one of two ways:

1. Combine similar rows of 3D solid elements with initial stresses (obtained from plane strain analysis) in the y direction to form the full plate and allow it to equilibrate under these stresses (all 6 components) to obtain the 3D states of deformation and stress (i.e. 2D solid to 3D solid mapping).

2. Map the plane strain element results to a row of 3D composite shell elements. This mapping can be done by considering each row of the solid elements as a layer of the composite shell elements and averaging the stresses to the mid-point of the shell elements as shown in Figure 2.14 (b). (Each shell element covers 20 solid elements. The stresses in these 20 solid elements are averaged and transferred to the mid-point). Then similar rows of these shell elements with initial stresses are combined to form the full plate and allowed to equilibrate under these stresses.

Since the first method requires a huge amount of 3D brick elements, the second method is preferred here. The results from this modified method and the actual 3D results are compared in Figure 2.15 – 2.16. The differences in the results are due to the averaging of the stresses. Also when the stresses of the solid elements are mapped on to the shell elements, it is assumed that the normal stress in the z direction (out-of-plane stress) and the shear stresses in the x-z and y-z

planes are zero. This assumption is valid for thin parts and it is expected that the results would be less accurate as the part thickness increases.

2.6 PARAMETRIC STUDY

The parameters that influence the buckling characteristic of a composite structure can be grouped into three categories: parameters related to material properties and geometry of the structure, parameters related to processing of the structure (these parameters also influence the material properties and geometry of the composite structure), and the parameters related to loading and boundary condition. In the following reliability study, the parameters related to processing of the composite structure are considered as random variables and the other two categories of parameters are considered as deterministic. The following parametric study was performed to identify the most important process variables that have an effect on the warpage of the plate.

The process parameters considered in this study are maximum autoclave temperature (T), fibre volume fraction (V_f), ply misalignment (θ), autoclave pressure (p), heating rate (HR), hold time (HT) and cooling rate (CR) (here only a limited number of processing parameters are considered for demonstration purposes of the method even though there may be some other parameters which affect the warpage and load capacity of the part). The sensitivity factor, which is defined as the ratio of the percentage increase in warpage to percentage increase in the parameter, is calculated and plotted for each parameter as shown in Figure 2.17. From this figure, it is identified that the part warpage is most sensitive to temperature, fibre volume fraction and fibre misalignment. From now on it is assumed that the part warpage depends on only these three processing parameters.

2.7 RELIABILITY-BASED DETERMINATION OF PROCESS CONTROL PARAMETERS

In the following reliability study, the three processing parameters which are identified as the most influential on the warpage of the composite structure in the parametric study are considered as random variables and the rest of the processing parameters are considered as deterministic. Among the chosen three random variables, the distorted shape of the plate after processing, *w*, is a function of *T*, V_f, and *θ*, while the critical load, P_{cr} is only a function of *θ* and V_f, which influence the material properties. Since the variables *T*, V_f, and *θ* are subject to uncertainty due to possible lack of tight process control, the outcomes *w* and P_{cr} are also random.

For the purposes of this study the performance standards for the plate were defined as follows:

1. The deflection *w* should be within a range, from 20mm to 40mm, with specified reliability. These two limits are the design requirements for the serviceability and ultimate conditions. The lower limit (span/600) will ensure that buckling will not result in a sudden departure from the flat configuration (i.e. there would be some warning before collapse). The upper limit (span/300) will ensure that the plate will not be excessively deformed. These two conditions can be described by a set of two "performance functions", G_1 and G_2 as follows

$$G_1 = w(\theta, V_f, T) - 20$$
$$G_2 = 40 - w(\theta, V_f, T)$$

(2.5)

2. The applied load P should result in a sufficient reliability against buckling. This condition is expressed as a performance function G3,

$$G_3 = P_{cr}(\theta, V_f) - P \qquad\qquad (2.6)$$

Given that the variables are random, the failure or non-performance probabilities correspond to the events $G_1 < 0$, $G_2 < 0$ and $G_3 < 0$. Provided that the statistics of the variables are defined, these probabilities can be readily evaluated by forward reliability procedures. Although the formulation of the problem is simple, the evaluation of the G function for each combination of random variables is time consuming and generally makes standard simulation procedure quite inefficient. To make the simulation procedure efficient, the actual performance function, G, can be replaced by a response surface and the failure probabilities can be obtained by any forward reliability procedures using the software RELAN (Foschi et al., 1999a).

But it is difficult to find a simple response surface to represent G over the entire domain of interest. In this case, calculation is carried out by local interpolation of the deterministic database (Foschi and Li, 2000). The deterministic database is constructed for all possible ranges of the random variables as shown in Table 2.2. For each combination of the random variables, the stresses and deformations obtained from COMPRO are fed to ABAQUS to obtain the required results ($\Delta_{75\%}$, P_{cr}). The main advantage of this method is that the database can be expanded in future by either increasing the number of random variables or increasing the range of the random variables. The probability of failure in each case is obtained by importance sampling simulation around an anchor point, which is determined by using an approximate response surface and the First Order Reliability Method (FORM). The method is explained in detail in Chapter 1. In each case, the probability of failure can be expressed by the associated reliability index β.

Example 1

For the inverse problem, let us assume that the task is to find the design parameters $\overline{V}_f, \overline{T}$ and $\overline{P}$, mean values of the corresponding variables, assuming that the remaining relevant statistics are as shown in Table 2.3. That is, knowing the accuracy with which the angle θ and the variables V_f and T can be controlled, their mean values are to be found (except for $\overline{\theta} = 0.0°$). Along with these, the mean of the load P that can be applied is to be determined in such a way that the plate response has the following target reliabilities for each of the three performance criteria:

1. For G_1, a failure probability of 0.05, or a target reliability index $\beta_1 = 1.645$

2. For G_2, a failure probability of 0.05, or a target reliability index $\beta_2 = 1.645$

3. For G_3, a failure probability of 6.2×10^{-3}, or a target reliability index $\beta_3 = 2.500$

The first two conditions imply a 90% confidence in the interval 20mm $< w <$ 40mm. The inverse reliability computer program, IRELAN, searches for the optimum solution, calculating the reliability indices for different combinations of the design parameters and minimizing the differences between the calculated and target reliabilities, β_j and β_j^T ($j = 1,2,3$), respectively:

$$\Psi = \sum_{j=1}^{3} \left[\beta_j^T - \beta_j(\overline{V}_f, \overline{T}, \overline{P}) \right]^2 \tag{2.7}$$

In each case, the reliability indices were calculated by the forward procedure previously described, using the deterministic database for w and P_{cr}. Of course, the results are not an exact

achievement of the target reliabilities, but rather an optimized solution, and are shown in Table 2.4.

Example 2

In a second design example, we assume that the load P is given (with corresponding statistics), and that the mean of the variables V_f and T are the *design parameters* that have to be calculated to meet the same performance criteria. That is, process parameters have to be found to satisfy performance under given load demands in the structural application. Let us assume that P has an Extreme Type I distribution, with a mean of 15 N and a coefficient of variation 0.25. Statistics for θ are as shown in Table 2.3. The results of this second optimization are shown in Table 2.5. As shown, the lower load P, with the same coefficient of variation and target reliabilities, allows a slightly lower $\overline{V}_f$ and mean temperature $\overline{T}$.

2.8 OTHER SOURCES OF VARIABILITY

In the above analysis, the influence of variations in part thickness on the buckling is not considered. During processing of a composite part, the thickness of the part changes due to the following sources: inaccuracy in lay-up, drawing vacuum, cure shrinkage, resin flow and the change in resin modulus. From the above COMPRO can predict the thickness changes due to only the last three sources. The effect of the thickness change due to these three sources is explained below.

Cure shrinkage of the resin causes permanent thickness reduction of the lamina. Since the weight ratio of the fibre and the resin remains the same, cure shrinkage will not alter the material properties of the lamina. According to the expression for the Euler critical buckling load for a

simply supported column, x percentage of reduction in the thickness causes $100(1-(1-\frac{x}{100})^3)$

percentage reduction in the buckling load. For the composite material used in the above analysis,

cure shrinkage causes 3% reduction in thickness that in turn causes around 9% reduction in the

buckling load.

During processing the resin modulus changes from a very low to relatively very high value

(roughly 3 orders of magnitude increase in modulus). Due to the application of the autoclave

pressure, this change in the resin modulus induces permanent deformation in the lamina. If the

initial and final transverse moduli of the lamina are E_{ri} and E_{rf} respectively and the autoclave

pressure is p, by a simple strength of materials calculation, the permanent deformation of the

lamina per unit thickness is given by $P(\frac{1}{E_{ri}}-\frac{1}{E_{rf}})$. In this case, p is 586 kPa E_{ri} and E_{rf} values

are 183.8 MPa and 10.16 GPa respectively. This results in only 0.3% reduction in the thickness.

The third source of thickness reduction is the flow of resin. The excess resin in the lamina is

removed by using a bleeder on top/side of the part (Hubert, 1996). The resin flow reduces the

thickness of the part and in the meantime the fibre volume fraction of the lamina also increases.

By assuming that the longitudinal modulus of the part is $V_f E_{lf}$, an x percentage reduction in the

thickness due to resin flow causes $100(1-(1-\frac{x}{100})^2)$ percentage reduction in the buckling load.

For the flat part considered in the above analysis, top bleed of the resin causes around 7%

reduction in thickness that in turn causes 14% reduction in the buckling load capacity.

The reduction in thickness due to the three sources mentioned above is the average values. These

values can be easily calculated and accounted for in the design. But, the variability of the change

in thickness due to the above three sources with other processing parameters such as temperature, pressure, V_f, etc., should be investigated.

2.9 SUMMARY AND CONCLUSIONS

The methodology shown here is an effective means of linking manufacturing process control, structural analysis and evaluation of performance reliability for composite structures. Although a flat plate was used here as an application, the method is completely general and could be used with any structural form. The approach adopted here can potentially lead to a new design methodology that uses the *as-manufactured* rather than *as-designed* conditions as the basis for structural analysis leading to the reduction or elimination of uncertainties and costs associated with the use of empirical safety factors currently employed in design of composite structures.

2.10 TABLES

Table 2.1: Laminate material properties

Longitudinal elastic modulus, E_{11}	126 GPa
Transverse elastic modulus, $E_{22} = E_{33}$	10.9 GPa
Major Poisson's ratio in-plane, ν_{12}	0.264
Longitudinal shear modulus, $G_{12} = G_{13}$	5.04 GPa
Transverse shear modulus, G_{23}	3.28 GPa

Table 2.2: Database

θ	Ply misalignment (degree)
V_f	Fiber volume fraction
T	Temperature (F)
$\Delta_{75\%}$	Out of plane displacement at $P/P_{cr} = 75\%$ (mm)
P_{cr}	Critical buckling load (N)

θ	V_f	T	$\Delta_{75\%}$	P_{cri}
0	0.589	350	31.89	29.4772
0	0.589	385	36.33	29.4772
0	0.589	367.5	34.11	29.4772
0	0.589	332.5	29.76	29.4772
0	0.589	315	27.63	29.4772
0	0.648	350	23.05	32.2845
0	0.648	385	26.3	32.2845
0	0.648	367.5	24.67	32.2845
0	0.648	332.5	21.46	32.2845
0	0.648	315	19.9	32.2845
0	0.6185	350	26.81	30.8808
0	0.6185	385	30.57	30.8808
0	0.6185	367.5	28.69	30.8808
0	0.6185	332.5	24.98	30.8808
0	0.6185	315	23.18	30.8808
0	0.56	350	38.75	28.0735
0	0.56	385	44.12	28.0735
0	0.56	367.5	41.47	28.0735
0	0.56	332.5	36.19	28.0735
0	0.56	315	33.63	28.0735
0	0.53	350	50.3	26.6698

0	0.53	385	57.14	26.6698
0	0.53	367.5	53.79	26.6698
0	0.53	332.5	47.06	26.6698
0	0.53	315	43.82	26.6698
4	0.589	350	50.44	26.7868
4	0.589	385	56.56	26.7868
4	0.589	367.5	53.39	26.7868
4	0.589	332.5	47.25	26.7868
4	0.589	315	43.9	26.7868
4	0.648	350	33.65	29.5006
4	0.648	385	37.77	29.5006
4	0.648	367.5	35.62	29.5006
4	0.648	332.5	31.35	29.5006
4	0.648	315	28.96	29.5006
4	0.6185	350	40.49	28.1437
4	0.6185	385	45.4	28.1437
4	0.6185	367.5	42.84	28.1437
4	0.6185	332.5	37.82	28.1437
4	0.6185	315	35.04	28.1437
4	0.56	350	67.66	25.4767
4	0.56	385	75.86	25.4767
4	0.56	367.5	71.74	25.4767
4	0.56	332.5	63.55	25.4767
4	0.56	315	59.32	25.4767
4	0.53	350	99.31	24.1432
4	0.53	385	116.6	24.1432
4	0.53	367.5	105.3	24.1432
4	0.53	332.5	92.92	24.1432
4	0.53	315	87.33	24.1432
2	0.589	350	37.58	28.7519
2	0.589	385	42.07	28.7519
2	0.589	367.5	39.7	28.7519
2	0.589	332.5	35.12	28.7519
2	0.589	315	32.5	28.7519
2	0.648	350	27.07	31.5359
2	0.648	385	30.41	31.5359
2	0.648	367.5	28.64	31.5359
2	0.648	332.5	25.16	31.5359
2	0.648	315	23.17	31.5359
2	0.6185	350	31.53	30.1556
2	0.6185	385	35.34	30.1556
2	0.6185	367.5	33.32	30.1556
2	0.6185	332.5	29.37	30.1556
2	0.6185	315	27.11	30.1556
2	0.56	350	46.05	27.3717
2	0.56	385	51.56	27.3717
2	0.56	367.5	48.72	27.3717
2	0.56	332.5	43.12	27.3717
2	0.56	315	40.03	27.3717
2	0.53	350	60.53	25.9914
2	0.53	385	67.81	25.9914
2	0.53	367.5	64.13	25.9914
2	0.53	332.5	56.83	25.9914

2	0.53	315	51.71	25.9914
-2	0.589	350	37.58	28.7519
-2	0.589	385	42.07	28.7519
-2	0.589	367.5	39.7	28.7519
-2	0.589	332.5	35.12	28.7519
-2	0.589	315	32.5	28.7519
-2	0.648	350	27.07	31.5359
-2	0.648	385	30.41	31.5359
-2	0.648	367.5	28.64	31.5359
-2	0.648	332.5	25.16	31.5359
-2	0.648	315	23.17	31.5359
-2	0.6185	350	31.53	30.1556
-2	0.6185	385	35.34	30.1556
-2	0.6185	367.5	33.32	30.1556
-2	0.6185	332.5	29.37	30.1556
-2	0.6185	315	27.11	30.1556
-2	0.56	350	46.05	27.3717
-2	0.56	385	51.56	27.3717
-2	0.56	367.5	48.72	27.3717
-2	0.56	332.5	43.12	27.3717
-2	0.56	315	40.03	27.3717
-2	0.53	350	60.53	25.9914
-2	0.53	385	67.81	25.9914
-2	0.53	367.5	64.13	25.9914
-2	0.53	332.5	56.83	25.9914
-2	0.53	315	51.71	25.9914
-4	0.589	350	50.44	26.7868
-4	0.589	385	56.56	26.7868
-4	0.589	367.5	53.39	26.7868
-4	0.589	332.5	47.25	26.7868
-4	0.589	315	43.9	26.7868
-4	0.648	350	33.65	29.5006
-4	0.648	385	37.77	29.5006
-4	0.648	367.5	35.62	29.5006
-4	0.648	332.5	31.35	29.5006
-4	0.648	315	28.96	29.5006
-4	0.6185	350	40.49	28.1437
-4	0.6185	385	45.4	28.1437
-4	0.6185	367.5	42.84	28.1437
-4	0.6185	332.5	37.82	28.1437
-4	0.6185	315	35.04	28.1437
-4	0.56	350	67.66	25.4767
-4	0.56	385	75.86	25.4767
-4	0.56	367.5	71.74	25.4767
-4	0.56	332.5	63.55	25.4767
-4	0.56	315	59.32	25.4767
-4	0.53	350	99.31	24.1432
-4	0.53	385	116.6	24.1432
-4	0.53	367.5	105.3	24.1432
-4	0.53	332.5	92.92	24.1432
-4	0.53	315	87.33	24.1432

Table 2.3: Statistics of random variables

Variable	Mean	Coefficient of variation	Distribution
θ	0.00°	0.50° (Standard Deviation)	Normal
V_f	(To be found)	0.20	Lognormal
T	(To be found)	0.10	Lognormal
P	(To be found)	0.25	Extreme Type I

Table 2.4: Inverse reliability and optimum design parameters, EXAMPLE 1

Calculated Optimum Design Parameters	Performance Requirement	Target Reliability Index β^T	Achieved Reliability Index β
$\overline{V}_f$ =0.791	$G_1 = w - 20\text{mm}$	1.645	1.652
$\overline{T}$ = 356.89 °F	$G_2 = 40\text{mm} - w$	1.645	1.633
$\overline{P}$ = 16.39 N	$G_3 = P_{cr} - P$	2.500	2.497

Table 2.5: Inverse reliability and optimum design parameters, EXAMPLE 2

Calculated Optimum Design Parameters	Performance Requirement	Target Reliability Index β^T	Achieved Reliability Index β
$\overline{V}_f$ =0.786	$G_1 = w - 20\text{mm}$	1.645	1.632
$\overline{T}$ = 350.50 °F	$G_2 = 40\text{mm} - w$	1.645	1.646
	$G_3 = P_{cr} - P$	2.500	2.783

2.11 FIGURES
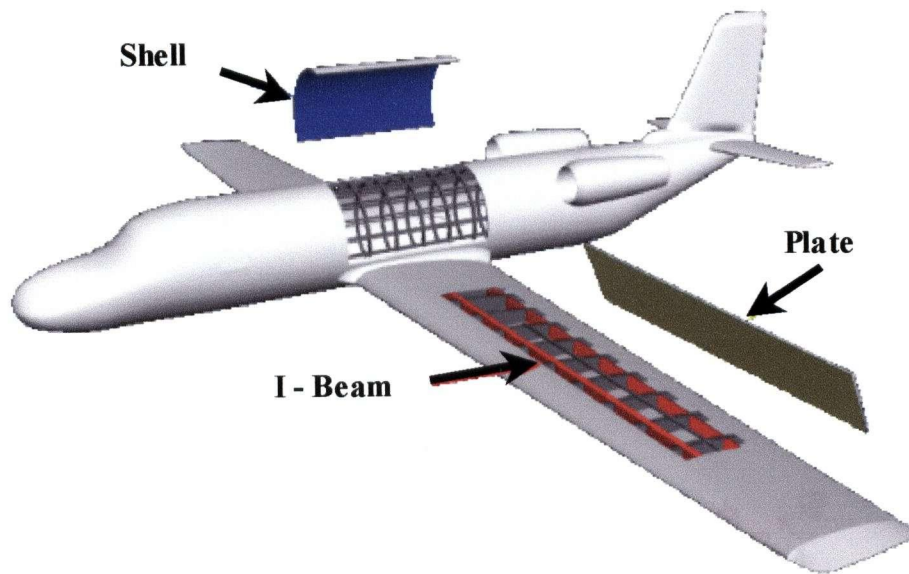
Figure 2.1: Basic structural elements (shell, plate and stiffener) of an aircraft.
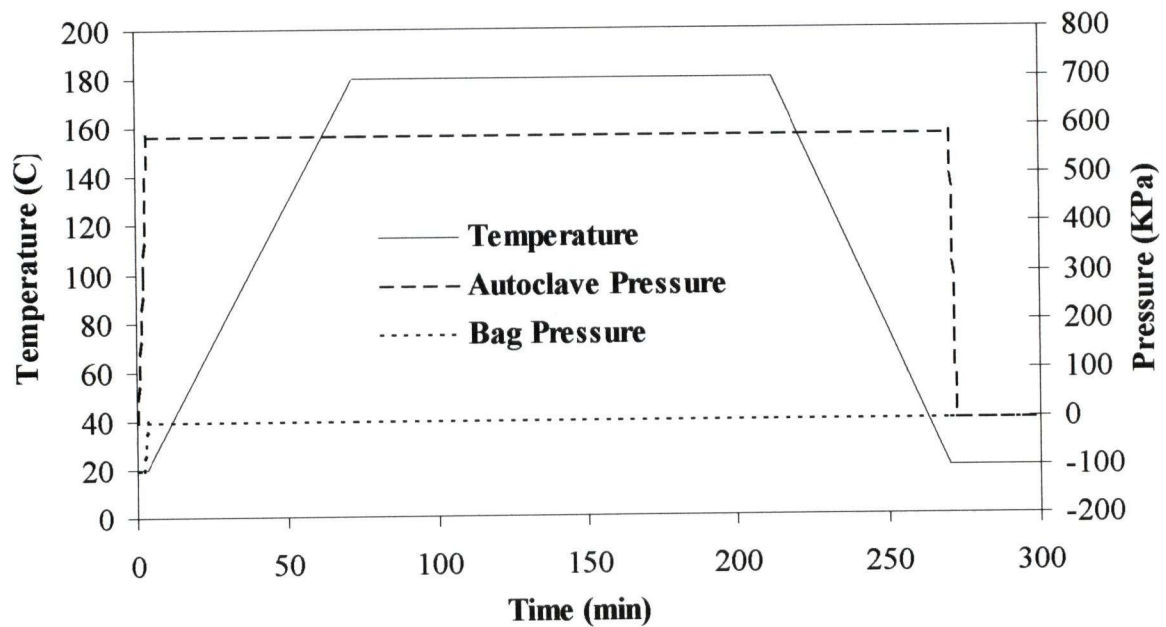
Figure 2.2: The air temperature and pressure cycle as applied in the autoclave during the processing of the composite plate (Twigg, 2001).
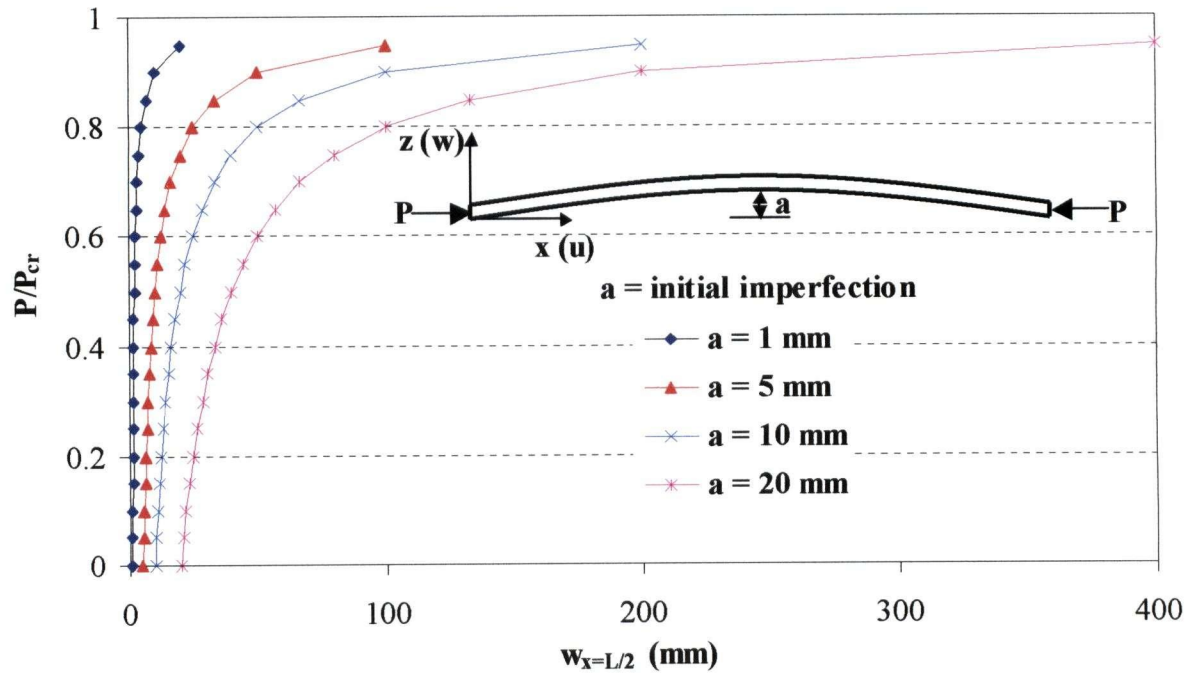
Figure 2.3: Non-dimensional axial load versus transverse deflection curve of the plate with various initial imperfections. P_{cr} is the critical Euler buckling load of the plate.
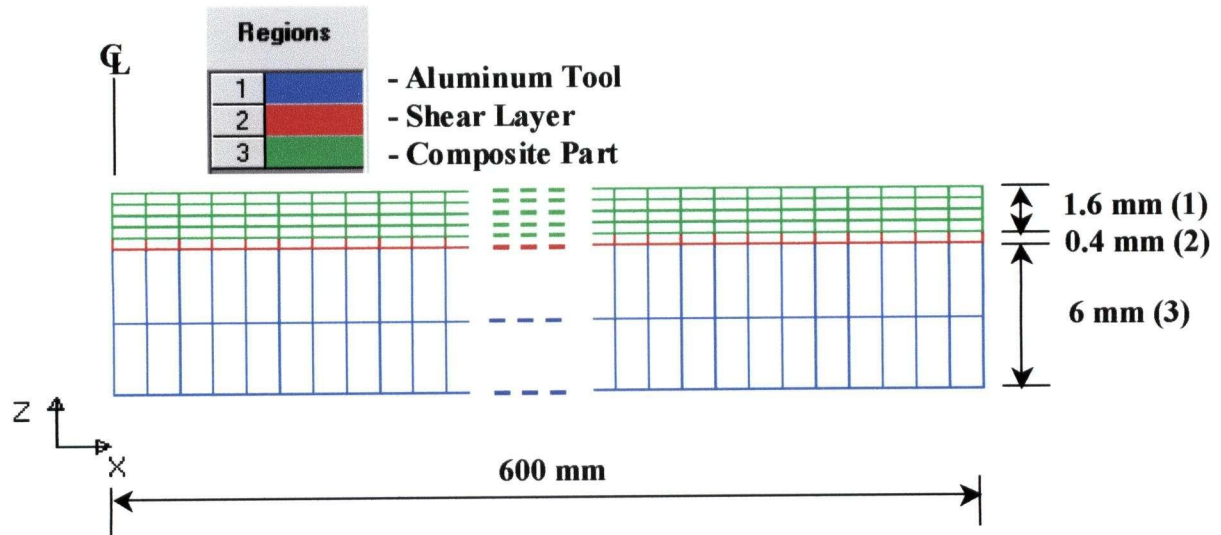
Figure 2.4: Finite element mesh of the plate and the tool used in COMPRO to virtually manufacture the part. Shear layer is used to model the tool – part interaction.
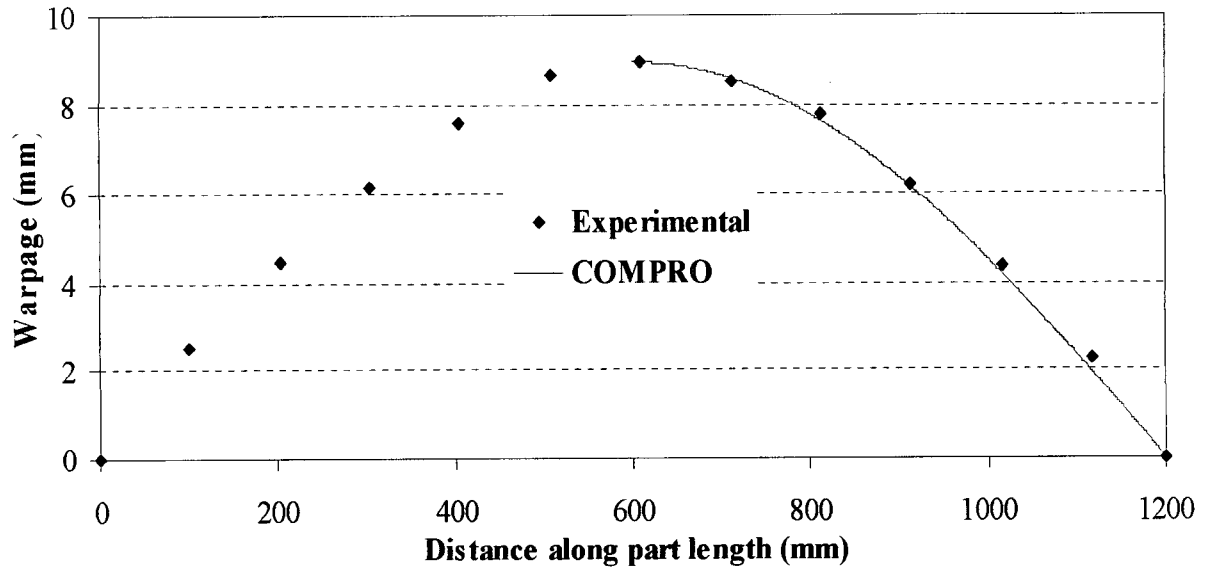
Figure 2.5: The warped profile of the 1200 mm long, 8 plies thick unidirectional composite part as it is removed from the aluminum tool. The prediction of COMPRO is compared with experimental results (Twigg, 2001).
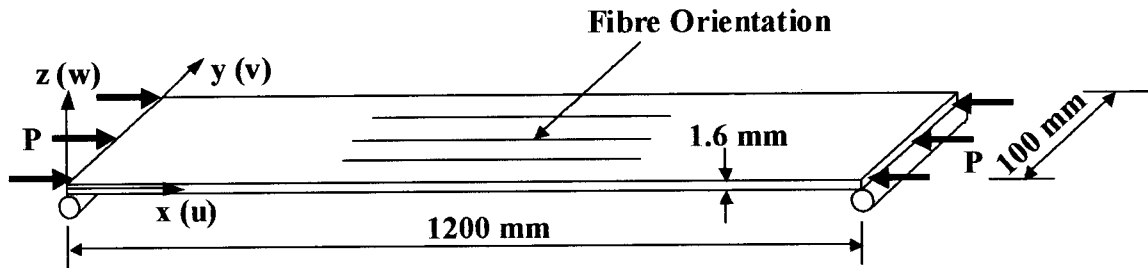
Figure 2.6: Schematic of the composite plate used for the case study. The applied loading and boundary conditions are also shown.

$$\delta = \frac{P(1-2v)}{lE}$$

$$\sigma_1 = \sigma_2 = \sigma_3 = \frac{P}{l^2}$$

$$\delta_1 = \frac{P(1+v)(1-2v)}{lE}$$

$$\sigma_1 = \sigma_2 = \frac{P}{l^2}$$

$$\sigma_3 = \frac{2vP}{l^2}$$

$$\delta_2 = \frac{-vP(1-2v)}{lE}$$

$$w = \frac{P(1-2v)}{lE}$$

$$\sigma_1 = \sigma_2 = 0$$

$$\sigma_3 = \frac{(1-2v)P}{l^2}$$
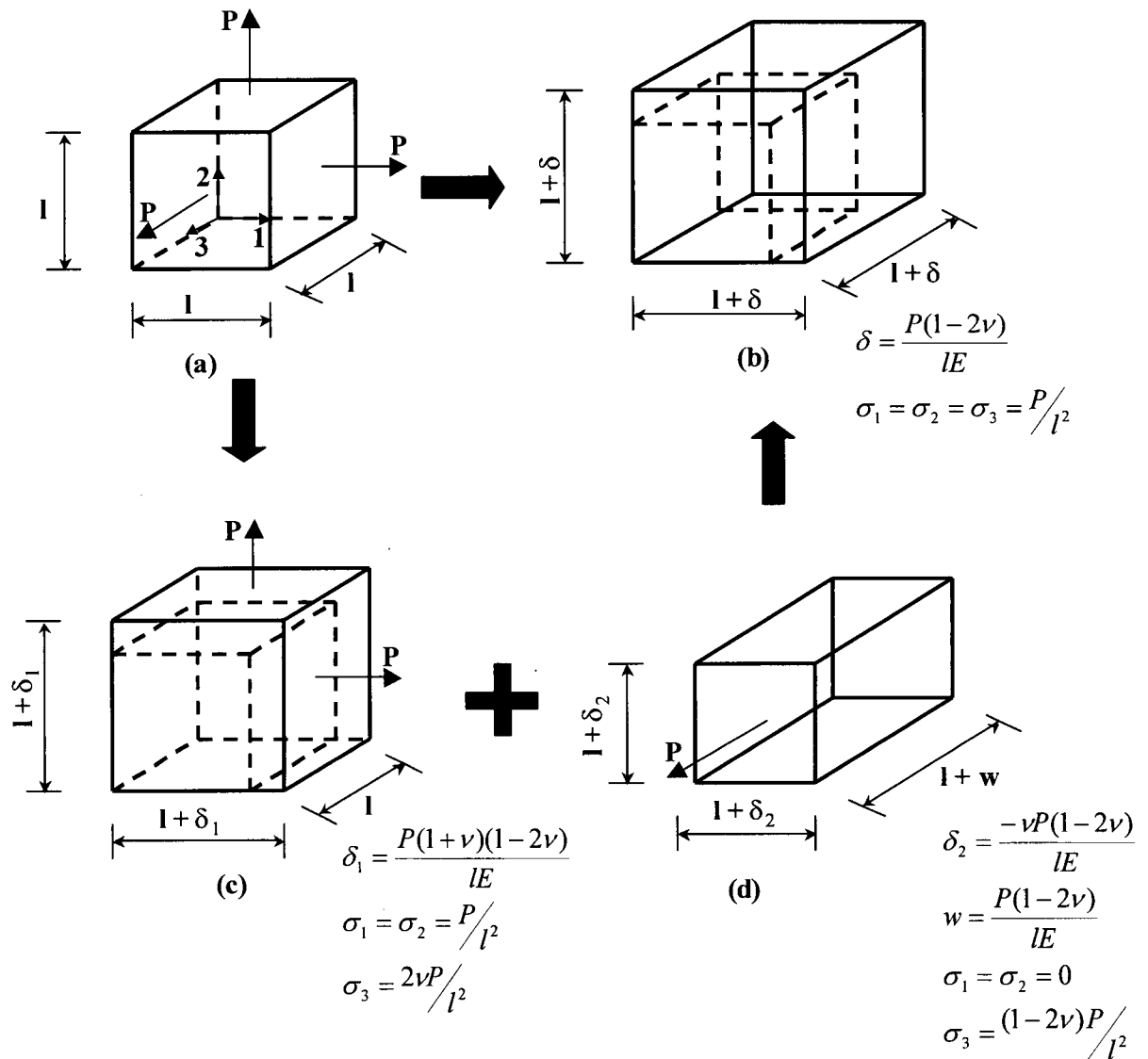
Figure 2.7: The superposition method to obtain the 3D state of stress from plane strain results for applied mechanical load (a) load P is applied in all three directions on a cube (b) 3D element: free to expand in all three directions (c) 2D plane strain element: load is applied in 1 and 2 directions, free to expand only in 1 and 2 direction, displacement in the 3rd direction is constrained to be zero (d) load is applied only in the 3rd direction, free to expand in all three directions. Combination of (c) and (d) gives (b).

$$\delta = l\,\alpha\,\Delta T$$
$$\sigma_1 = \sigma_2 = \sigma_3 = 0$$

(b)

$$\delta_1 = (1+\nu)\,l\,\alpha\,\Delta T$$
$$\sigma_1 = \sigma_2 = 0$$
$$\sigma_3 = -E\,\alpha\,\Delta T$$

(c)
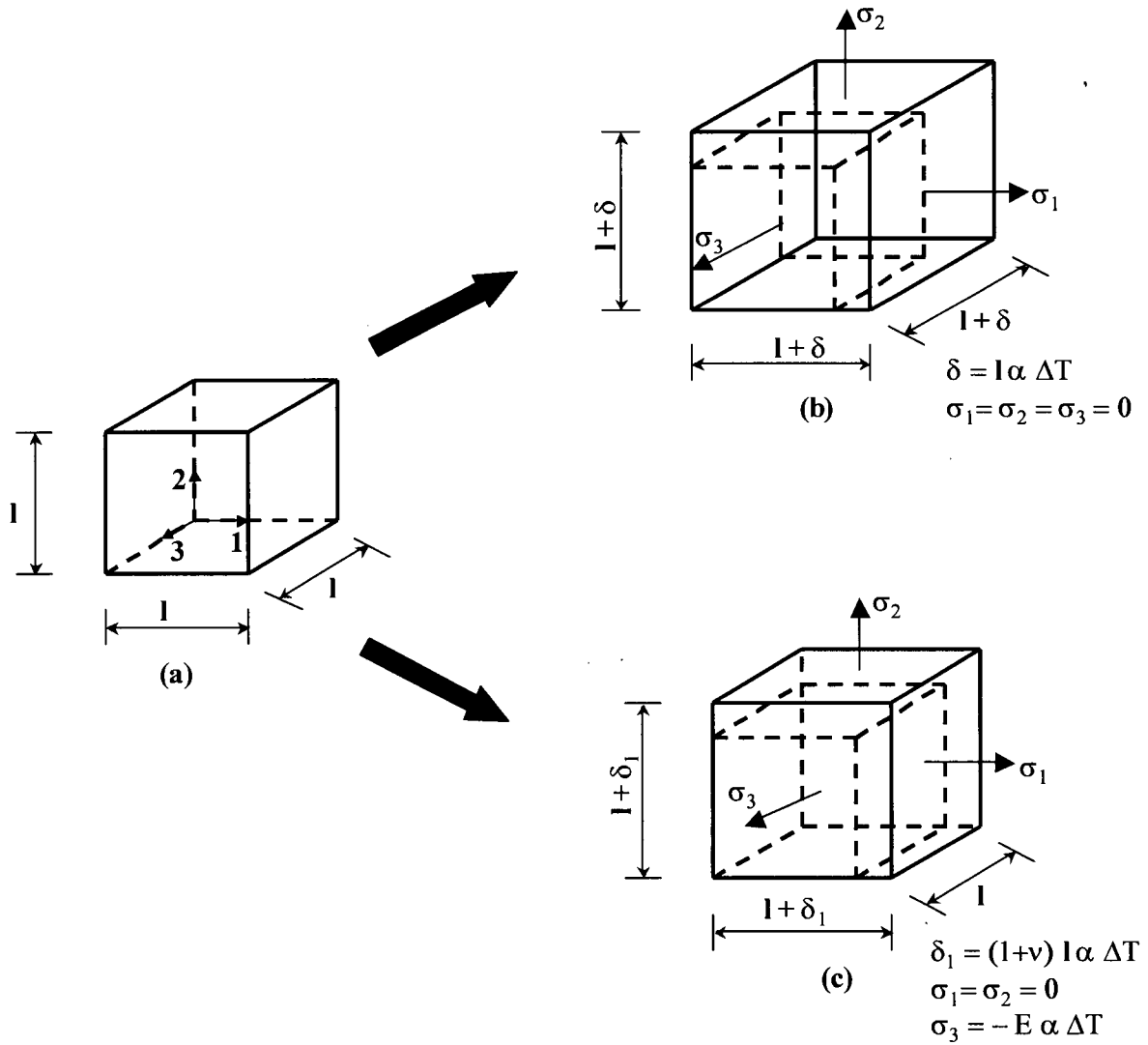
Figure 2.8: The difference between 3D element and plane strain element (a) temperature increment is applied to a cube (b) 3D element: free to expand in all three directions, no stresses developed (c) 2D plane strain element: free to expand only in 1 and 2 directions, displacement in the 3rd direction is constrained to be zero.

$\sigma_1 = \sigma_2 = 0$
$\sigma_3 = -E\,\alpha\,\Delta T$

(a)

$\sigma_1 = \sigma_2 = \sigma_3 = 0$
$\delta_2 = -\nu\,l\,\alpha\,\Delta T$
$\delta_3 = l\,\alpha\,\Delta T$

(b)

(c)

(d)
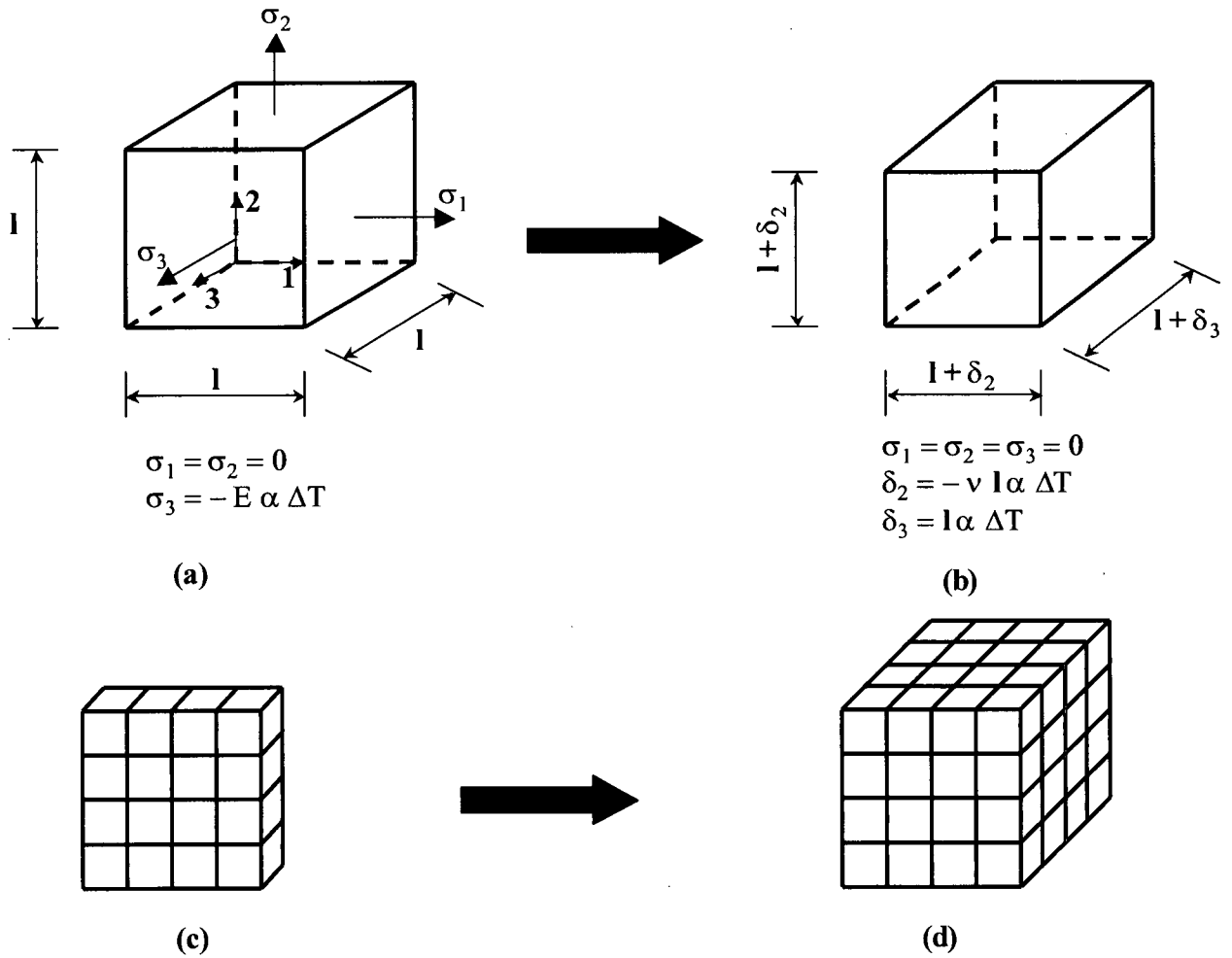
Figure 2.9: **Superposing the plane strain stresses to obtain the 3D results (a) stresses from the plane strain analysis are applied as initial stresses to the cube (b) the cube is allowed to equilibrate under these initial stresses with free boundary conditions (c) the cube problem is modeled with a number of plane strain elements (d) the plane strain block in (c) is combined to form the full cube and allowed to equilibrate under the stresses.**
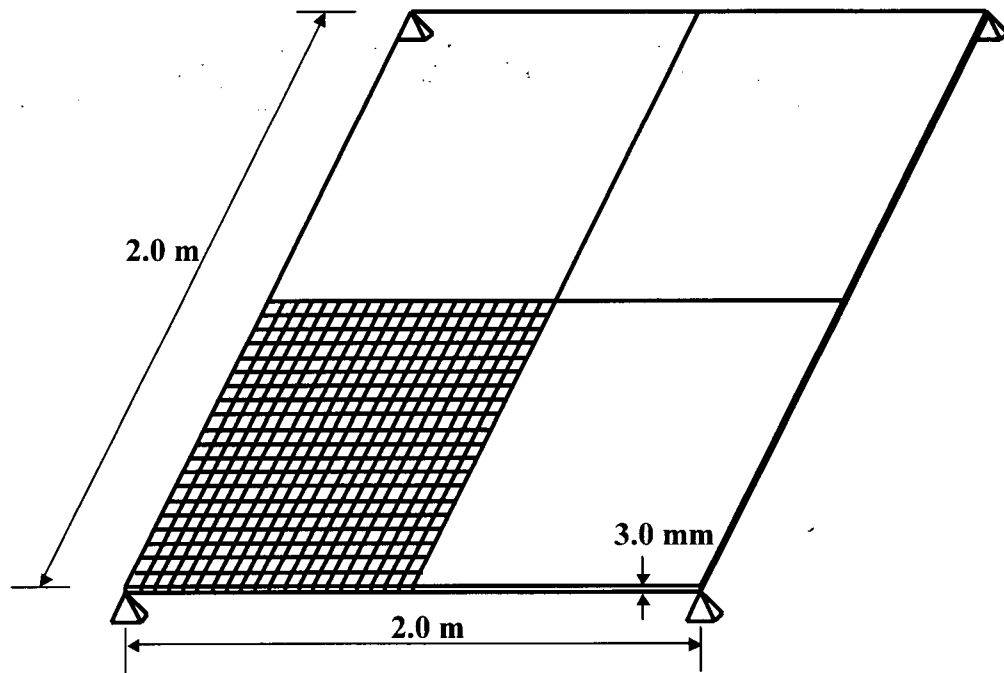
Figure 2.10: Plate simply supported at the corners under thermal load (finite element mesh is shown for one quarter of the plate).
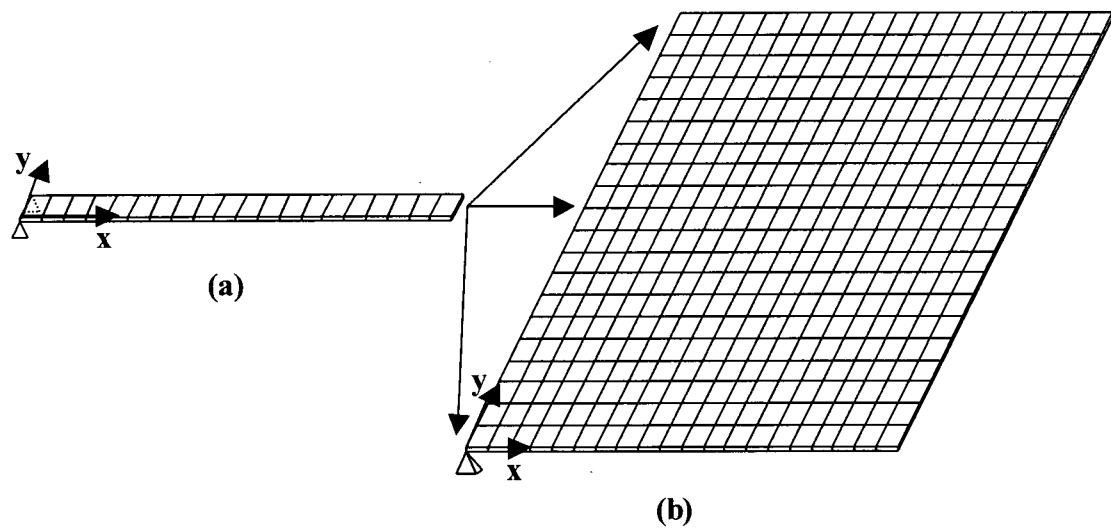
Figure 2.11: Developing the full 3D results using the results of a row of shell elements (a) a row of shell elements (b) full 3D plate.
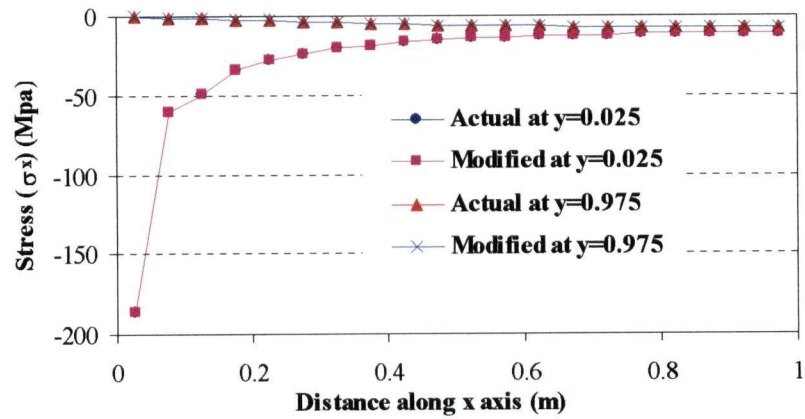
(a)
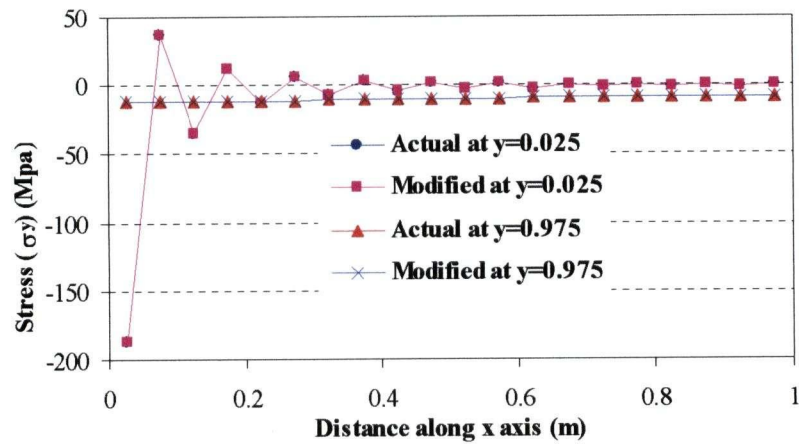
(b)
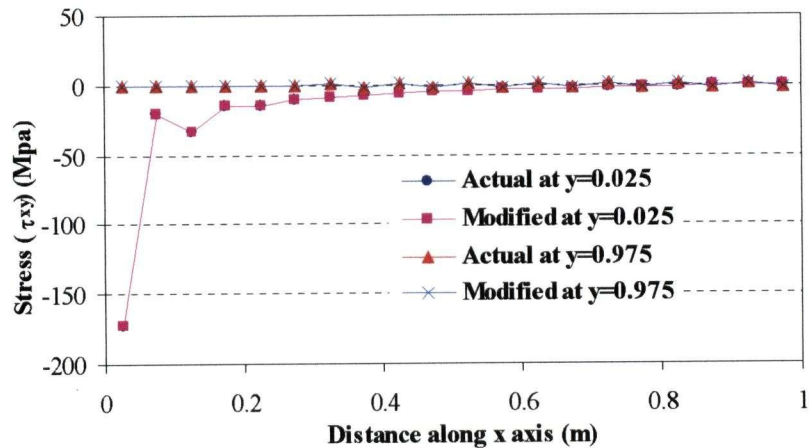
(c)

Figure 2.12: **Comparison of stresses from the actual 3D analysis and the modified superposition method (2D shell – 3D shell mapping) (a) stress σ_x (b) stress σ_y (c) stress τ_{xy}.**
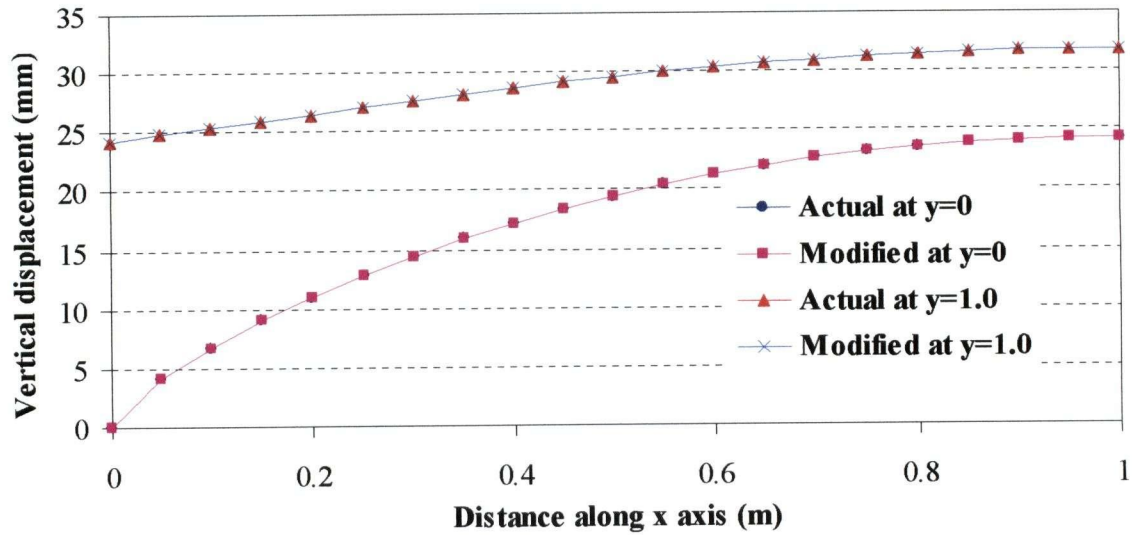
Figure 2.13: Comparison of vertical displacement from the actual 3D analysis and the modified superposition method (2D shell – 3D shell mapping).
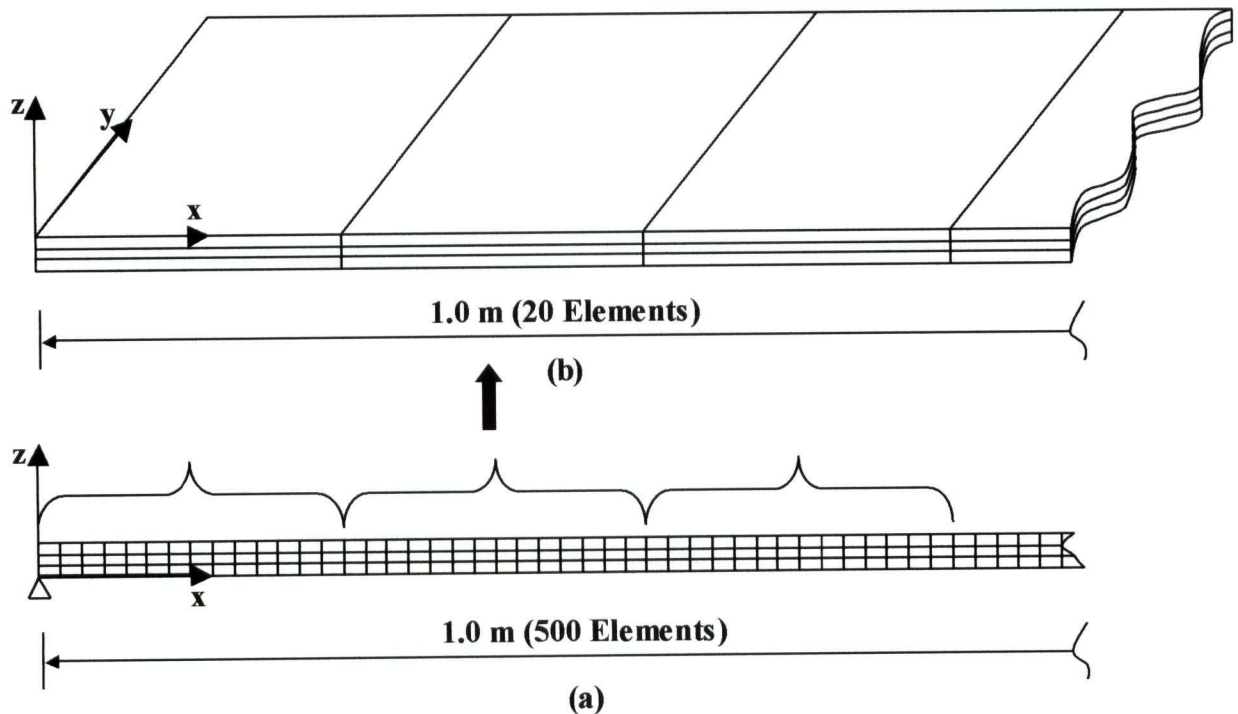
Figure 2.14: Mapping the stresses from plane strain solid element to shell elements. (a) The plate problem is modeled with plane strain solid elements and (b) the stresses from the plane strain analysis are mapped to the shell elements.
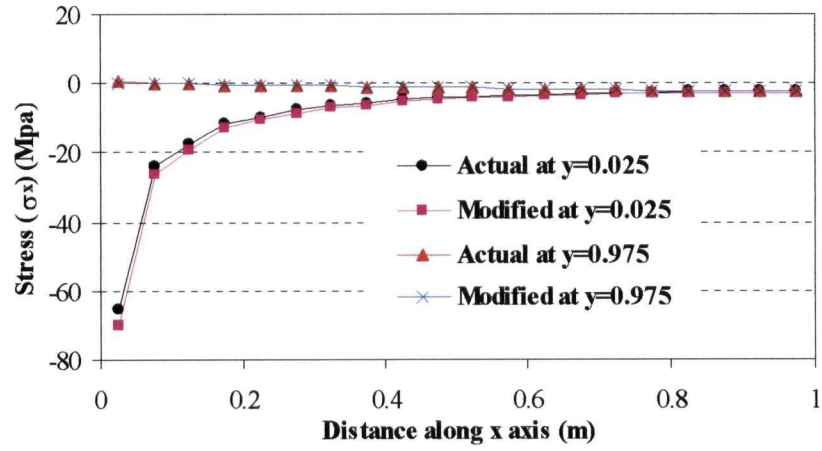
(a)
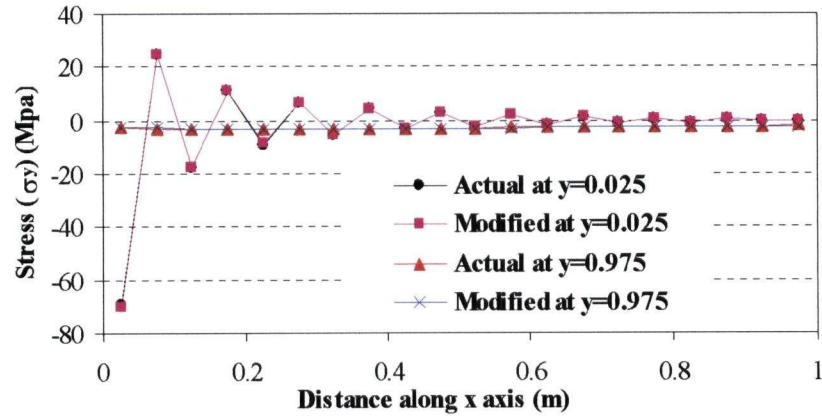
(b)
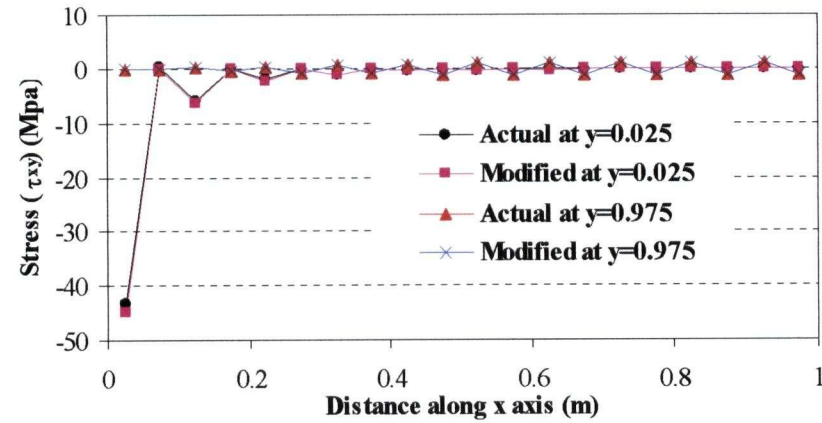
(c)

Figure 2.15: Comparison of stresses from the actual 3D analysis and the modified superposition method (2D solid – 2D shell – 3D shell mapping) (a) stress σ_x (b) stress σ_y (c) stress τ_{xy}.
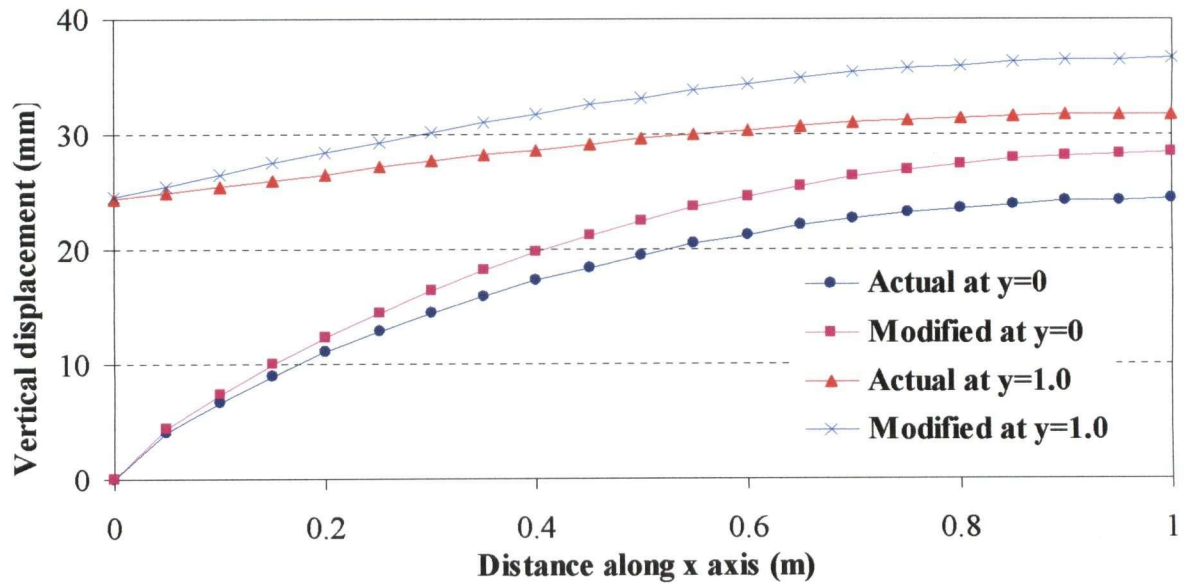
Figure 2.16: Comparison of vertical displacement from the actual 3D analysis and the modified superposition method (2D solid – 2D shell – 3D shell mapping).
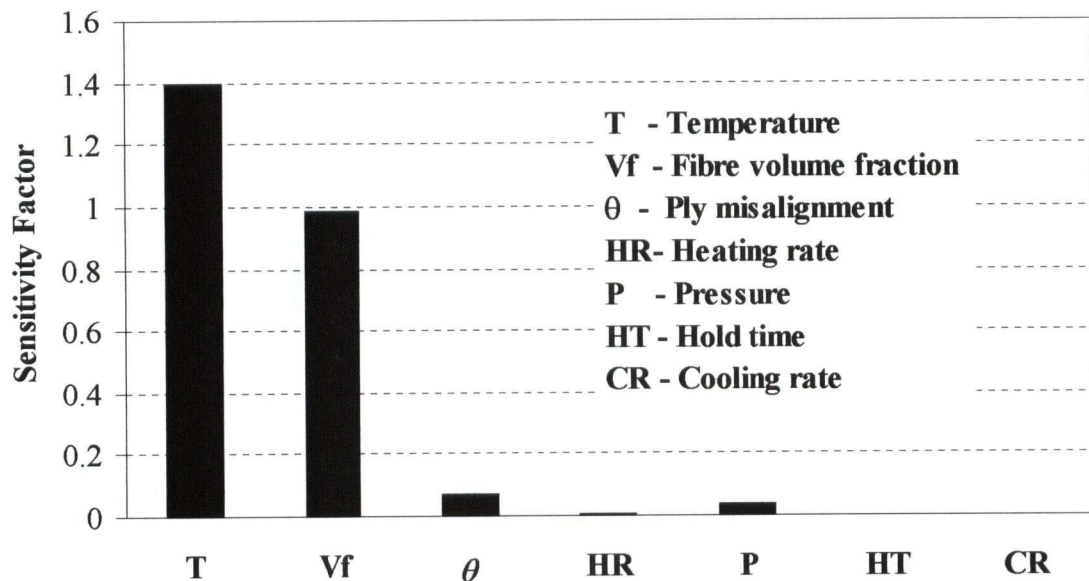
Figure 2.17: Sensitivity study of the processing parameters that mostly affect the warpage of the part. Sensitivity is defined as the ratio of the percentage increase in warpage to the percentage increase in the parameter.

CHAPTER 3: SPRING-IN OF ANGLED COMPOSITE LAMINATE

3.1 INTRODUCTION

In the previous chapter, it was demonstrated using a simple example, how the process induced deformations can affect the structural response of composite structures. In that study, only a limited number of processing parameters were considered for simplicity. In this chapter, we will consider a more complex shape laminate, an angle section, where an attempt will be made to identify and separate the various phenomena that give rise to process-induced residual stresses and deformations.

Stresses develop at two different levels during the processing of composite structures: micro-level and macro-level. Macro-mechanical stresses originate at the ply- and laminate-level. These stresses are the source for large-scale deformation of the processed part and may lead to premature failure of the structure during its service life. In most processing models, the macro-mechanical stresses are calculated by treating each lamina as a homogeneous but anisotropic layer. The effective material properties of each lamina are determined either using micro-mechanics equations or micro-mechanical finite element models based on the properties of the resin and fibre and their volume fraction at a given temperature and degree of cure of resin. A number of sources, such as tool-part interaction, anisotropic thermal strain, and cure shrinkage of resin, contribute to these stresses during the autoclave processing. The next chapter deals with the micro-level stresses in more detail.

The following are identified as the important sources that contribute to the process-induced deformations and stresses (Johnston, 1997):

1. Anisotropic thermal expansion
2. Chemical shrinkage of resin

 } Anisotropy

3. Tool-part interaction
4. Lay-up
5. Fibre volume fraction gradient through thickness

The spring-in of a curved composite part can be separated into two main components: corner component and warpage component. Among the sources stated above, anisotropy mainly contributes to the corner component while tool-part interaction contributes to the warpage component (Albert, 2001).

Many parameters are reported to affect the spring-in. These parameters can be separated into two groups: *intrinsic* and *extrinsic*. Intrinsic parameters are related to part geometry and material properties such as initial part angle, corner radius, thickness, lay-up, staking sequence and part shape and extrinsic parameters are related to tooling and processing such as cure cycle, tool surface condition, tool material, cure temperature, and pressure.

Over the past three decades, significant research has been conducted to either experimentally measure or model the effect of these parameters on spring-in. On the modelling front, a two-dimensional finite element computer code, COMPRO, was developed as mentioned earlier. Although the predictive capability of COMPRO has been investigated earlier, not every feature in the code has been validated against a carefully designed set of experiments. Recently Albert

(2001) carried out an extensive experimental program to study the effect of some of the above-mentioned parameters on dimensional stability of various shape composite laminates.

In this study, an attempt is made to capture numerically some of the process-induced dimensional changes measured by Albert (2001) using COMPRO.

3.2 REVIEW OF EXPERIMENTS

In this section, a brief review of the experimental work carried out by Albert will be given. This review includes only the experiments that are relevant to our studies. A more detailed description of the experiments and the results can be found in Albert (2001).

One of the tool geometries used in the experiments is shown in Figure 3.1. The tool surfaces were cleaned with acetone to remove any trace of oil or dirt and two or three coats of release agent (Multishield) were applied over the entire surface to prevent sticking of the part to the tool. In some cases, to reduce the friction between the tool and the part, an FEP (Fluorinated Ethylene Propylene) sheet was placed over the release agent before the part was laid up on the tool.

The parts were C- or L-shaped with flange length of 57 mm and thickness consisting of either 8 plies (1.6 mm) or 16 plies (3.2 mm). The web length of the C-shaped part was 102 mm. The parts made were either unidirectional laminates $[0]_n$, where all the fibres follow the curved contours, or quasi-isotropic laminates $[0/45/-45/90]_{ns}$ with 0° and 90° directions shown in Figure 3.2.

Once the lay-up was complete, the tool-part assemblies were placed inside an autoclave and cured under a prescribed temperature and pressure cycle (both one-hold and two-hold cure cycles were used). After the part was removed from the tool, approximately 1 cm was trimmed off the

edge to eliminate the edge thinning effect. The surfaces were polished and scanned. The scanned images were then digitally analyzed.

3.3 PROCESS MODELLING USING COMPRO

In this case study, the stresses and the deformations of an L-shaped composite component are numerically analysed and compared with experimental results of Albert (2001). The composite material used in the modelling is different from the material used in the actual experiments since the complete material data for the latter was not available. Hence, in this study, only the trends, rather than the absolute values, are compared with the experiments. The modelled composite component is made of unidirectional layers of AS4/8552 material. The thermal and mechanical properties of this material are given in Appendix A (Johnston, 1997). The plies are laid up on a tool and virtually processed using COMPRO. The part and the tool dimensions are shown in Figure 3.3. The part and the tool are modeled in COMPRO using 8-noded isoparametric elements (Osooly, 2001) as shown in Figure 3.4. The interaction between the part and the tool is modeled by adding a shear layer in between as indicated in Chapter 1. The mechanical and thermal boundary conditions are also shown in Figure 3.4.

The 16-ply unidirectional laminate of AS4/8552 material on aluminum tooling is chosen as the nominal case for this study, although other lay-ups and thicknesses are also examined. The part is cured under the cure cycles (both one and two holds) shown in Figure 3.5. After the simulation of tool removal, the spring-in angle is calculated. The spring-in angle is calculated using a technique analogous to that used in the experiment. The total spring-in is calculated by calculating the included angle of the lines connecting the two end points (one at the corner and one at the end) of the flanges as shown in Figure 3.6. The corner component of this total spring-

in is obtained by calculating the included angle between the tangent lines at the corner (see Figure 3.6) and the warpage component is given by the gradient of the warpage profile of the flange at the corner as shown in Figure 3.7.

3.4 SOURCES OF RESIDUAL STRESSES

3.4.1 ANISOTROPY

When an L-shaped composite part is cured in the autoclave without a tool, the part will spring in due to two main sources: anisotropy in the coefficient of thermal expansion (CTE) and cure shrinkage. The carbon fibre has a very low longitudinal CTE compared to its transverse CTE and the CTE of the matrix (Appendix A). This results in the laminate having a higher out-of-plane thermal strain than the in-plane thermal strain during curing. Similarly, the chemical shrinkage of the matrix is constrained by stiff fibres in the longitudinal direction, leading to higher chemical shrinkage strains in the out-of-plane direction than in the in-plane direction.

This difference between the in-plane and out-of-plane strains leads to the spring in/up of a curved composite part. This is purely driven by the circular geometry of the corner and mismatch of the in-plane and out-of-plane CTE and chemical shrinkage properties of the part. It is independent of the thickness and the mechanical properties of the part. A simple equation has been proposed for predicting the spring in/up of a curved laminate due to anisotropy (Nelson et al., 1989 and Radford et al, 1993):

$$\Delta\theta = \Delta\theta_{CTE} + \Delta\theta_{CS} = \theta\left(\frac{(CTE_L - CTE_T)\Delta T}{1 + CTE_T \Delta T}\right) + \theta\left(\frac{\phi_L - \phi_T}{1 + \phi_T}\right) \tag{3.1}$$

where θ = initial part angle (°)

$\Delta\theta$ = spring-in angle (°)

$\Delta\theta_{CTE}$ = component of spring-in due to thermal expansion anisotropy (°)

$\Delta\theta_{CS}$ = component of spring-in due to cure shrinkage anisotropy (°)

ΔT = change in temperature (°C)

ϕ_L = longitudinal chemical shrinkage strain (-)

ϕ_T = through-thickness chemical shrinkage strain (-)

CTE_l = longitudinal coefficient of thermal expansion (m/m/°C)

CTE_t = through-thickness coefficient of thermal expansion (m/m/°C)

The volumetric cure shrinkage of Hexcel 8552 epoxy resin is 0.099 (Johnston, 1997). Converting the volumetric shrinkage strain, V_r^S, to linear strain, ε_r^S, using the following equation

$$\varepsilon_r^S = \left(1 + V_r^S\right)^{1/3} - 1 \qquad (3.2)$$

leads to an isotropic strain of 3.2%.

The lamina longitudinal and transverse chemical shrinkage strains are calculated using the micromechanics equations (Equations B.11 and B.12 in Appendix B) proposed by Hashin and Rosen (1964) by setting the fibre strains equal to zero. The lamina longitudinal and transverse shrinkage strains are computed to be 5.217E-04 and 1.858E-02, respectively. During the curing process, according to Equation 3.1, the anisotropic coefficient of thermal expansion does not contribute to the spring-in and the cure shrinkage results in a spring-in of 1.6°.

In COMPRO, the 16-ply part without the tool is virtually processed and the predicted spring-in angle is 2.61°. The same spring-in is predicted for 8-ply and 24-ply parts as well. The higher value is due to the plane strain assumption in COMPRO. When the same run is repeated without

the Poisson's effect (i.e. when Poisson's ratios of the fibre and the matrix are set to zero), the prediction is 1.44°, which is very close to the analytical solution (Equation 3.1).

The error due to the plane strain assumption is also investigated using the commercial software ABAQUS for the 16-layer part by comparing the spring-in prediction by both plane strain analysis and three-dimensional analysis. In the analysis, only the spring-in due to CTE-anisotropy during the cooling down portion of the cure cycle is considered by assuming the material is fully cured and the temperature is uniform in the part. In the three-dimensional case, only one element of length 2 mm is modelled in the out-of-plane direction. From the results shown in Figure 3.8, the plane strain assumption over-predicts the spring-in for the unidirectional and [0/90] lay-ups and predicts accurately the spring-in for the quasi-isotropic lay-up. This trend can be explained by calculating the equivalent mechanical properties of the above lay-ups. Since the classical laminate plate theory does not account for the through thickness properties, a simple numerical model outlined below is used to predict the equivalent properties.

Numerical model to predict the equivalent properties of lay-ups

Consider a composite cube of 16 layers as shown in Figure 3.9(a). The cube is modelled in ABAQUS with a single 20-noded isoparametric solid composite element. The mechanical properties of a lamina are calculated from the fully cured properties of the resin and fibre using the micromechanics equations B.1 – B.12 in Appendix B. The stacking sequence of the lay-up starts from face-3a in the 3rd direction.

The boundary conditions applied are (Figure 3.9(b)):

Face-1a = Symmetric

Face-1b = Coupled

Face-2a = Symmetric

Face-2b = Coupled

Face-3a = Symmetric

Face-3b = Coupled

The symmetric boundary condition implies that the deformations of the nodes along that particular face in the direction normal to the face are constrained to be zero. The coupled boundary condition implies that all the nodes of that particular face are coupled to deform by the same amount in the direction normal to the face (this is achieved using the EQUATION function in ABAQUS).

To calculate the Young's modulus in the 1 direction (E_1), a constant displacement (0.1 units) is applied in the 1 direction to the face-1b and the resultant force in the same direction at the face-1a, the resultant deformations of the face-2b and face-3b are calculated. By dividing the resultant force by the applied displacement, we obtain E_1. i.e.

E_1 = *(Resultant force in direction 1)/(Applied displacement in direction 1)*

The Poisson's ratios are given by

v_{12} = *-(Resultant displacement of face-2b)/(Applied displacement in direction 1)*

v_{13} = *-(Resultant displacement of face-3b)/(Applied displacement in direction 1)*

The other mechanical properties are also calculated in a similar manner. The coefficients of thermal expansions are calculated by applying a known temperature (100 °C) and calculating the resultant deformations of faces 1b, 2b, and 3b in the direction normal to the respective faces.

CTE_1 = *(Displacement of face-1b)/(Applied temperature)*

The equivalent properties so calculated are listed in Table 3.1. The in-plane properties are seen to agree very well with those obtained from CLT (the values obtained from CLT are listed inside a square bracket next to the corresponding values from the above method in Table 3.1).

Difference between 3D and plane strain

In the 3D case, under a temperature change, the curved composite part can expand freely in the out-of plane direction (direction 2). But in the plane strain case, the out-of plane strain (ε_2) is fully constrained. This is equivalent to applying the negative of this out-of plane strain to a 3D part. Hence the plane strain condition induces the following additional in-plane strains due to the Poisson's effect.

$$\varepsilon_1 = v_{21}\varepsilon_2$$
$$\varepsilon_3 = v_{23}\varepsilon_2$$

(3.3)

If the material is isotropic then $v_{21} = v_{23}$ and the plane strain condition does not change the included angle of the part. However, for orthotropic materials $v_{21} \neq v_{23}$ and the plane strain condition changes the included angle according to Equation 3.1.

$$\Delta\theta = \frac{(v_{21} - v_{23})\varepsilon_2}{(1 + v_{23}\varepsilon_2)}$$

(3.4)

Hence, the magnitude of the difference in spring-in between 3D and plane strain depends on the difference between the two Poisson's ratios, namely, ($v_{21} - v_{23}$), and ε_2. For the unidirectional lay-up, both quantities are high and therefore the difference between the 3D and plane strain prediction of spring-in is high. For the [0/90]$_n$ lay-up, though ($v_{21} - v_{23}$) is high, ε_2 is small and therefore the difference is smaller. For the quasi-isotropic lay-up, both quantities are very small (see table 3.1) and so is the difference between 3D and plane strain predictions.

3.4.2 TOOL-PART INTERACTION

The presence of the tool affects the distortion of the part in two ways: thermally and mechanically. The thermal effect is due to the large thermal mass of the tool that induces a temperature gradient through the part thickness (Figure 3.10). During processing, the tool mechanically interacts with the curved part in two modes: constrains the part from springing in and introduces a shearing force at the tool-part interface due to the CTE mismatch between the part and the tool.

Experimental study of tool-part interaction

The tool-part interaction of a flat plate is discussed in detail by Twigg (2001). In his work, Twigg (2001) proposed an empirical equation (Equation 3.5) to predict the variation of part warpage with part thickness and length for the parts processed under similar processing conditions.

Maximum part warpage, $\qquad w_{max} \propto \dfrac{L^3}{t^2}$ $\qquad\qquad\qquad\qquad$ (3.5)

$$w_{max} = C\frac{L^3}{t^2}$$

where L is the half-length of part, t is the laminate thickness, and C is a proportionality constant.

By assuming first ply slip and constant shear stress along the part length, he proposed that this proportionality constant can be expressed as

$$C = \frac{2\tau_{net}}{E_{part}}$$ $\qquad\qquad\qquad\qquad$ (3.6)

where $\tau_{net} = (\tau_{interface} - \tau_{interply})$ as shown in Figure 3.11 and E_{part} is the elastic modulus of the part. From the average of his experimental results, he deduced a value of 6.2 kPa for τ_{net}. Based

on this value and the smaller lengths of the parts considered, the warpage component of the parts studied by Albert (2001) should be negligible (both Albert and Twigg used similar processing conditions and materials). However, Albert observed considerable warpage in her experiments. This may be attributed to the tool surface condition and the size of the part in both experiments. As reported by Twigg (2001), two conditions may prevail at the tool-part interface: sticking and sliding as shown in Figure 3.12. For a smaller part, the sticking condition may be dominant. This provides a rough explanation for the increased warpage in Albert's experiment. More experimental studies have to be done to verify this.

Modelling the tool-part interaction

As mentioned earlier, the tool-part interaction in the current version of COMPRO is simulated by introducing a shear layer. The introduction of an isotropic shear layer with very low Young's (and shear) modulus removes both the normal constraint and the tool-part interface shear effect. However, the introduction of an orthotropic shear layer with very low Young's (and shear) modulus only in the direction parallel to the tool-part interface removes the tool-part interface shear effect but maintains the constraining effect of the tool normal to the interface. The values of E_{11} and G_{13} of the shear layer are lowered by identical orders of magnitude. In the following discussion, the shear layer properties are quoted by the value of E_{11}. The order of E_{11} dictates the order of G_{13}. The usual practice is to select the shear layer properties to match the results of an experiment and then the same shear layer properties are used to predict the trend of the variation with other geometric parameters such as part thickness, part length etc. To satisfy Equation 3.5, the shear stress should be constant with these geometric parameters. To verify this, the shear stress in the shear layer between a flat part and an aluminum tool, similar to the model of Twigg (2001), is investigated at a certain time (200 min) during the cure cycle (Figure 3.13 – 3.14).

From these figures, it can be seen that the average interfacial shear stress remains constant with part thickness, which complies with Equation 3.5. But the average shear stress does not remain constant with part length. These graphs confirm the finding of shear lag theory that the gradient of the interfacial shear stress curve depends on the shear layer properties. Hence, by scaling the shear layer property by the ratio of the part length, the average shear stress can be maintained constant with part length as shown in Figure 3.15. In this figure, the shear layer properties of the 600 mm part are kept constant and the shear layer properties of the 300 mm and 1200 mm parts are modified by the length ratio. The variation of the maximum warpage of a flat plate with part thickness and part length is shown in Figure 3.16 – 3.17. In these figures, prediction of the COMPRO is compared with the analytical solution using Equation 3.5. In the analytical solution, the warpage of the 8-layer, 600 mm part is kept constant and the variation of the warpage with the part thickness and part length is calculated using Equation 3.5.

By introducing an isotropic shear layer with very low Young's and shear moduli, the mechanical interaction of the tool with the part is essentially eliminated while keeping the thermal mass effect of the tool, which introduces a temperature gradient through the thickness. The spring-in from this analysis was compared with the predicted spring-in value of the part without the tool. Only a small variation was observed due to the difference in the through thickness temperature gradient between the two cases. And the parts with three different thicknesses (1.6 mm, 3.2 mm and 4.8 mm) resulted in almost the same value of spring-in (~2.61°). This shows that the temperature gradient does not have a strong influence on the spring-in due to anisotropy, for this case study. It may have some influence on a thicker part.

During processing, when the part is constrained from springing in by the tool, stresses build up in the part that cause it to spring in once the tool is removed. The predicted spring-in of 8-ply, 16-

ply and 24-ply parts when the parts are constrained by the tool are given in Table 3.2 and Figure 3.18. According to this result, the contribution of the cure shrinkage to the total spring-in is small (~20%) compared to the contribution from CTE mismatch (~80%). However, when the part is not constrained, cure shrinkage anisotropy is the major source of springing in. This can be explained by observing the stress development through the cure cycle. Stress starts to develop significantly only after the vitrification point (mostly on the cooling down part). But much of the resin shrinkage occurs while the resin is in the rubbery state and therefore without any significant stress development.

The shearing effect of the tool is investigated by changing the shear layer properties from no bonding to full bonding (shear layer = tool). The labels used for different shear layers and their material properties are listed in Table 3.3. In the following discussion, the shear layer will be referred to by the labels. The spring-in of the part with different shear layer properties is shown in Figure 3.19. From the figure, it can be observed that only the changes in warpage component with shearing layer properties is significant while the change in corner component is very small.

To compare the modelling results with experiment, first an appropriate shear layer property should be selected to match one of the experimental results. Since in the experiment two types of surface conditions were used (Release agent (3 coats), Release agent (3 coats) + FEP), two different shear layers are selected to represent these two surface conditions. A comparison between the predicted and measured results for the spring-in of an 8-layer part under the 2-hold cure cycle, as shown in Figure 3.20, reveals that the selected shear layer properties, namely TS-1 for RA+FEP and TS-2 for RA only, are reasonable choices. The properties of the selected shear layers are listed in Table 3.4. In the following sections, when COMPRO results are compared to the experimental results, the same similarity will be maintained (i.e. RA+FEP = TS-1, RA = TS-

2). The results for both 8 layers and 16 layers, for the two tool surface conditions, are compared in Figure 3.21 and the parts details are listed in Table 3.5.

The question that comes to mind from this result is whether it is possible to conclude that anisotropy (CTE mismatch and cure shrinkage) contributes to the corner component of the spring-in while tool-part interaction (shear) contributes to the warpage component of the spring-in. If anisotropy is the sole contributor to the corner component, then the corner component should not vary with thickness, radius, tool surface condition etc. according to Equation 3.1. But according to Figure 3.21, the corner component does change with tool surface condition and part thickness. This trend can be explained by having a close look at the method of separating the warpage and the corner component. In our measurement method, the separation of warpage and corner components is done at the corner-flange interface. Hence, the warpage component only includes the warpage of the flange. It does not include the warpage of the corner as shown in Figure 3.22. Hence, depending on the curvature, the corner component may consist of the spring-in due to anisotropy and the spring-in due to warpage of the corner length. This warpage portion of the corner component may be the reason the corner component of the spring-in changes with part thickness, tool surface, etc.

3.5   EFFECT OF INTRINSIC AND EXTRINSIC PARAMETERS

In this section, the effect of the intrinsic and the extrinsic parameters are numerically predicted by modelling and compared with experiments. Since the material used in the modelling is different from the material used in the experiments and the material data are incomplete, no attempt is made to compare the absolute values. Instead only the trend of variation of the spring-in with the parameters is compared. In comparing the effect of a given parameter between two

parts, only that parameter is varied, while the rest of the parameters are kept identical. For example, if the purpose of the analysis is to compare the effect of part thickness, the trend of spring-in variation between two L-shaped parts predicted by the model may be compared with the trend of spring-in variation between two C-shaped parts from the experiment.

3.5.1 EFFECT OF PART THICKNESS

The predicted variation of corner and warpage components of the spring-in with part thickness is shown in Figure 3.23. According to Equation 3.1, spring-in due to anisotropy does not change with part thickness. But according to Equation 3.5, the spring-in due to tool-part interaction decreases with part thickness. However, both corner and warpage components are expected to decrease with increasing part thickness as shown in the Figure 3.23. A similar trend was also observed in the experiments as shown in Figure 3.24. In the experiments, while the tool is aluminum, the parts are C-shaped with both 8 and 16 unidirectional layers processed under a 2-hold cure cycle (Table 3.6).

3.5.2 EFFECT OF TOOL MATERIAL

In this section, the variations of spring-in with two different tool materials (aluminum and steel) are analysed. Similar to the part thickness, the tool material also does not change the spring-in due to anisotropy. Since the thermal properties of the tool materials are different, the temperature gradient through the part thickness may vary. But it has already been shown that the temperature gradient does not have significant affect the spring-in (Section 3.4.2). However, the warpage component may vary with the tool materials due to the difference in the CTE values. Since aluminum has a higher CTE value than steel, it causes a higher CTE mismatch between the tool

and the part. Therefore, it is expected that the warpage component for the case of aluminum tool are higher.

The comparison of COMRO predictions with the experimental results is shown in Figure 3.25 for 8 layers and Figure 3.26 for 16 layers. In the experiment C-shaped parts of unidirectional layers were processed under a 2-hold cure cycle (Table 3.7 – Table 3.8). In the modelling, selecting the shear layer properties for both tooling materials to match the respective tooling surface condition is not clear. For example SL-2 is selected to represent the RA tool surface for the aluminum tooling. But it is not verified whether the same shear layer can be used to represent the RA tool surface for the steel tooling. Hence, in this case, the mechanical properties of the shear layer are kept constant. But the thermal and mass properties are made to match the properties of the tooling material. In the Figures 3.25 and 3.26, both the experimental and modelling results show the same trend for the corner component. But the experiments show an opposite trend for the warpage component except for the 8-layer part with RA tool surface.

3.5.3 EFFECT OF LAY-UP

In this section, the effect of two different lay-ups (unidirectional and quasi-isotropic) on the spring-in are investigated and compared with experimental results.

As discussed in Section 3.4.1, the lay-up changes the spring-in due to anisotropy by altering the in-plane and the through thickness properties. According to Equation 3.1, the quasi-isotropic lay-up gives more spring-in due to anisotropy than the unidirectional lay-up (Figure 3.8). But it has already been shown that COMPRO may predict the opposite trend due to the plane strain assumption (Section 3.4.1).

Similar to anisotropy, it is reported in the literature, that the quasi-isotropic lay-up gives more spring-in due to tool-part interaction than the unidirectional lay-up (Albert, 2001). The reason behind this is given below (the mathematical derivation to support this argument is given in Appendix D). During the heat up portion of the cure cycle, the resin has very low modulus. Hence, the stress due to tool-part interaction mostly occurs at the first ply level and it reduces drastically with the distance away from the first ply. According to this, both unidirectional lay-up and the quasi-isotropic lay-up with 0-ply at the bottom have similar stress distribution during heat up. On the other hand, during the cool down portion of the cure cycle, the resin is fully cured and therefore has a higher modulus. Hence, the whole thickness of the part is involved in the interaction with the tool and the stress due to the tool-part interaction is almost constant through the thickness. The magnitude of this stress depends on the CTE and the axial stiffness of the part and it is different for both lay-ups. On the removal of the tool, the resultant of the stresses at these two stages (heat up and cool down) causes the part to warp. The curvature of the part is given by

$$\frac{d^2 w}{dx^2} = \frac{M}{EI} \propto \frac{M}{E} \tag{3.7}$$

Therefore, the warpage component of the spring-in should be in the following order

$$\theta_{[0/45/-45/90]2s} > \theta_{[0]4s} > \theta_{[90/45/-45/0]4s} \tag{3.8}$$

The prediction by COMPRO of the warpage of a 600 mm long and 16 plies thick flat part processed on a aluminum tool under the fully bonded tool surface condition shows a different trend,

$$w_{[0]4s} > w_{[0/45/-45/90]2s} > w_{[90/45/-45/0]4s} \tag{3.9}$$

-71-

The above argument is totally based on the first ply slip, which, in turn, is very sensitive to the initial resin modulus. Hence, warpage of the same flat part is analysed for different initial resin moduli as listed in Table 3.9. It shows that the expected trend is predicted correctly at low resin modulus. This leads to the same conclusion made by Twigg (2001) that the initial resin modulus should be obtained experimentally rather than selected arbitrarily as is done in currently (Johnston, 1997).

The effect of the lay-up on the spring-in is shown in Figure 3.27. From this figure, it can be observed that at low shear layer moduli, the corner component of the unidirectional lay-up is higher than the quasi-isotropic lay-up, but the warpage component is consistently lower. The comparison between the experimental results and the COMPRO prediction is shown in Figure 3.28. In the experiments, the parts are L-shaped and made of 8 layers. The flange length of the parts is 89 mm (greater than the model) and the included angle is 45° (less than the model). They are processed on an aluminum tool with RA surface condition under a 2-hold cure cycle (Table 3.10). Good agreement is observed between the experimental and modelling results when the trends in behaviour are compared.

3.5.4 Effect of Part Shape

In this section, the effect of part shape or geometry on the spring-in is examined. In particular, L and C shapes are compared. The C-shaped part geometry is shown in Figure 3.29. The web length is twice the flange length similar to the experiment. The variation of spring-in between the two shapes predicted by the model is shown in Figure 3.30. The corner components of both the L and C shapes are comparable. But the predicted warpage component of the C-shaped part is much larger than that of the L-shaped part with a higher proportion of the warpage occurring at

the web. In contrast to the above prediction, the experiment shows no difference between a C and an L shaped part. Note that Albert (2001) only reported the total warpage component. When the experimental warpage component is actually separated into the warpages of the flange and the web, it is observed that most of the warpage occurs in the web section as shown in Figure 3.31 (the flange warpages are nearly zero).

In a previous combined experimental and numerical work (Fernlund et al., 2001), the C-shaped part had a greater spring-in than the L-shaped part by about 20%. For the numerical study, a different version of COMPRO with updated geometry capability was used. The COMPRO version used in this current study does not have the updated geometry option and the prediction for the spring-in of the C-shaped part is much higher than the L-shaped part even if the tool part interaction is switched off by using a very low modulus shear layer. This indicates that the corner of the C-shaped part is prevented from sliding over the tool (corner locking) and, because of that, when the tool expands it stretches the web with it as shown in Figure 3.32. This suggests that, when a tool with an effectively zero CTE, such as Invar, is used, then both the L and C shapes should result in identical spring-in values. In fact, the analysis using COMPRO shows that the spring-in of the C shaped parts on an Invar tool is only 6% higher than the spring-in of the L-shaped part on the same tool.

Currently research work is underway to replace the shear layer in COMPRO with a more realistic and robust contact interface model with updated geometry capability. In the meantime, a crude method is introduced in this section to overcome the corner-locking problem. In this method, the shear layer is divided into three regions (web, corner and flange) as shown in Figure 3.33. The web and the flange shear layers have the usual shear layer properties (example E_{11} = 6.95E5 Pa). To eliminate the corner-locking, a gap is introduced in the corner (only for the C-

shaped part) by using an isotropic shear layer with very low Young's (and shear) modulus. The results of this modified method is compared with the earlier results for the C-shaped part in Figure 3.34. It can be seen that with this modification both the C-shaped and L-shaped parts show almost the same amount of spring-in. The result is also compared with the experimental result in Figure 3.35 and Figure 3.36. In the experiment, the parts are 8 layers thick and they are processed on both aluminum and steel tool with RA(3) surface condition under a 2-hold cure cycle (Table 3.11 – Table 3.12). A good agreement between the experimental results and the predicted results is observed. Hence, this crude method may serve as a temporary solution to overcome the corner-locking problem in COMPRO until a more scientifically sound method such as the contact surface method is developed.

3.6 SUMMARY AND CONCLUSIONS

The accuracy of the reliability design method introduced in Chapter 1 mostly depends on the prediction capability of COMPRO. The key issue in the modelling is to model the tool-part interaction correctly. Extensive research in both experimental and numerical areas has been conducted to model the tool-part interaction with reasonable accuracy in COMPRO.

Currently, the tool-part interaction is modeled in COMPRO by introducing a thin shear layer. In this work, the capability of COMPRO to predict the variation of spring-in of an angled part with intrinsic and extrinsic parameters is verified. For this purpose, COMPRO results are compared with the experimental results of Albert (2001). Unfortunately, due to the unavailability of the material data for the composite material used in the experiment, only the trend of variation was examined using the data of a similar material. Although the shear layer method is not a physically accurate representation of the tool-part interaction, it can be used to capture some

important phenomena during processing. The method proposed here to overcome the corner-locking in a C-shaped part by introducing a gap in the corner should be verified with more experimental data.

3.7 TABLES

Table 3.1: Evaluated laminate equivalent properties (the values in [ ] are those obtained using CLT).

Property	$[0]_{16}$	$[0/90]_{4s}$	$[0/45/-45/90]_{2s}$
E_1 (GPa)	122.800 [122.8]	66.664 [66.64]	48.492 [48.47]
E_2 (Gpa)	9.920 [9.920]	66.664 [66.64]	48.492 [48.47]
E_3 (GPa)	9.920	12.092	12.092
v_{12}	0.2680 [0.2680]	0.0397 [0.0401]	0.3015 [0.3018]
v_{13}	0.2680	0.4207	0.3060
v_{23}	0.4710	0.4207	0.3060
v_{21}	0.0216	0.0397	0.3015
v_{31}	0.0216	0.0763	0.0763
v_{32}	0.4710	0.0763	0.0763
CTE_1 (μm/mm/C)	0.600 [0.600]	3.1515 [3.151]	3.1515 [3.151]
CTE_2 (μm/mm/C)	28.600 [28.600]	3.1515 [3.151]	3.1515 [3.151]
CTE_3 (μm/mm/C)	28.600	39.793	39.793

Table 3.2: Spring-in of the L-shaped composite parts when constrained by the tool.

Part Lay-up	Total Spring-in (deg)	CTE Mismatch (%)	Cure Shrinkage (%)
8	0.750	72.17	27.83
16	0.659	86.34	13.66
24	0.634	90.88	9.12

Table 3.3: Shear layer properties and their identification labels.

Shear Layer Labels	Longitudinal Modulus E_{11} (Pa)	Shear Modulus G_{13} (Pa)	$E_{11, \text{shear Layer}}/E_{11, \text{tool}}$
SL-0	$6.9*10^{-3}$	$2.6*10^{-3}$	10^{-13}
SL-1	$6.9*10^{5}$	$2.6*10^{5}$	10^{-5}
SL-2	$6.9*10^{6}$	$2.6*10^{6}$	10^{-4}
SL-3	$6.9*10^{7}$	$2.6*10^{7}$	10^{-3}
SL-4	$6.9*10^{8}$	$2.6*10^{8}$	10^{-2}
SL-5	$6.9*10^{10}$	$2.6*10^{10}$	1

Table 3.4: Selected shear layer properties to represent the experimental tool surface conditions.

Tool Surface	COMPRO		Experiment	
	Shear Layer Properties	Warpage Component of Spring-in (deg)	Tool Surface Condition	Warpage Component of Spring-in (deg)
TS-1	$E_{11} = 6.9E4$ Pa $G_{13} = 2.6E4$ Pa	0.135	Release Agent (3 coats) + FEP	0.14
TS-2	$E_{11} = 7.6E6$ Pa $G_{13} = 2.9E6$ Pa	0.895	Release Agent (3 coats)	0.92

Table 3.5: Spring-in variation with tool surface conditions. COMPRO predictions are compared with experimental results.

Part Shape	Lay-up	Tool Material	Tool Surface	Cure Cycle	Spring-in	
					Corner	Warpage
COMPRO						
L	$[0]_8$	Aluminum	TS-1	2	0.79	0.14
L	$[0]_8$	Aluminum	TS-2	2	0.95	0.90
L	$[0]_{16}$	Aluminum	TS-1	2	0.73	0.08
L	$[0]_{16}$	Aluminum	TS-2	2	0.75	0.33
Experiment						
C	$[0]_8$	Aluminum	RA(3)+FEP	2	0.78	0.14
C	$[0]_8$	Aluminum	RA(3)	2	0.97	0.92
C	$[0]_{16}$	Aluminum	RA(3)+FEP	2	0.72	0.07
C	$[0]_{16}$	Aluminum	RA(3)	2	0.83	0.28

Table 3.6: Spring-in variation with part thickness. COMPRO predictions are compared with experimental results.

Part Shape	Lay-up	Tool Material	Tool Surface	Cure Cycle	Spring-in	
					Corner	Warpage
COMPRO						
L	$[0]_8$	Aluminum	TS-1	2	0.79	0.14
L	$[0]_{16}$	Aluminum	TS-1	2	0.73	0.08
L	$[0]_8$	Aluminum	TS-2	2	0.95	0.90
L	$[0]_{16}$	Aluminum	TS-2	2	0.75	0.33
Experiment						
C	$[0]_8$	Aluminum	RA(3)+FEP	2	0.78	0.14
C	$[0]_{16}$	Aluminum	RA(3)+FEP	2	0.72	0.07
C	$[0]_8$	Aluminum	RA(3)	2	0.97	0.92
C	$[0]_{16}$	Aluminum	RA(3)	2	0.83	0.28

Table 3.7: Spring-in variation with tool material for an 8-layer unidirectional part. COMPRO predictions are compared with experimental results.

Part Shape	Lay-up	Tool Material	Tool Surface	Cure Cycle	Spring-in	
					Corner	Warpage
COMPRO						
L	$[0]_8$	Aluminum	TS-1	2	0.79	0.14
L	$[0]_8$	Steel	TS-1	2	0.79	0.13
L	$[0]_8$	Aluminum	TS-2	2	0.95	0.90
L	$[0]_8$	Steel	TS-2	2	0.87	0.50
Experiment						
C	$[0]_8$	Aluminum	RA(3)+FEP	2	0.78	0.14
C	$[0]_8$	Steel	RA(3)+FEP	2	0.65	0.19
C	$[0]_8$	Aluminum	RA(3)	2	0.97	0.92
C	$[0]_8$	Steel	RA(3)	2	0.81	0.55

Table 3.8: Spring-in variation with tool material for a 16-layer unidirectional part. COMPRO predictions are compared with experimental results.

Part Shape	Lay-up	Tool Material	Tool Surface	Cure Cycle	Spring-in	
					Corner	Warpage
COMPRO						
L	$[0]_{16}$	Aluminum	TS-1	2	0.73	0.08
L	$[0]_{16}$	Steel	TS-1	2	0.73	0.07
L	$[0]_{16}$	Aluminum	TS-2	2	0.75	0.33
L	$[0]_{16}$	Steel	TS-2	2	0.75	0.20
Experiment						
C	$[0]_{16}$	Aluminum	RA(3)+FEP	2	0.72	0.07
C	$[0]_{16}$	Steel	RA(3)+FEP	2	0.60	0.18
C	$[0]_{16}$	Aluminum	RA(3)	2	0.83	0.28
C	$[0]_{16}$	Steel	RA(3)	2	0.77	0.38

Table 3.9: Variation of maximum warpage of a flat part (600mm long, 16 plies thick) with lay-up.

Initial Resin Modulus (Pa)	Maximum Warpage (mm)		
	$[0]_{16}$	$[0,45,-45,90]_{2S}$	$[90,45,-45,0]_{2S}$
4.67E6	38.3	37.2	15.8
4.67E5	28.8	45.4	22.1
4.67E4	17.9	27.5	9.8

Table 3.10: Spring-in variation with part lay-up. COMPRO predictions are compared with experimental results.

Part Shape	Lay-up	Tool Material	Tool Surface	Cure Cycle	Spring-in	
					Corner	Warpage
COMPRO						
L	$[0]_{16}$	Aluminum	TS-2	2	0.95	0.90
L	$[0,45,-45,90]_{S}$	Aluminum	TS-2	2	1.01	1.23
L	$[0]_{16}$	Steel	TS-1	2	0.73	0.08
L	$[0,45,-45,90]_{2S}$	Steel	TS-1	2	0.69	0.10
Experiment						
L	$[0]_{8}$	Aluminum	RA(3)	2	0.81	0.71
L	$[0,45,-45,90]_{S}$	Aluminum	RA(3)	2	0.76	1.22
C	$[0]_{16}$	Steel	RA(3)+FEP	2	081	0.04
C	$[0,45,-45,90]_{2S}$	Steel	RA(2)+FEP	2	0.95	0.15

Table 3.11: Spring-in variation with part shape for aluminum tool. COMPRO predictions are compared with experimental results.

Part Shape	Lay-up	Tool Material	Tool Surface	Cure Cycle	Spring-in		
					Corner	Warpage	
						Web	Flange
COMPRO							
L	$[0]_8$	Aluminum	TS-2	2	0.95	0.45	0.45
C	$[0]_8$	Aluminum	TS-2	2	1.09	2.57	0.48
C-modified	$[0]_8$	Aluminum	TS-2	2	0.83	0.75	0.08
Experiment							
L	$[0]_8$	Aluminum	RA(3)	2	0.96	0.38	0.42
C	$[0]_8$	Aluminum	RA(3)	2	0.97	0.83	0.09

Table 3.12: Spring-in variation with part shape for steel tool. COMPRO predictions are compared with experimental results.

Part Shape	Lay-up	Tool Material	Tool Surface	Cure Cycle	Spring-in		
					Corner	Warpage	
						Web	Flange
COMPRO							
L	$[0]_8$	Steel	TS-2	2	0.87	0.25	0.25
C	$[0]_8$	Steel	TS-2	2	0.95	1.37	0.28
C-modified	$[0]_8$	Steel	TS-2	2	0.80	0.46	0.07
Experiment							
L	$[0]_8$	Steel	RA(3)	2	0.74	0.29	0.34
C	$[0]_8$	Steel	RA(3)	2	0.81	0.45	0.10

3.8 FIGURES
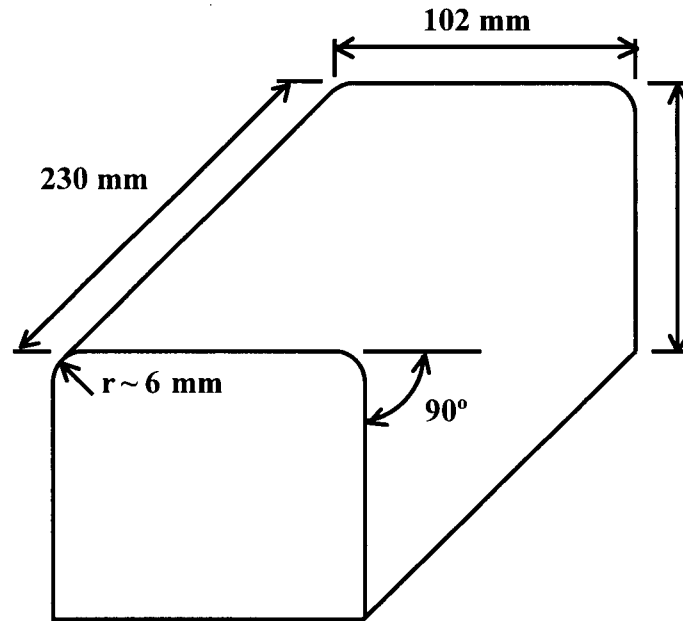
Figure 3.1: Tool geometry used in the experiment (Albert, 2001).

(a)   (b)
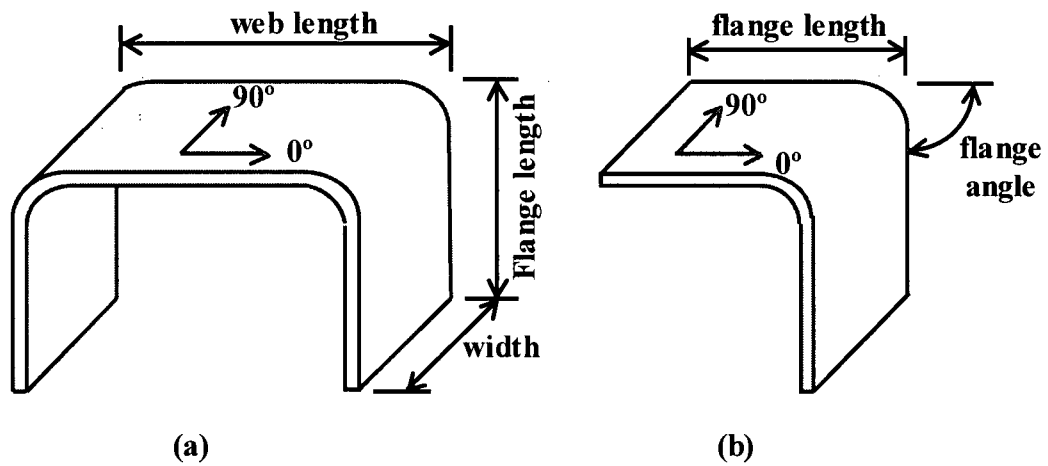
Figure 3.2: Part geometries used in the experiment (a) C-shaped (b) L-shaped (Albert, 2001).
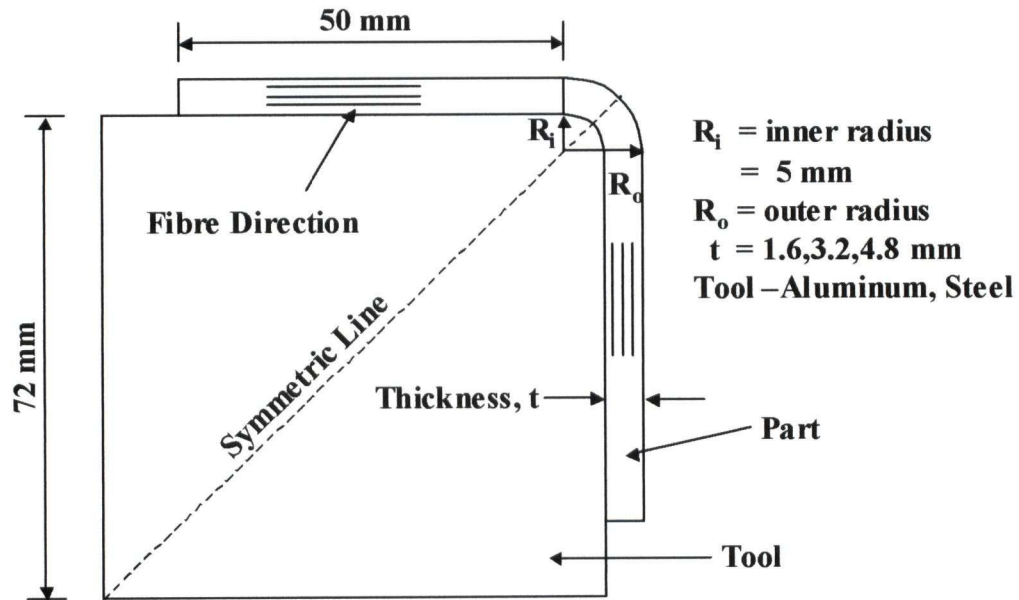
Figure 3.3: The geometry of the L-shaped composite part and the tool used in modelling.
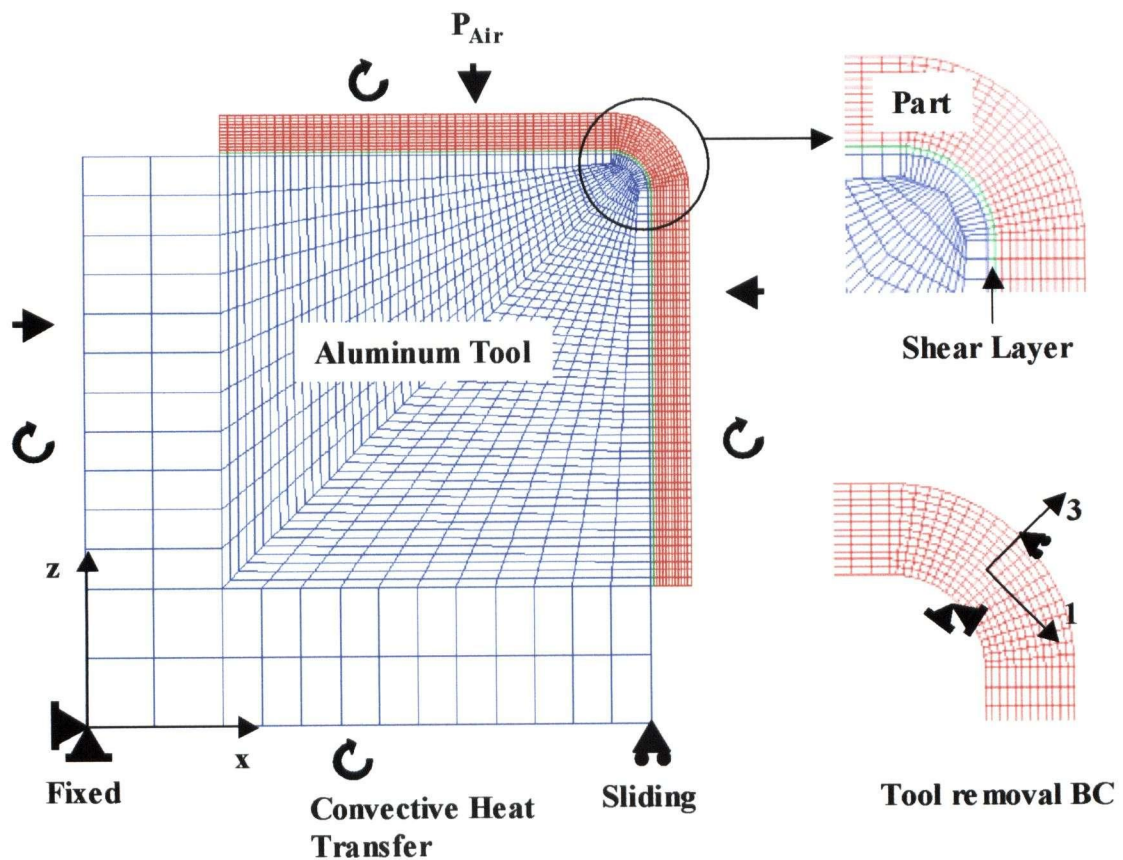
Figure 3.4: Finite element representation of the angle laminate and the boundary conditions applied.
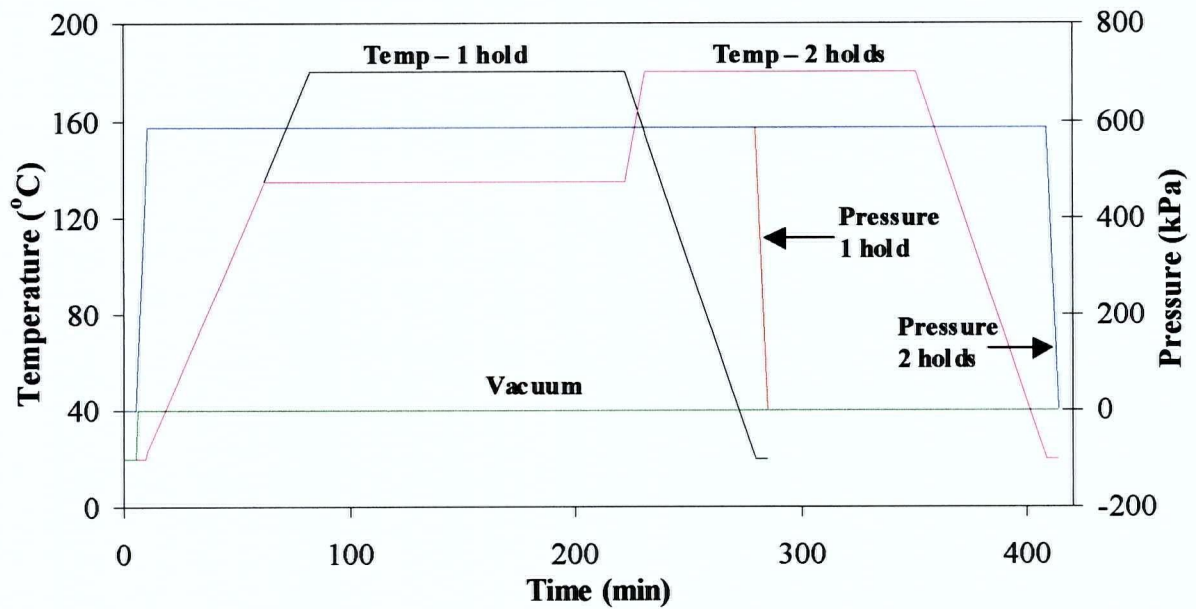
Figure 3.5: Target cure cycles used in autoclave processing of the L-shaped part. Both one and two hold cure cycles (similar to the ones used by Albert, 2001) are used.
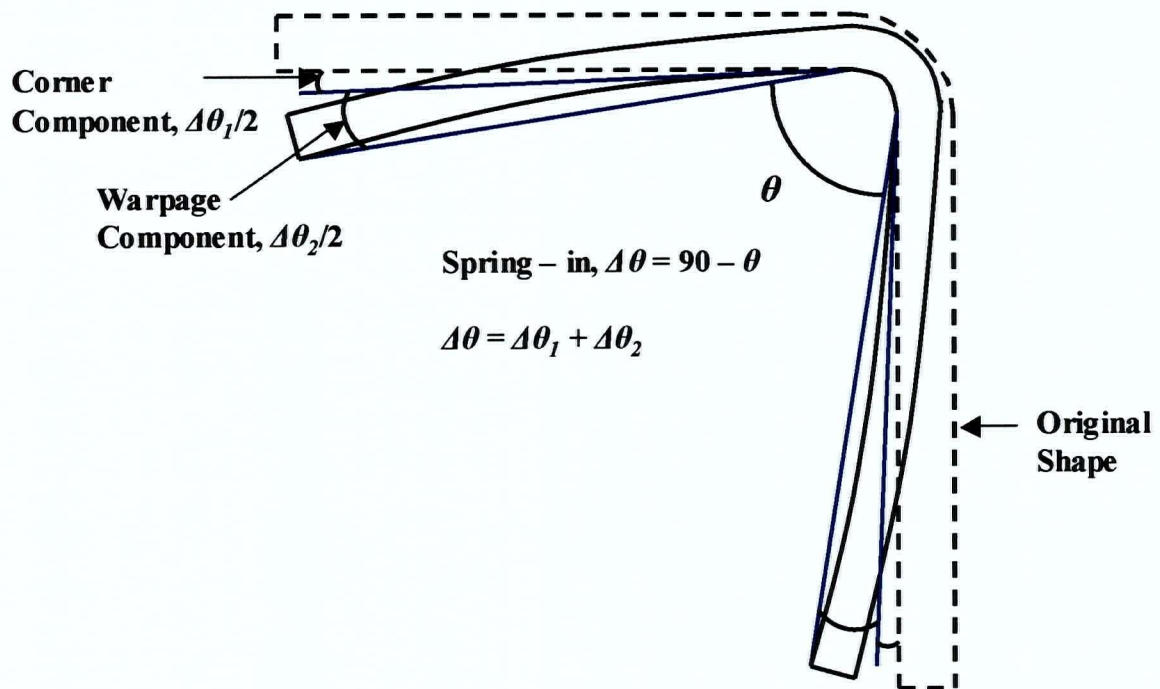
Figure 3.6: Measurement of spring-in of the L-shaped part.
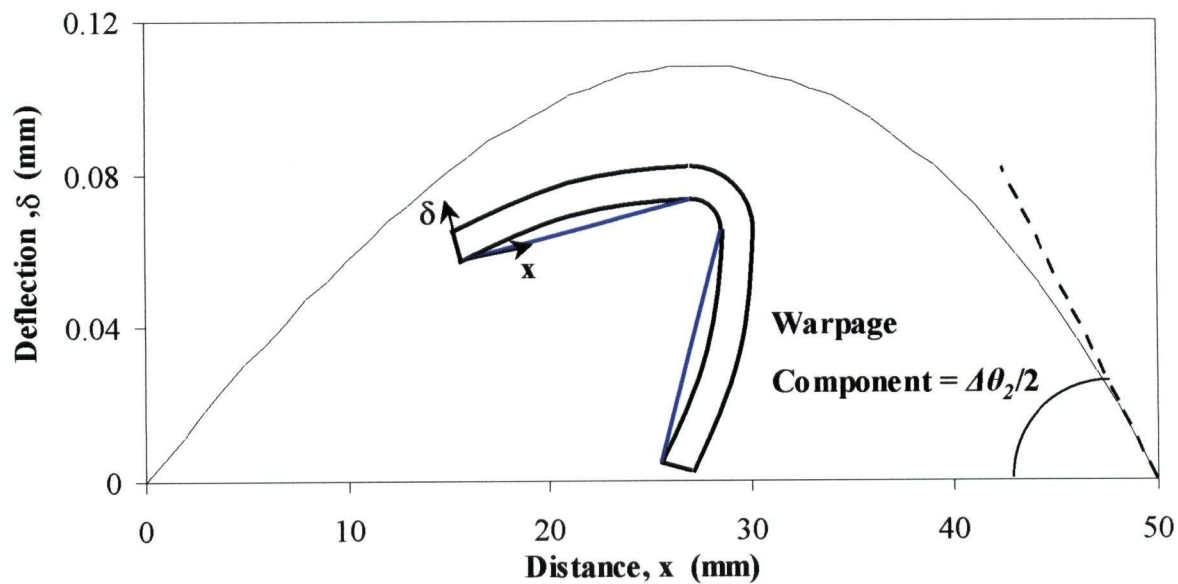
Figure 3.7: Predicted flange warpage profile of a 16-layer L-shaped part.
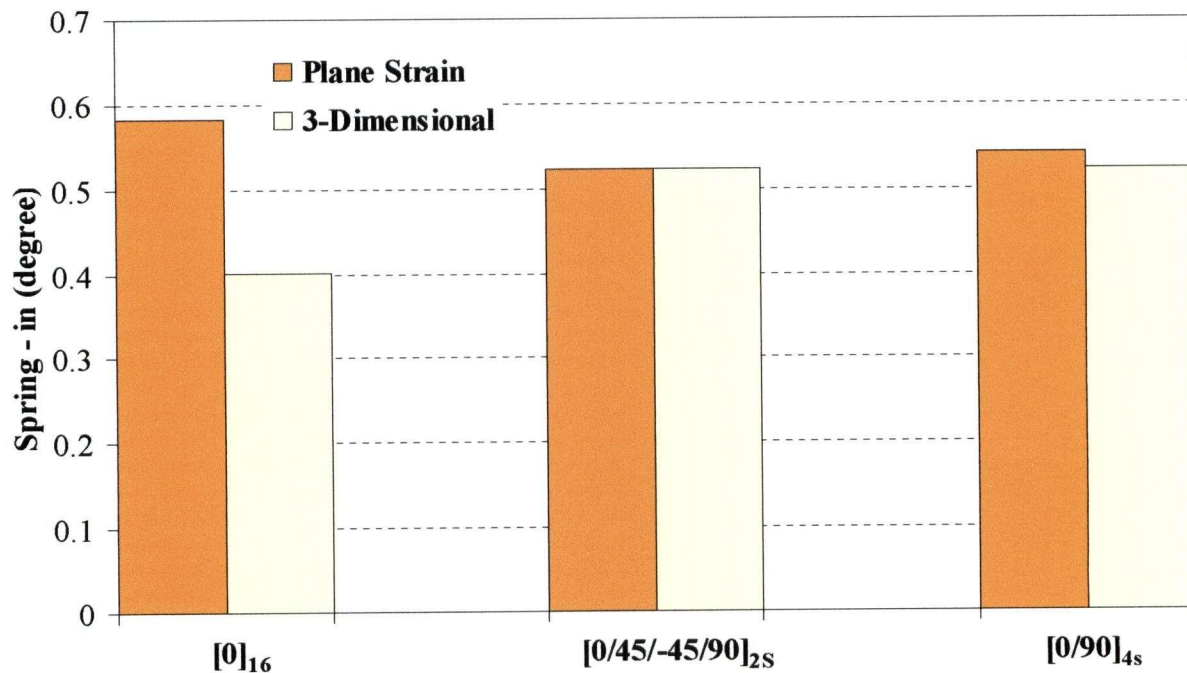
Figure 3.8: Comparison of spring-in prediction between plane strain and three-dimensional analysis.

(a)

(b)

(c)
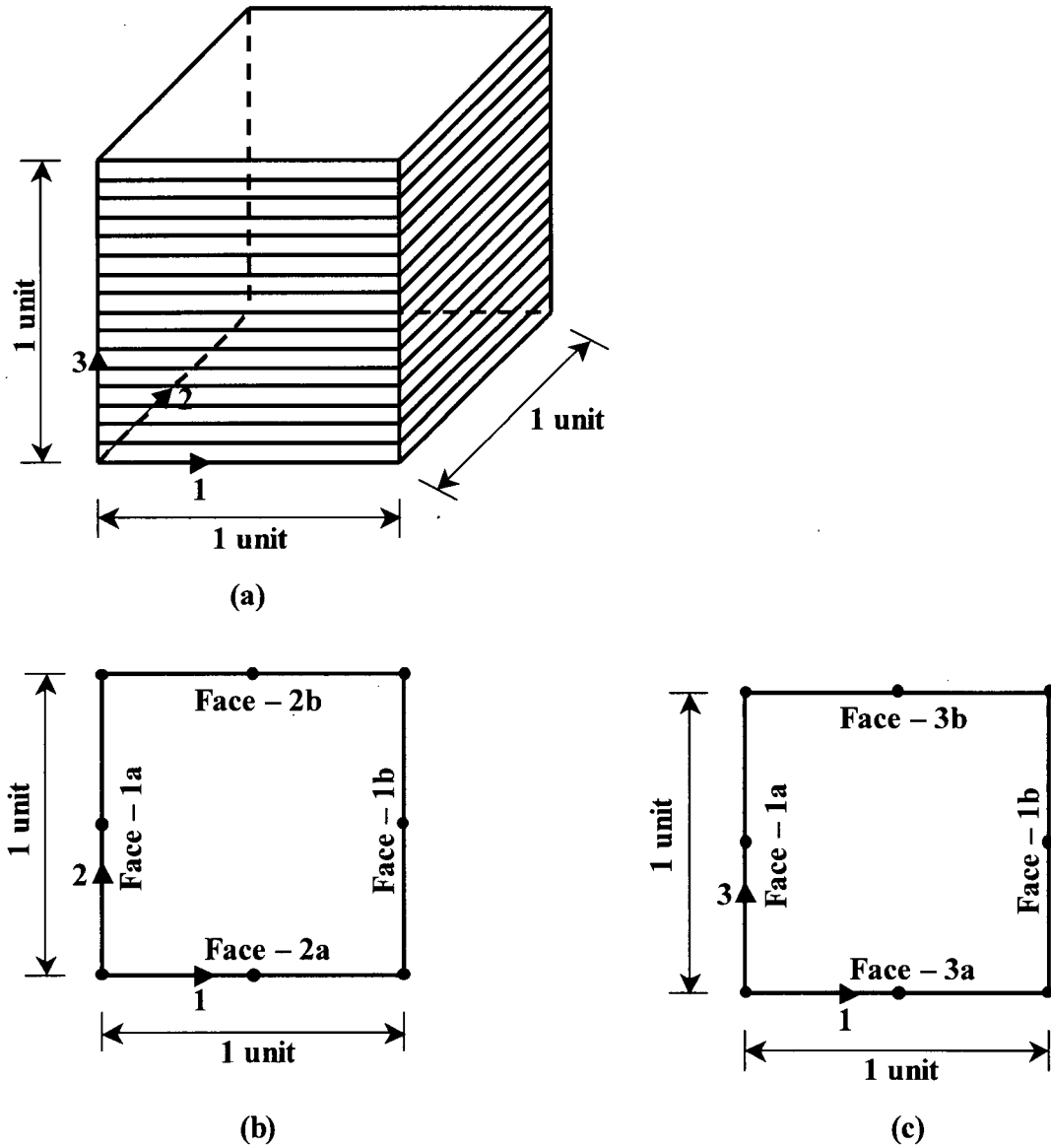
Figure 3.9: Numerical model to predict the equivalent properties of a composite laminate using a 3D elastic analysis. (a) Schematic diagram of a 16-layer composite element (b) & (c) identification of faces for boundary conditions.
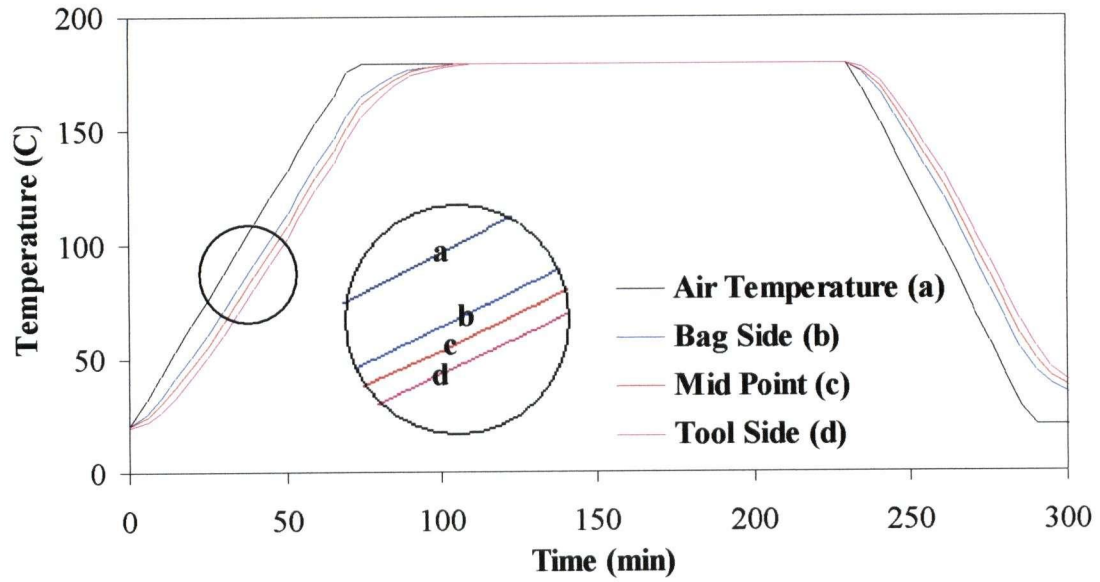
Figure 3.10: Temperature profile through the part thickness.
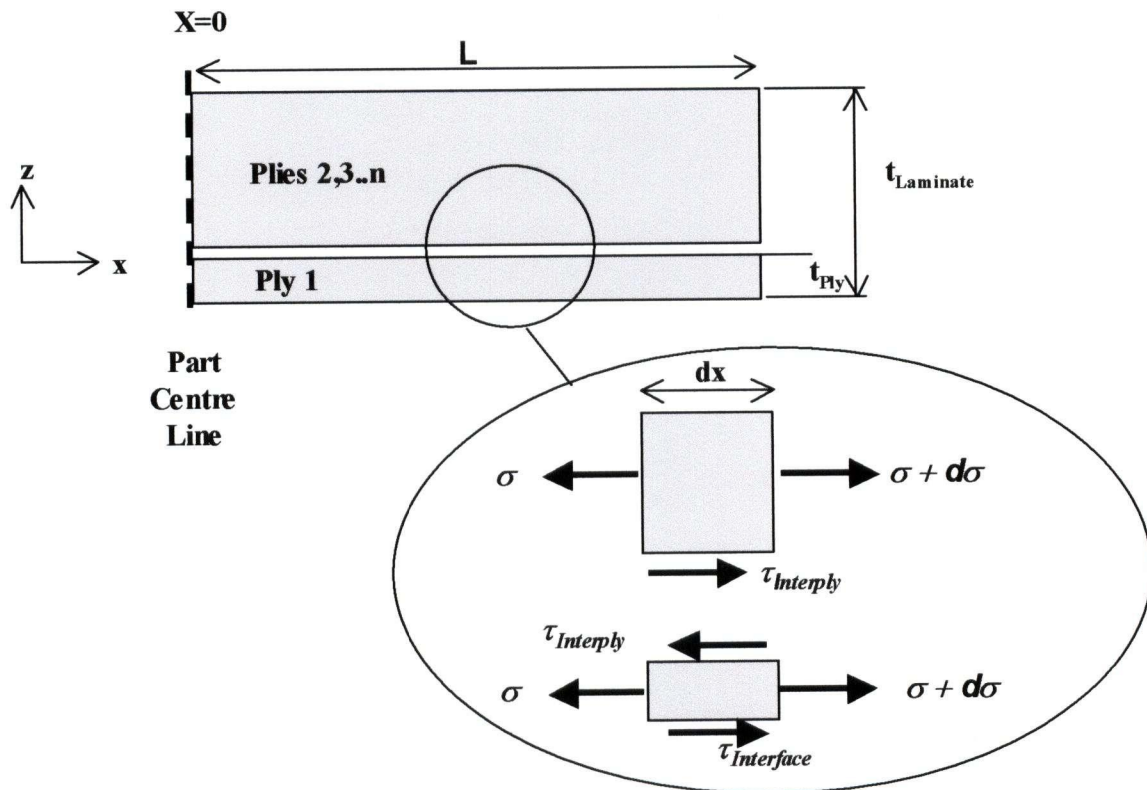
Figure 3.11: Part geometry for the analytical model. Sliding friction occurs at both the tool-part interface and at the interply region (Twigg, 2001).
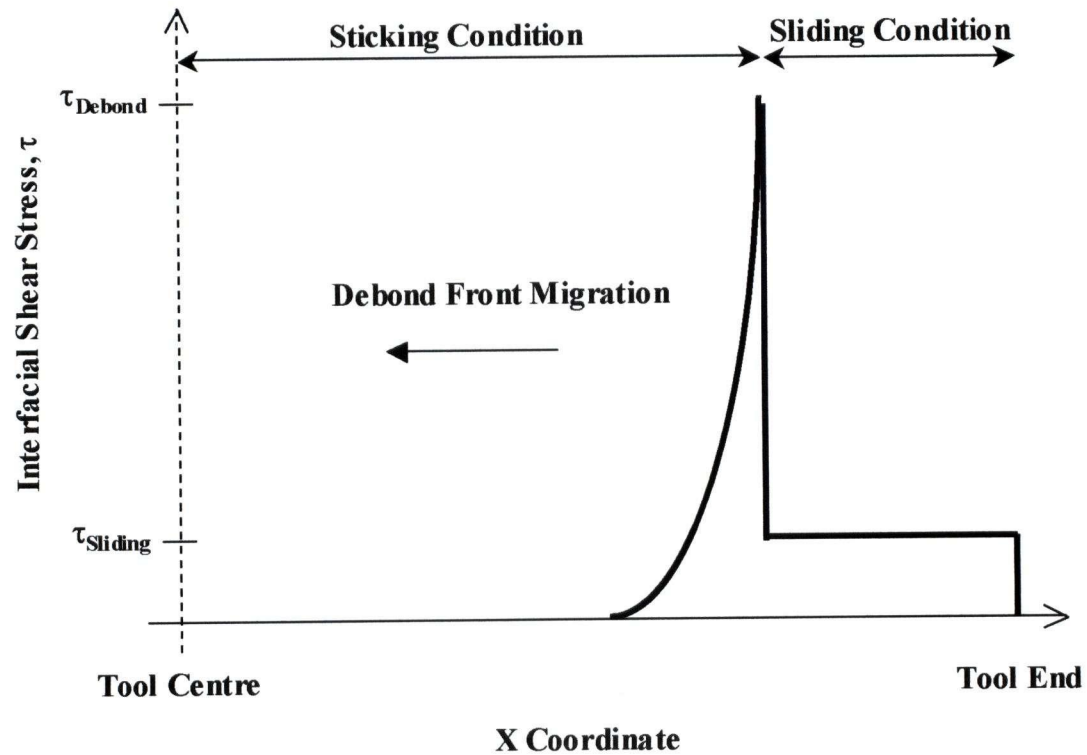
Figure 3.12: Illustration of interfacial shear stress distribution as the debond front travels from the tool end towards the center (Twigg, 2001).
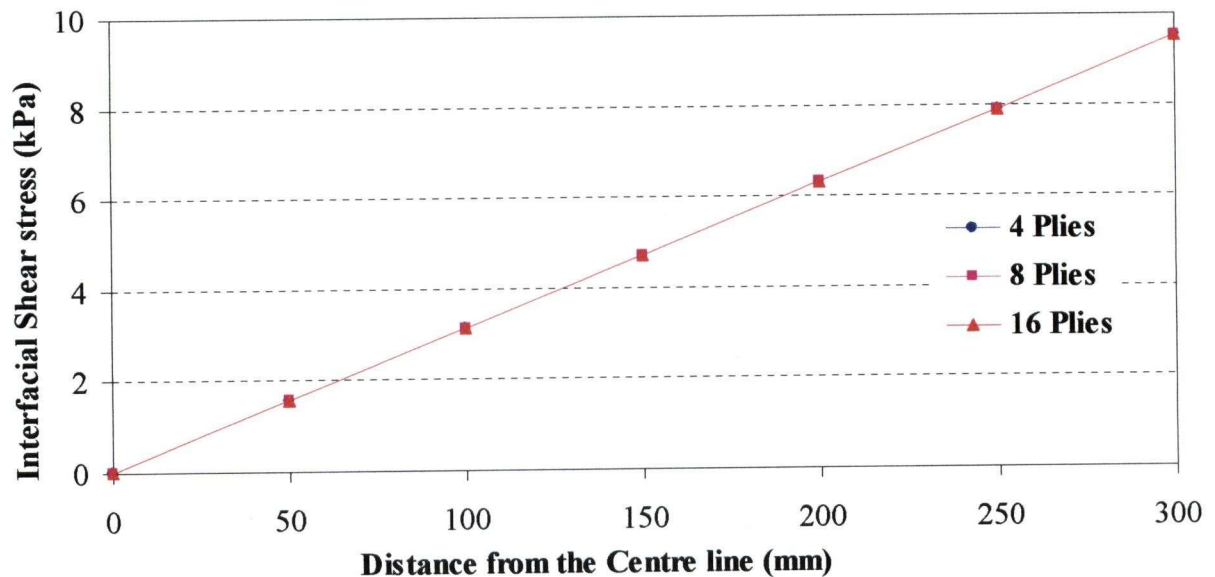
Figure 3.13: The variation of interfacial shear stress distribution with part thickness (600 mm long part with unidirectional layers) according to COMPRO prediction using a shear layer of modulus 6.9 kPa.
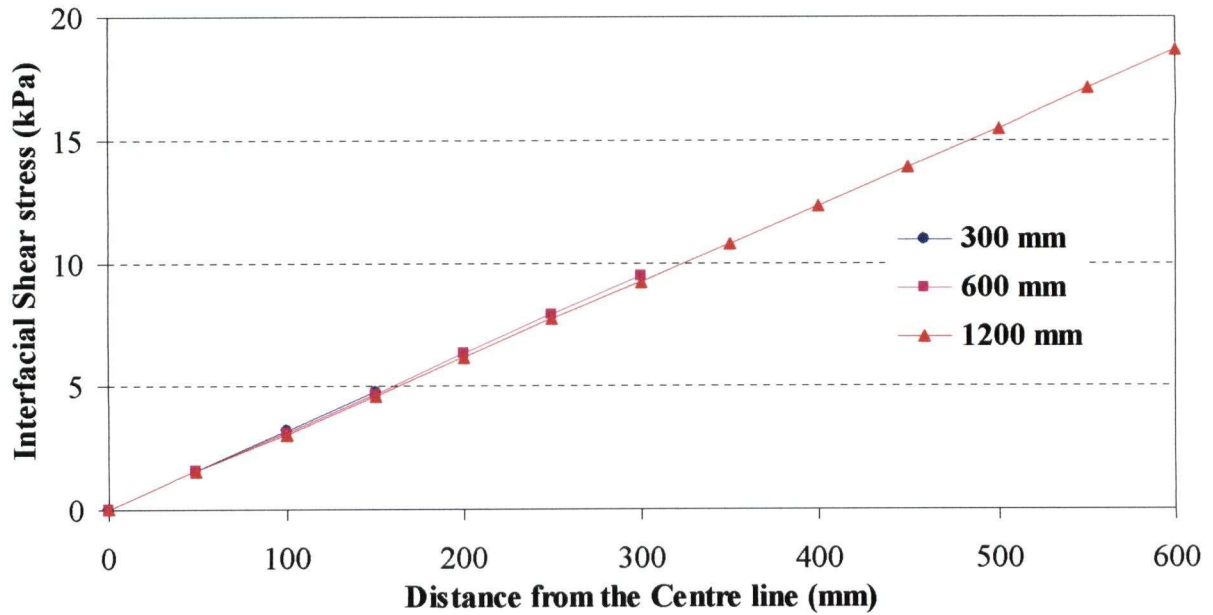
Figure 3.14: **The variation of interfacial shear stress distribution with part length (8 unidirectional layer part) according to COMPRO prediction using a shear layer of modulus 6.9 kPa.**
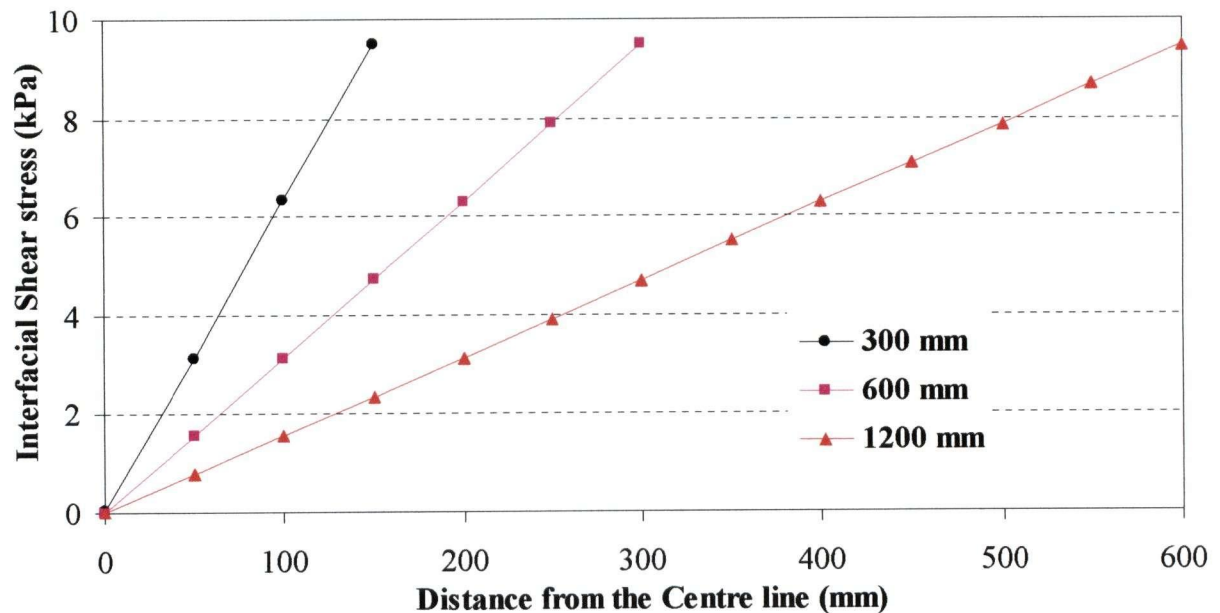
Figure 3.15: **The variation of interfacial shear stress distribution with part length. By modifying the shear layer property with length ratio, the peak shear stresses are made equal (average shear stresses are also equal).**
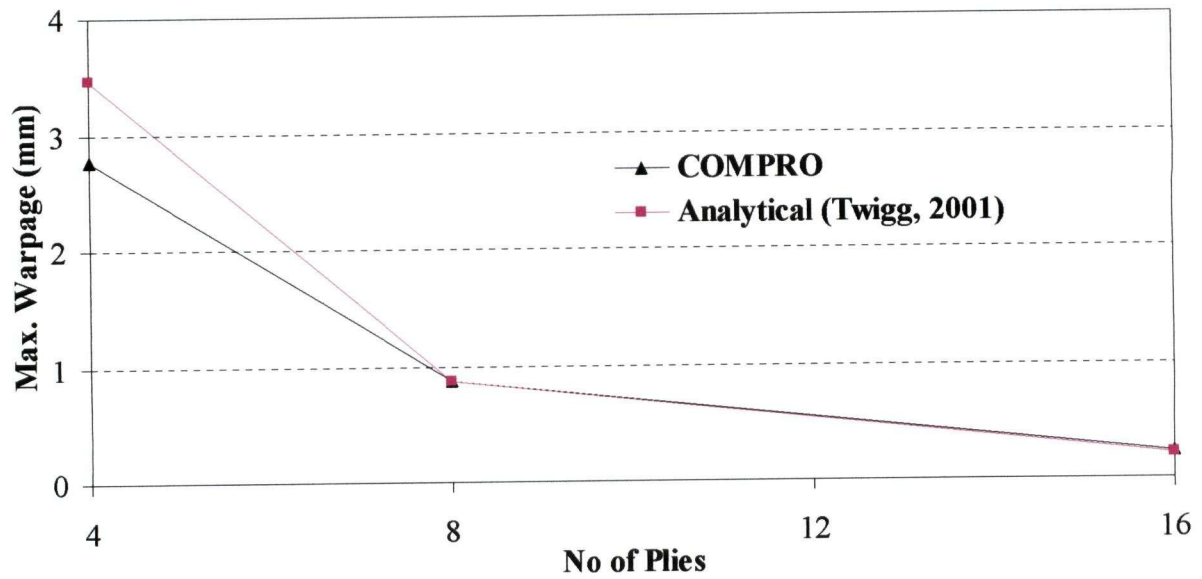
Figure 3.16: The variation of the warpage of a flat part with part thickness. The prediction of COMPRO is compared with the analytical solution proposed by Twigg (2001).
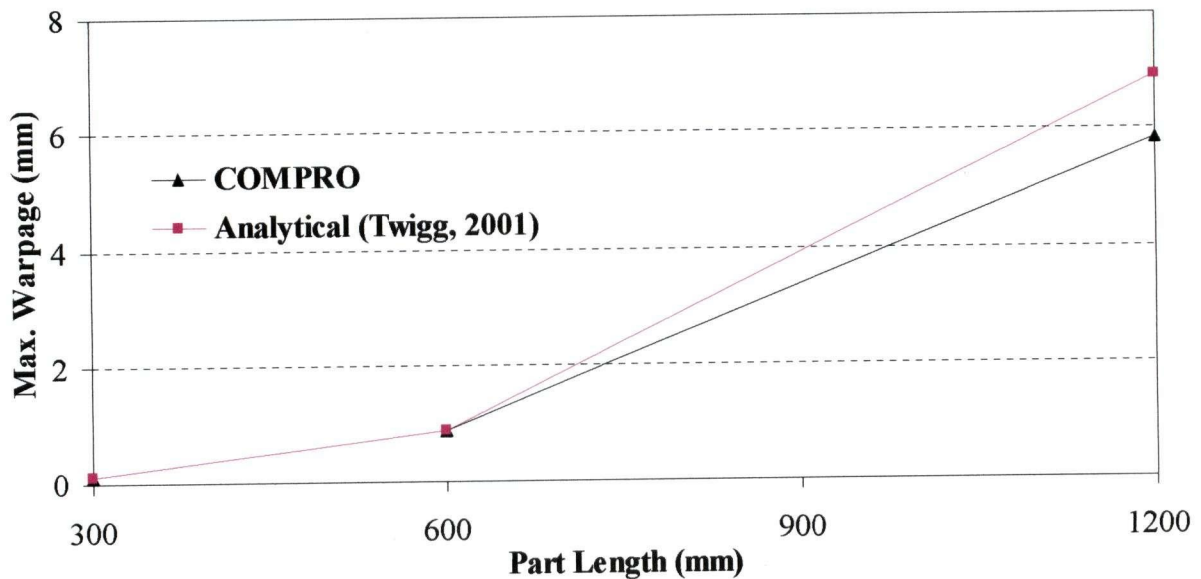
Figure 3.17: The variation of the warpage of a flat part with part length. The prediction of COMPRO, with the shear layer modified by part length ratio, is compared with the analytical solution proposed by Twigg (2001).
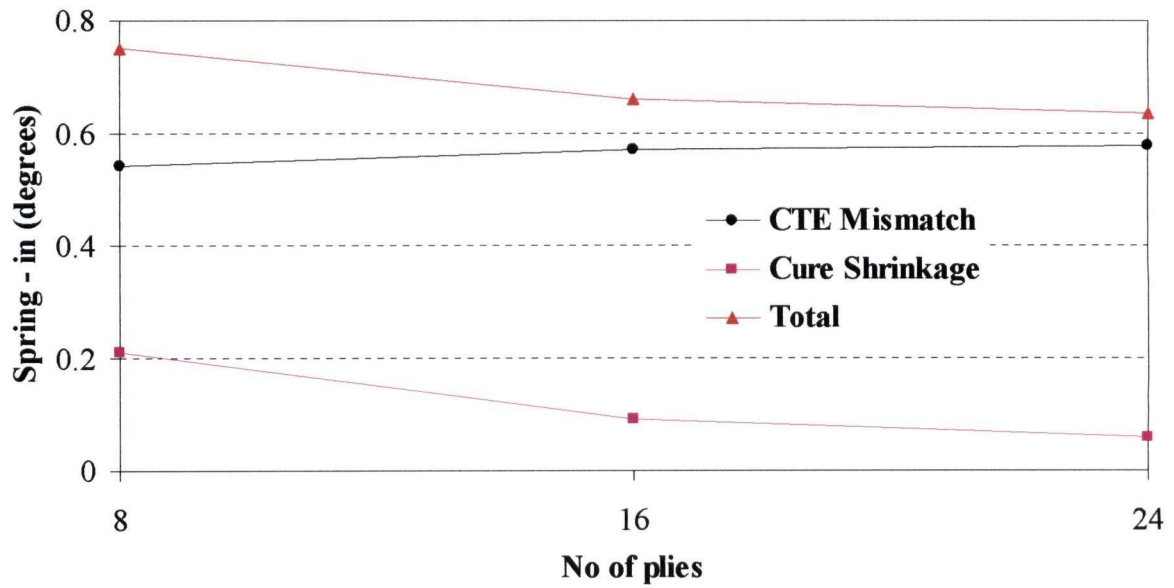
Figure 3.18: Contribution by the CTE anisotropy and cure shrinkage to the total spring-in when the part is constrained by the tool.
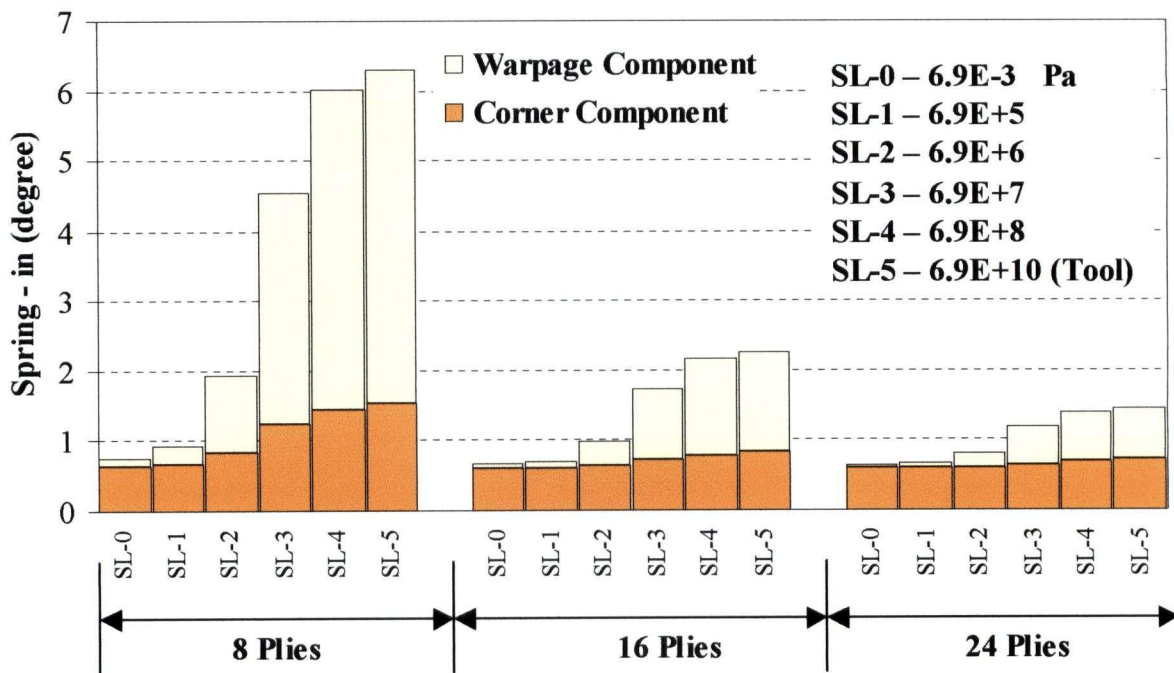
Figure 3.19: Spring-in of the parts with different shear layers. Only the Young's modulus is shown in here although the shear modulus is also changed by the same order.
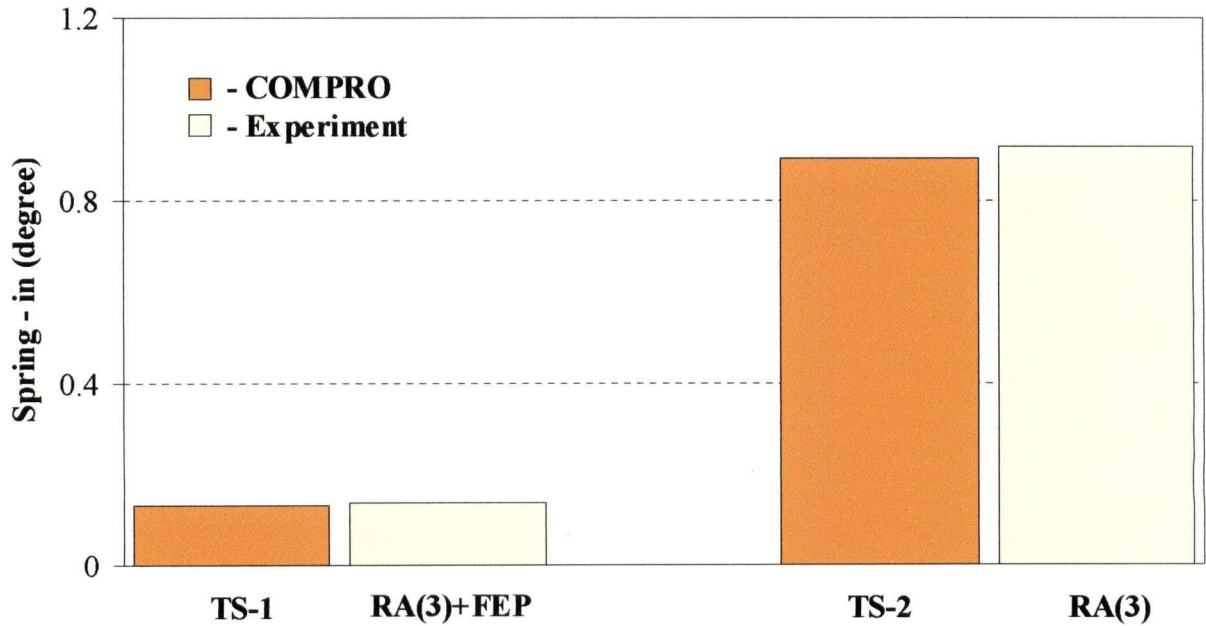
Figure 3.20: Comparison between the predicted and measured warpage components of an 8-layer part to select the appropriate shear layer property to represent the tool surface condition used in the experiment.
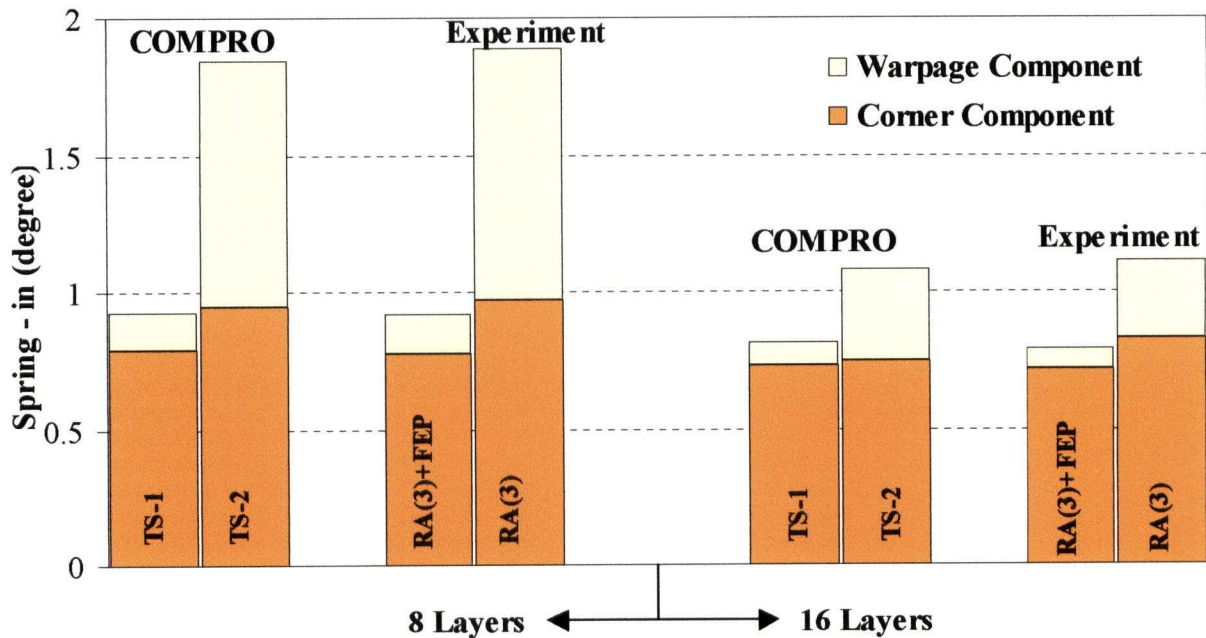
Figure 3.21: Spring-in variation with tool surface condition. COMPRO predictions are compared with experimental results for both 8-layer and 16-layer unidirectional parts.
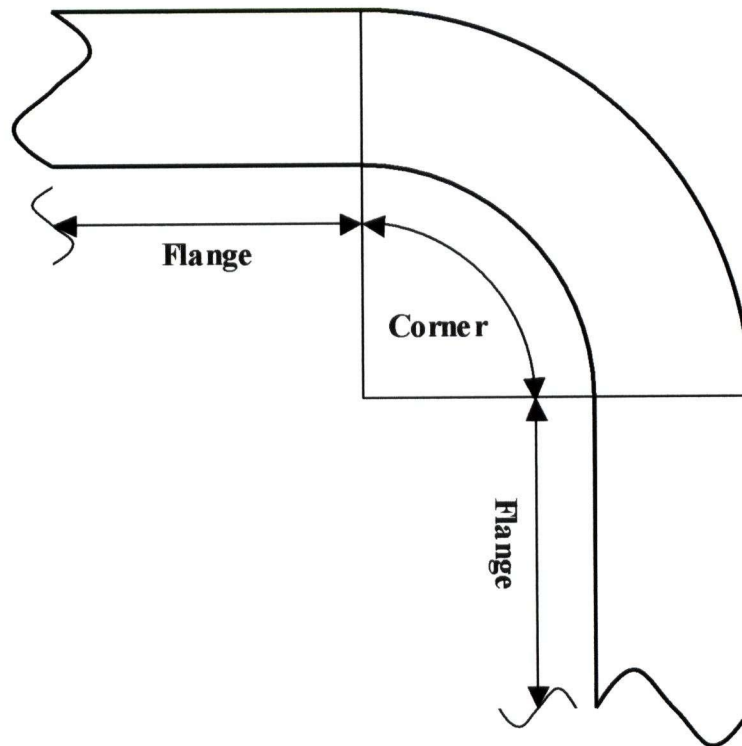
Figure 3.22: Schematic showing the corner and flange components of an L-shaped part.
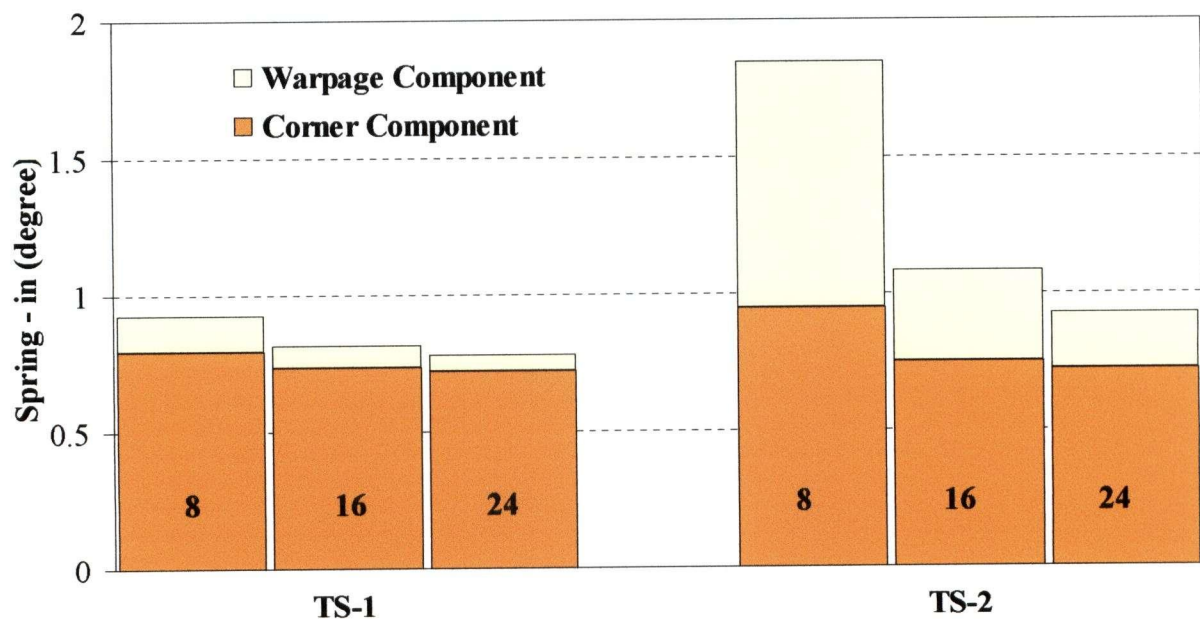
Figure 3.23: Variation of spring-in with part thickness predicted by COMPRO. The results are shown for two different tool surfaces.
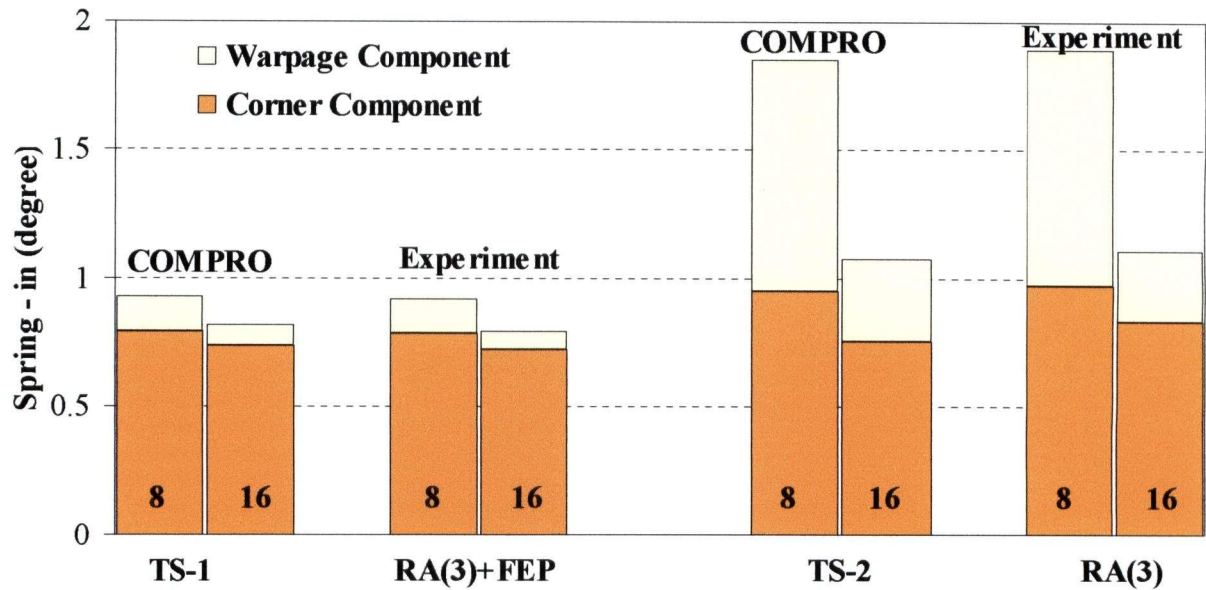
Figure 3.24: Spring-in variation with part thickness. COMPRO results are compared with experimental results for two different tool surface conditions.
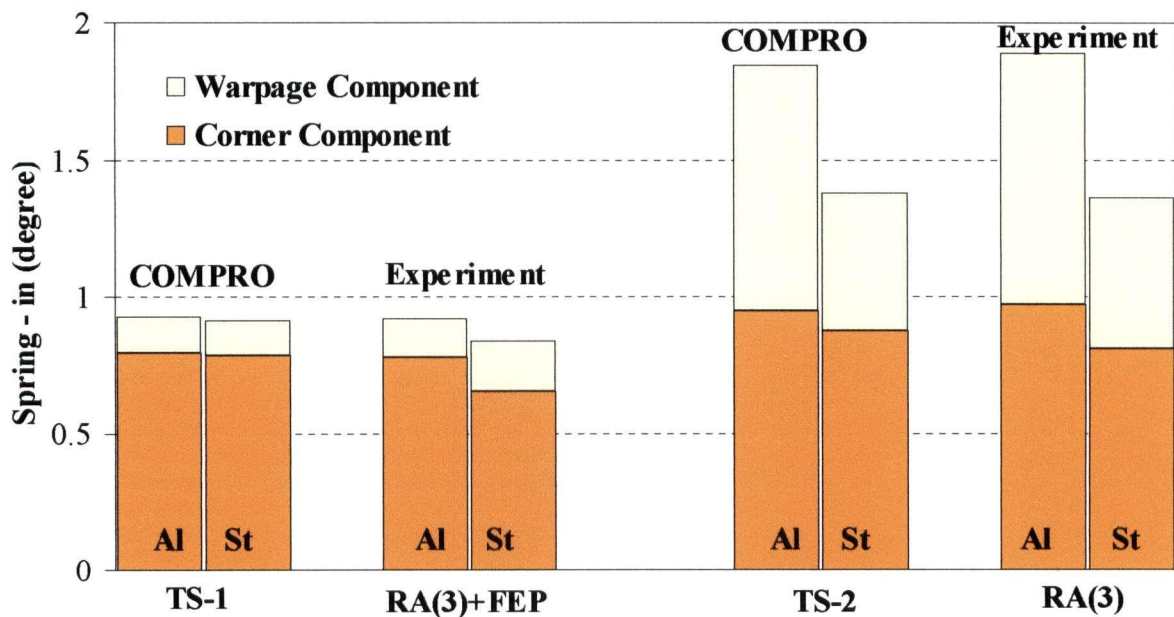
Figure 3.25: Spring-in variation with tool material for an 8-layer unidirectional part. COMPRO results are compared with experimental results for two different tool surface conditions.
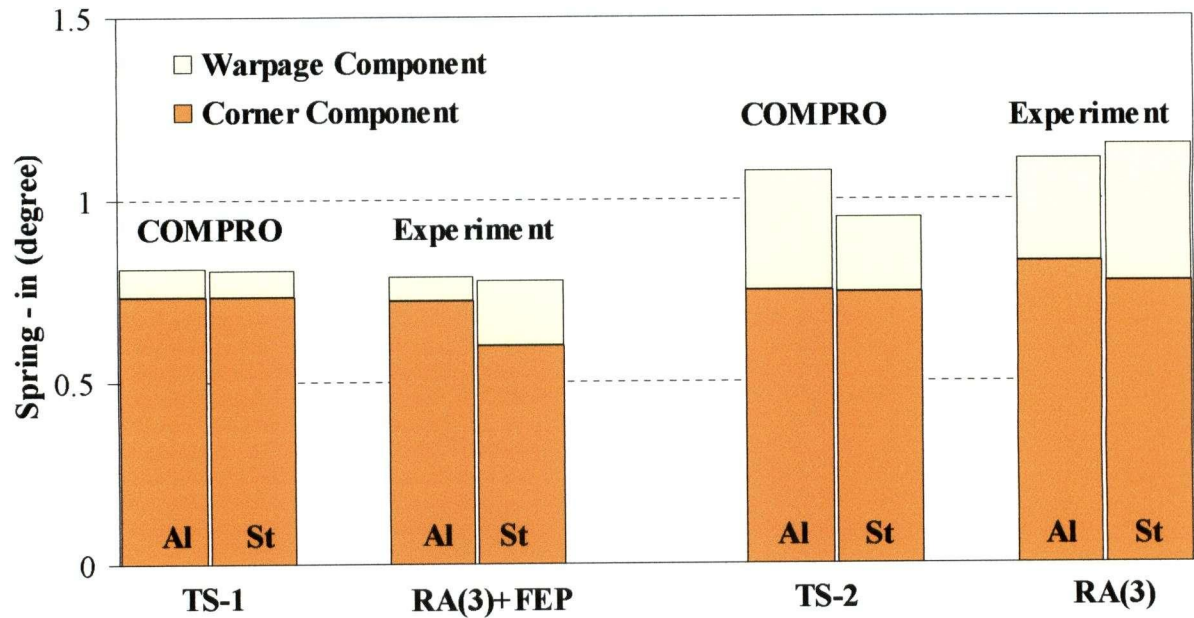
Figure 3.26: Spring-in variation with tool material for a 16-layer unidirectional part. COMPRO results are compared with experimental results for two different tool surface conditions.
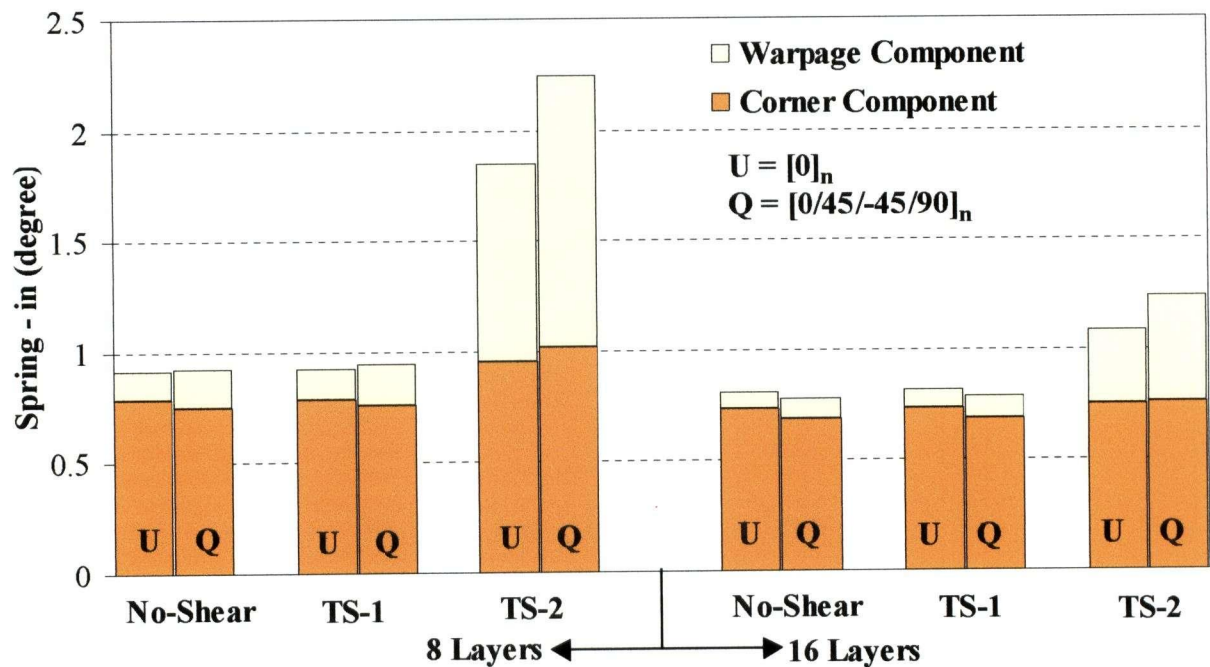
Figure 3.27: The predicted variation of spring-in with part lay-up for two different thickness of the part. The results for three different shear layer properties are also shown. No-Shear indicates that there is minimal tool part interaction.
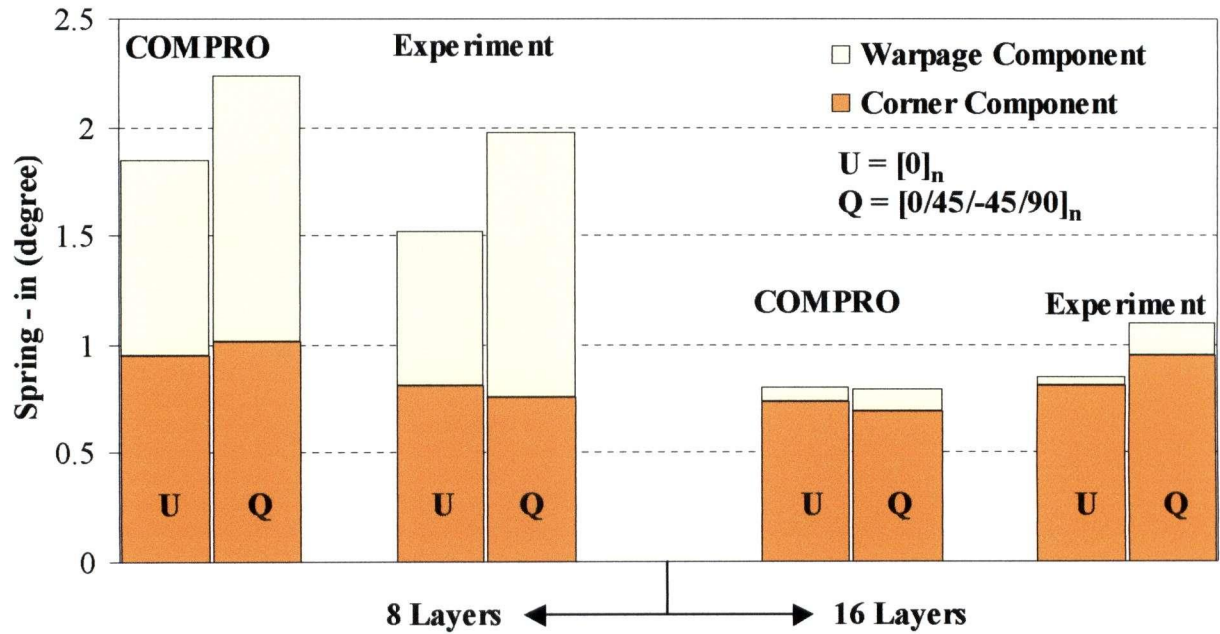
Figure 3.28: Spring-in variation with part lay - up. COMPRO results are compared with experimental results for two different thickness of the part.
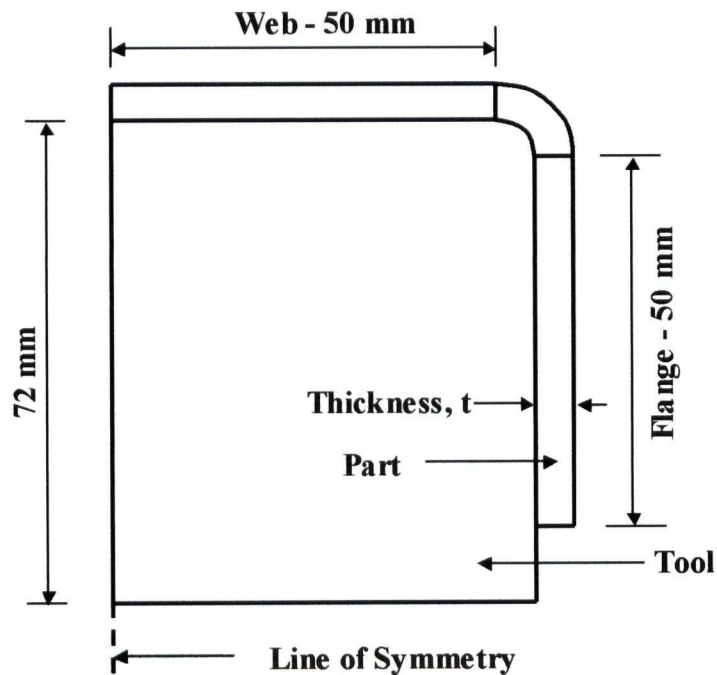
Figure 3.29: The geometry of half of the C-shaped composite part and the tool.
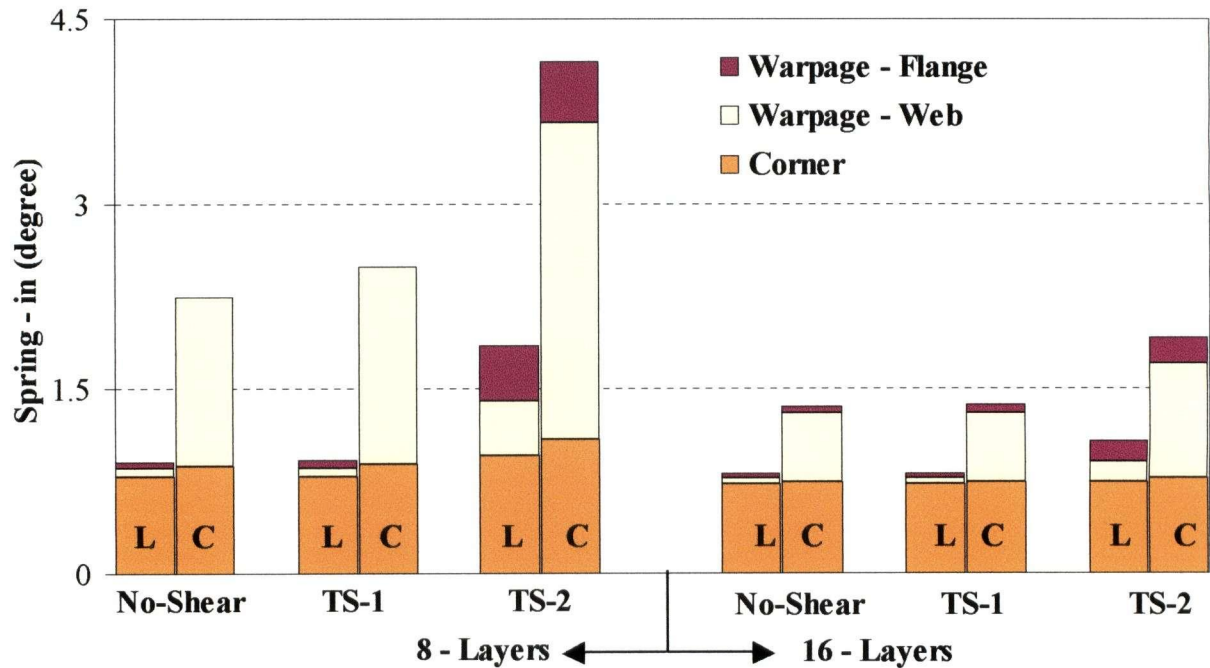
Figure 3.30: Variation of spring-in with part shapes predicted by COMPRO. The results are shown for three different tool surface conditions. No-Shear indicates that there is minimal tool part interaction.
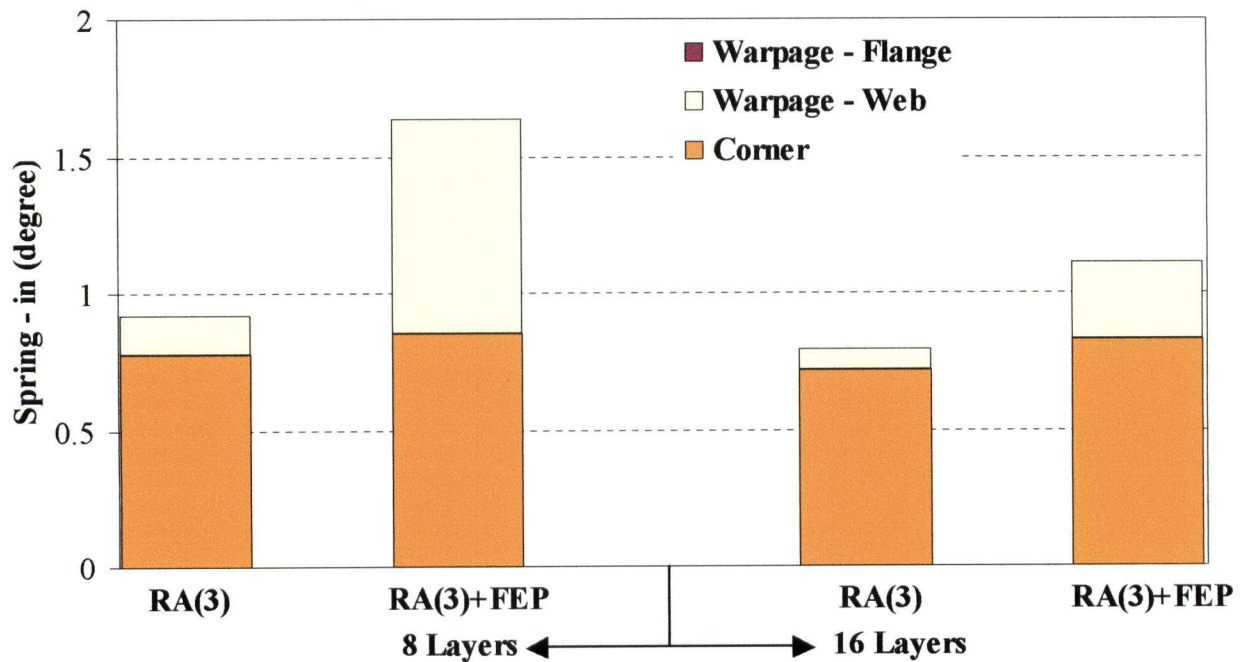
Figure 3.31: The experimentally measured spring-in of C-shaped parts. In all cases, the warpage of the flange is negligible (Albert, 2001).
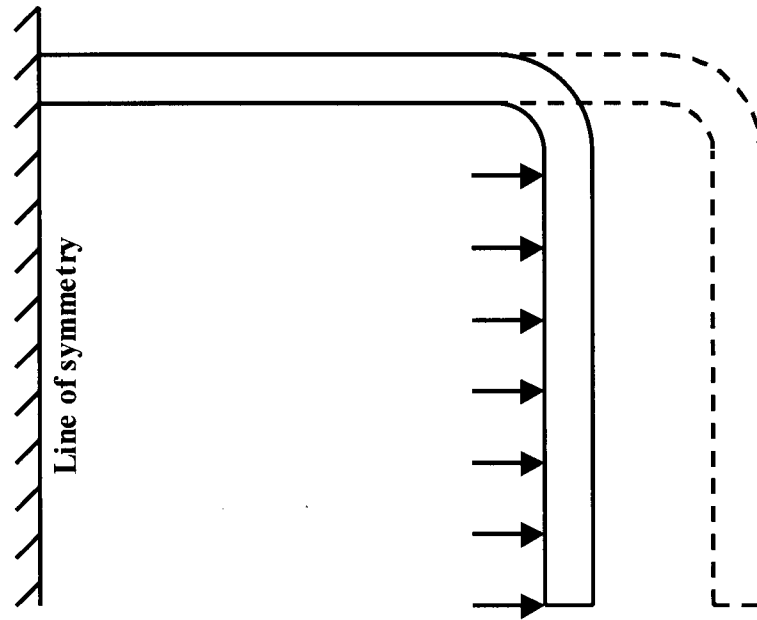
Figure 3.32: Schematic showing stretching of the C-shaped part due to the corner-locking as the tool expands.
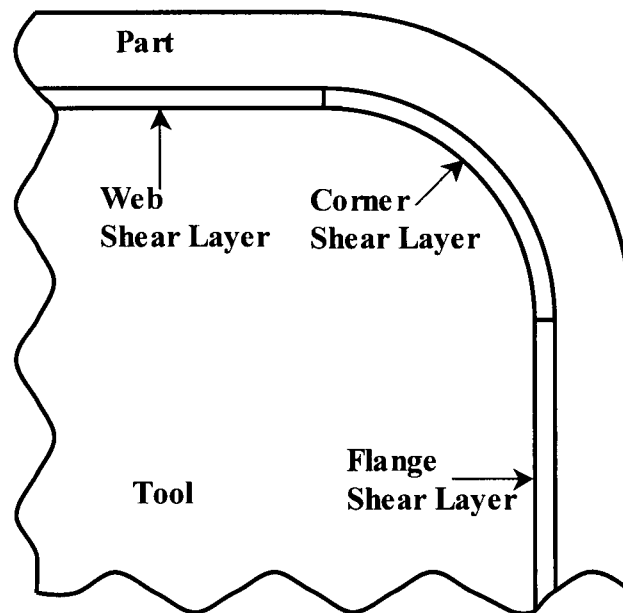
Figure 3.33: Illustration of the three zones of the shear layer used in the modified method to overcome the corner-locking.
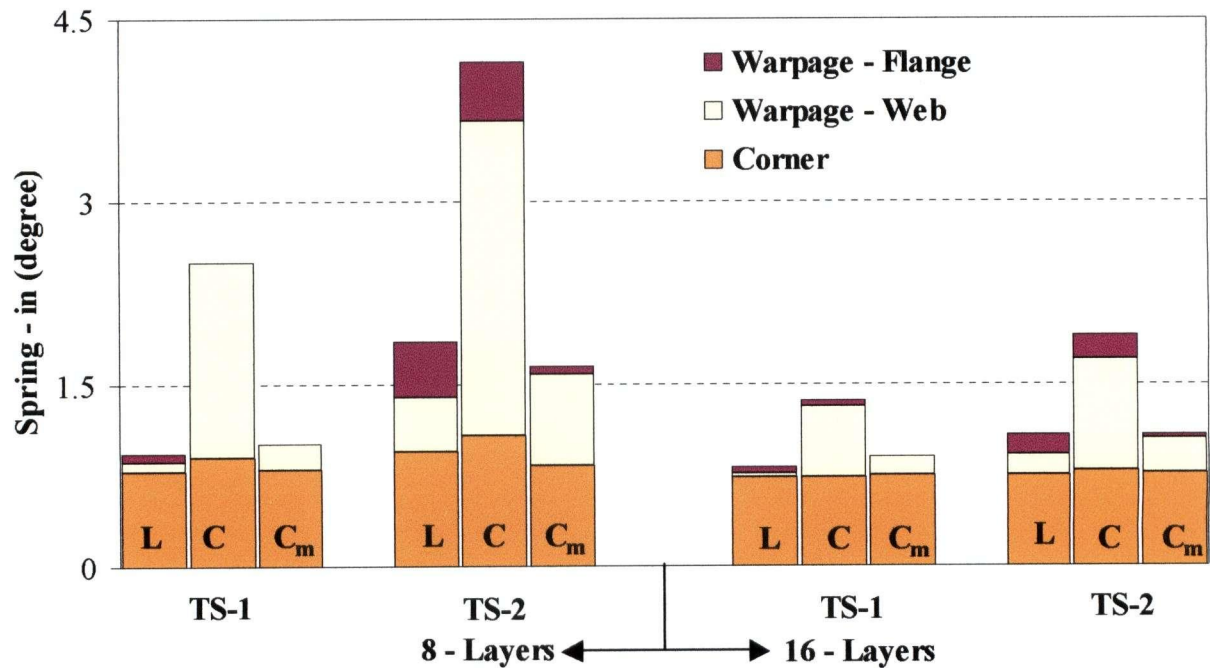
Figure 3.34: Spring-in results by the modified method to overcome the corner-locking problem. C is the original results and C_m is the modified results.
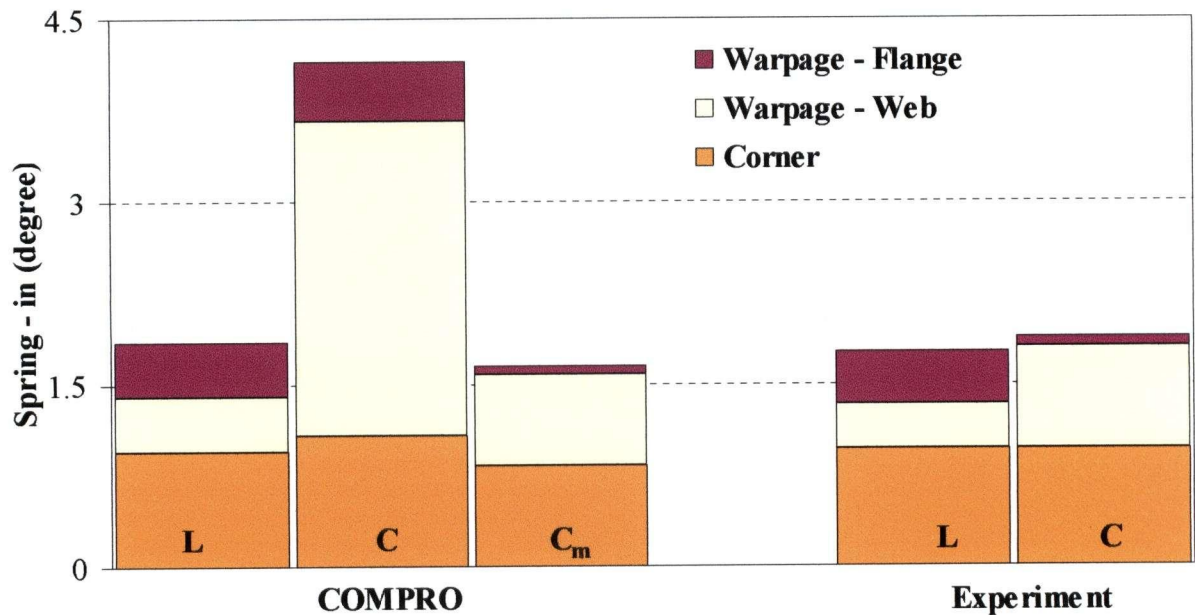
Figure 3.35: Effect of part shape on spring-in. COMPRO predictions by both the original method (C) and the modified method (C_m) are compared with experimental results for aluminum tool.
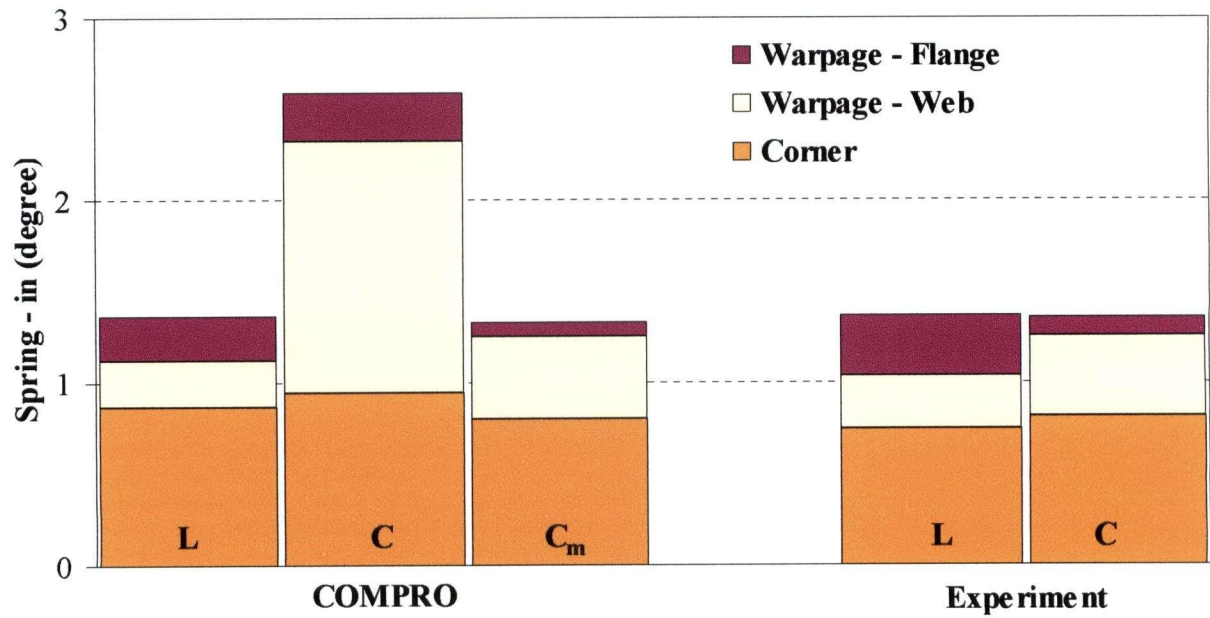
Figure 3.36: Effect of part shape on spring-in. COMPRO predictions by both the original method (C) and the modified method (C_m) are compared with experimental results for steel tool.

CHAPTER 4: PROCESS-INDUCED RESIDUAL STRESSES

4.1 INTRODUCTION

In the previous section the intrinsic and the extrinsic parametres that contribute to the residual stresses in a composite part were investigated. Once the part is removed from the tool, these residual stresses are released and cause the L-shaped part to spring in and warp. But due to the changes in the material properties during the curing process, some of the residual stresses will be locked in after the part is released from the tool. Even though this portion of the residual stresses is small compared to the residual stresses that cause the part to spring in, it can potentially elevate the stresses in the composite structure during its service life and lead to its failure sooner than expected.

In addition to the macro-level stresses that develop at the laminate-level, there will be micro-level stresses at the ply-level. Micro-level stresses are defined as those stresses that develop between the fibre and matrix as a result of thermal expansion coefficient mismatch and the resin shrinkage during curing. These stresses are complicated due to the complex arrangements of the fibres in the matrix in a ply. But these stresses are generally self-equilibrating and do not contribute to the macro-level deformations. Although micro-level stresses do not contribute to the macro-level deformation, they may lead to reduction of strength and initiation of cracking. Since the experimental methods are complicated and expensive, the simplest way to evaluate the process-induced micro-level residual stresses is to use numerical methods.

Wagner and Nairn (1997) proposed a simple concentric cylindrical model to predict the thermal stresses in a composite material. This model is similar to the model used by Rosen and Hashin (1964) to predict the mechanical properties of composite materials.

Several researchers used the finite element approach to analyse the thermal stresses in a composite material (Bowles et al., 1991; Hyer, 1997). In all these analyses, only the stresses due to thermal mismatch are considered and the resin properties are assumed to be either constant or temperature dependent. Chen et al. (2001) used a viscoelastic micromechanical model to calculate the residual stresses induced during the curing process. In this work, only the stresses due to thermal mismatch were considered.

In this section the residual stresses due to thermal mismatch, cure shrinkage and mechanical load at the micro-level in a specific lamina (Figure 4.1) of the previously studied L-shaped part are investigated.

4.2 MICROMECHANICAL FINITE ELEMENT MODELLING

In a composite lamina, the actual fibre arrangement is random. But for simplicity, the fibres are assumed to be arranged in a periodic manner so that a representative volume element (RVE) can be identified and analysed separately. The commonly used periodic arrangements of fibres are square-packed and hexagonal-packed arrays. The names of the arrays are derived from the shape of the polygons that describe the repeating fibre-packing pattern as shown in Figure 4.2. The hexagonal-packed array is the preferred model since it closely represents the actual fibre arrangement as shown in Figure 4.3. If a load is applied in the fibre direction, each fibre will respond in the same way as its neighbouring fibres, since the fibres are embedded in a vast array. So the analysis can be focused only on the RVE that represents the whole fibre-matrix system.

The RVE has the same fibre volume fraction and material properties as the lamina. In this study, a unidirectional ply with continuous fibres is considered and the following assumptions are made:

- The fibres are circular in cross section and continuous in the longitudinal direction

- The fibres are arranged in a periodic square or hexagonal array

- The fibre properties are isotropic and constant (do not change with temperature)

- The matrix is cure hardening instantaneously linear elastic (CHILE) as it is in COMPRO

- The displacements are continuous across the fibre/matrix interface (perfect bonding)

- The temperature is uniform throughout the body

- The applied load is uniform over the area of application

The RVE for square-packed and hexagonal-packed arrays are shown in Figure 4.4 and the corresponding finite element mesh is shown in Figure 4.5. The dimension of the unit cell in the axial direction (1) is not important, since the stresses and strains are independent of the axial coordinate. So the axial dimension is chosen to keep the element aspect ratio below 2 (here the axial dimension is taken to be 0.25 units). Due to the symmetry, only a quarter of the RVE is considered. The analysis is performed using the commercial finite element software ABAQUS. 20-noded isoparametric solid elements are used for the analysis. Mesh sensitivity and convergence of the finite element solution is examined by dividing each element into four as shown in Figure 4.5(b).

4.3 BOUNDARY CONDITIONS

Because of the periodicity, the straight lines outlining the unit cells in Figure 4.6 remain straight when the composite is subjected to normal loading (tensile, compressive) and temperature change. Symmetry boundary condition implies that the corresponding displacement component at that boundary and in the direction normal to that boundary is zero and the couple boundary condition (all the nodes along this boundary are coupled with each other to deform by the same amount in a specified direction) implies that the corresponding displacement component at that boundary and in the direction normal to that boundary is constant. A summary of the boundary conditions is given below (x_1, x_2 and x_3 are any arbitrary distances from the origin in 1, 2 and 3 directions respectively):

$u(0, x_2, x_3) = 0$	-	Symmetry - 1
$u(0.025, x_2, x_3) = $ constant	-	Couple - 1
$v(x_1, 0, x_3) = 0$	-	Symmetry - 2
$v(x_1, 1, x_3) = $ constant	-	Couple - 2
$w(x_1, x_2, 0) = 0$	-	Symmetry - 3
$w(x_1, x_2, 1) = $ constant	-	Couple - 3

The couple boundary is applied using the EQUATION option in ABAQUS. The boundary conditions are shown schematically in Figure 4.6.

4.4 MATERIAL MODELLING IN ABAQUS

Three types of material properties are necessary for the calculation of stresses: elastic constants, thermal expansion coefficients and cure shrinkage coefficients. All materials are assumed to be instantaneously linear elastic i.e. although the material properties vary throughout the processing,

at any given instant it behaves as a linear elastic material. The material properties of the fibre and the matrix are given in Appendix A (Full details of the material can be found in Johnston (1997)).

Elastic constants of the transversely isotropic fibre are assumed to vary linearly with temperature. For AS4 fibre material, the properties remain constant with the temperature. The isotropic matrix resin is modelled as a cure hardening instantaneously linear elastic material. This means the resin modulus is assumed to be linear elastic at any given time and the modulus increases with the degree of cure. As implemented in COMPRO, in this case too, the heat transfer and the cure kinetics equations are solved independently (Johnston, 1997). Since consideration is given to a single ply in the L-shaped part, the temperature-time history of this ply is imported from COMPRO and a uniform temperature is assumed throughout the fibre and the matrix. The temperature history is shown in Figure 4.7. In COMPRO, the cure kinetics equation (Equation 4.1) is solved by Backward Euler method. But in this case, the equation is solved by Forward Euler method to avoid iteration (Equation 4.2).

$$\frac{d\alpha}{dt} = \frac{K\alpha^m (1-\alpha)^n}{1 + e^{C\{\alpha - (\alpha_{C0} + \alpha_{CT}T)\}}} \tag{4.1a}$$

$$K = Ae^{-\Delta E / RT} \tag{4.1b}$$

where α Resin degree of cure

T Resin temperature

H_R Total resin heat of reaction ($\alpha = 0$ to 1)

A Pre-exponential factor

ΔE Activation energy

m, n Exponent parameters

R Gas constant

C, α_{C0}, α_{CT} Diffusion constants

$$\frac{(\alpha_{i+1} - \alpha_i)}{\Delta t} = \frac{K_i \alpha_i^m (1-\alpha_i)^n}{1 + \exp\{C(\alpha_k - \alpha_{C0} - \alpha_{CT} T_i)\}}$$

$$K_i = Ae^{-\Delta E/RT_i}$$

(4.2a)

$$\alpha_{i+1} = \Delta t \left[\frac{K_i \alpha_i^m (1-\alpha_i)^n}{1 + \exp\{C(\alpha_i - \alpha_{C0} - \alpha_{CT} T_i)\}} \right] + \alpha_i$$

(4.2b)

The accuracy of the results depends on the time step taken: the smaller the time step the more accurate the results. The time step used in COMPRO vary from 1 second to 100 seconds (user can define the minimum and the maximum time step). COMPRO increases and reduces the time step according to the change in α. The degree of cure calculation using the forward Euler method with the time steps of 10 min, 5 min and 2 min are compared with the results of COMPRO in Figure 4.8. A Δt of 2 min is used in the subsequent calculations.

The resin modulus development during curing is calculated according to Equation 4.3 (Johnston, 1997).

$$E_r = E_r' [1 + a_{Er}(T - T_0)]$$

$$E_r' = E_r^0 \qquad\qquad\qquad\qquad\qquad\qquad T^* < T_{C1}^*$$

$$E_r' = E_r^0 + [(T^* - T_{C1}^*)/(T_{C2}^* - T_{C1}^*)](E_r^\infty - E_r^0) \qquad T_{C1}^* < T^* < T_{C2}^*$$

$$E_r' = E_r^\infty \qquad\qquad\qquad\qquad\qquad\qquad T^* > T_{C2}^*$$

(4.3)

$$T^* = (T_g^0 + a_{Tg}\alpha) - T$$

$$T_{C1}^* = T_{C1a}^* + T_{C1b}^* T$$

where

α The resin degree of cure

E_r^0 The resin elastic modulus at very low degrees of cure

E_r^∞ The resin elastic modulus at T_0 and $\alpha = 1.0$

T Resin temperature

T^* Difference between resin temperature and resin instantaneous T_g

T_{ga} Glass transition temperature at $\alpha = 0$

T_{gb} Factor expressing the degree of cure dependence of resin glass transition temperature

T_{C1a} T^* above which resin modulus begins to increase at $T = 0$ K

T_{C1b} Factor expressing the temperature dependence of the T^* above which resin modulus begins to increase

T_{C2} T^* above which resin modulus has reached its full value

T_0 Resin modulus development reference temperature

a_{Er} Factor expressing the temperature dependence of resin modulus

The resin modulus development model is implemented using the UFIELD subroutine in ABAQUS. The ABAQUS calculation is verified by a simple spreadsheet calculation throughout the cure cycle.

4.5 STRESS ANALYSIS

Since the material is assumed to be linear elastic at a given time, the increment in stress for that time step is given by Hooke's law:

$$\Delta \sigma = E \, \Delta \varepsilon \tag{4.4}$$

Where E is the instantaneous modulus and the total stress is given by

$$\sigma_{i+1} = \sigma_i + \Delta \sigma \tag{4.5}$$

However, in ABAQUS, if we use the UFIELD option to calculate the instantaneous material properties, the stress values are also instantaneous (Equation 4.4). Thus the accumulating part (Equation 4.5) should be done separately. Although the cumulative stresses can be calculated using the UMAT subroutine in ABAQUS, for simplicity a spreadsheet is used for this calculation. The stresses due to CTE mismatch and cure shrinkage are calculated separately and added together at each time step to find the total stress at any instant during the curing process.

4.5.1 THERMAL STRESSES

Equation 4.6 gives the instantaneous thermal stress at any given time.

$$\sigma_{i+1} = E \ CTE \ (T_{i+1} - T_0) \tag{4.6}$$

Where E is the instantaneous Young's modulus, T_0 is initial temperature and T_{i+1} is the current temperature. The above stress is due to the temperature change of $(T_{i+1} - T_0)$. But for the current time step, the required stress should be due to a temperature change of $(T_{i+1} - T_i)$. So the incremental stress due to thermal mismatch can be calculated by scaling the instantaneous stress by the temperature increment for the current time step, i.e.

$$\Delta\sigma_T = \sigma_{i+1} \frac{(T_{i+1} - T_i)}{(T_{i+1} - T_0)} \tag{4.7}$$

where T_0 is the initial temperature, σ_{i+1} is the instantaneous stress due to thermal mismatch at temperature T_{i+1} and $(T_{i+1} - T_i)$ is the temperature increment at this time step. The cumulative stress at this time is given by Equation 4.5.

4.5.2 CURE SHRINKAGE STRESSES

The stress due to resin cure shrinkage is calculated by converting the linear resin cure shrinkage strain to an equivalent thermal expansion (shrinkage) coefficient and setting the thermal expansion coefficient of fibre equal to zero. The volumetric cure shrinkage strain is given by Equation 4.5,

$$
\begin{aligned}
V_r^S &= 0.0 & \alpha < \alpha_{C1} \\
V_r^S &= A\alpha_S + \left(V_r^{S\infty} - A\right)\alpha_S^2 & \alpha_{C1} \leq \alpha < \alpha_{C2} \\
V_r^S &= V_r^{S\infty} & \alpha > \alpha_{C2}
\end{aligned}
\tag{4.8}
$$

$$
\alpha_S = \frac{\alpha - \alpha_{C1}}{\alpha_{C2} - \alpha_{C1}}
$$

where

V_r^S Resin volumetric cure shrinkage

$V_r^{S\infty}$ Total volumetric resin shrinkage from $\alpha = 0$ to 1

α_S The 'cure shrinkage' degree of cure

α_{C1} Degree of cure after which the resin shrinkage begins

α_{C2} Degree of cure after which the resin shrinkage stops

A Linear cure shrinkage coefficient

This volumetric strain is converted to a linear strain by

$$
\varepsilon^S = \left(1 + V_r^S\right)^{1/3} - 1
\tag{4.9}
$$

where ε^S is the linear shrinkage strain and V_r^S is the volumetric shrinkage. This is the strain that a lamina undergoes at a given time. The incremental linear cure shrinkage strain for the time step $(i+1)$ will be

$$
\Delta\varepsilon_{i+1}^S = \varepsilon_{i+1}^S - \varepsilon_i^S
\tag{4.10}
$$

where ε_{i+1}^{S} and ε_{i+1}^{S} are the linear cure shrinkage strains at the current time and the previous time respectively. From this value, the incremental cure shrinkage stress and the total cure shrinkage stress are calculated according to Equations 4.4 and 4.5.

Applying the incremental strain directly to the resin will be difficult. Instead, this incremental strain is applied as thermal load by converting the incremental strain to an equivalent thermal expansion coefficient given by

$$CTE_{S} = \frac{\Delta\varepsilon_{i+1}^{S}}{(T_{i+1} - T_{0})} \tag{4.11}$$

where T_{i+1} is the instantaneous temperature and T_{0} is the initial temperature. Hence, the incremental cure shrinkage stress will be given by

$$\Delta\sigma_{S} = E \, CTE_{S} \, (T_{i+1} - T_{0}) \tag{4.12}$$

and the total stress can be calculated according to Equation 4.5.

The axial stress development in the fibre during the curing process due to thermal mismatch and cure shrinkage is given in Figure 4.9. According to this figure, the contribution of thermal mismatch to the total stress is around 85% and the contribution from cure shrinkage around 15%. Although the cure shrinkage strain is very high compared to the thermal strain, most of the cure shrinkage occurs at low resin modulus. Hence, the contribution from cure shrinkage is low compared to the thermal mismatch.

The stress components to be discussed are shown in Figure 4.10. Since the stress values at the fibre-matrix interface are the critical ones, here we consider only those values. The

circumferential locations around the fibre-matrix will be identified by the angle θ which will be considered positive clockwise from the axis 3.

The normal and shear stresses acting on the interface between the fibre and the matrix, σ_r and $\tau_{r\theta}$, have the same value on the matrix side of the interface as on the fibre side due to the equilibrium condition. These stress components are responsible for the failure of the interface. The normal and shear stresses at the interface between the fibre and the matrix for the AS4/8552 material due to thermal mismatch and cure shrinkage are shown in Figure 4.11. The stresses due to cure shrinkage are lower compared to the stresses due to CTE mismatch. The normal stress, σ_r, depends strongly on θ, and it is compressive at all circumferential locations. This strong dependence on θ is due to the interaction between fibres. The compressive stresses are higher at locations where fibres are close to each other i.e. when $\theta = 30$ and $\theta = 90$. Compared to normal stresses, shear stresses are smaller in magnitude. Since the normal stresses are compressive, there is no possibility for crack initiation in the matrix but the shear stresses may cause interface failure.

The circumferential stress components in the fibre and the matrix do not have the same value (Figure 4.12). The tensile circumferential stress in the matrix may contribute to crack formation in the matrix. The crack in this case will be emanating radially from the interface into the matrix. Note that the ultimate tensile strength of the 8552 resin is around 120 MPa (obtained from the HEXCEL Cooperation product data sheet for 8552 Epoxy Matrix).

The longitudinal stress components in the fibre and the matrix are shown in Figure 4.13. The longitudinal stresses in the fibre are compressive while the longitudinal stresses in the matrix are tensile as expected (the CTE of the resin is higher than the CTE of the fibre). The tensile stresses

in the matrix may contribute to matrix cracking. The longitudinal stresses are quite uniform in the fibre and the matrix.

4.6   CONCENTRIC CYLINDRICAL MODEL

The prediction of the micro-level thermal residual stresses using the finite element method is time consuming. Can the residual stresses be predicted by simple calculations? In this section, the thermal residual stresses calculated by both the finite element method (hexagonal array) and the concentric cylinders model proposed by Wagner et al. (1997) are compared. The stresses in the fibre and the matrix by the concentric cylinder model are given in Equation 4.13.

Stresses in the fibre:
$$\sigma_r^f = \sigma_\theta^f = A^f$$
$$\sigma_1^f = C^f$$
(4.13a)

where A^f and C^f are constants.

Stresses in the matrix:
$$\sigma_r^m = A^m + B^m (R_1 / r)^2$$
$$\sigma_\theta^m = A^m - B^m (R_1 / r)^2$$
$$\sigma_1^f = C^m$$
(4.13b)

where A^m, B^m and C^m are constants and R_1 is the radius of the fibre. σ_r, σ_θ, and σ_1 are radial, hoop and axial stresses as shown in Figure 4.10. Due to the axisymmetry assumption, all the stresses are independent of θ. Full detail of the Equation 4.13 is given in Appendix C.

Since most of the thermal residual stresses develop at the cool down part of the processing cycle, in this case only this part of the cure cycle is considered for comparison of the methods. The material properties of the AS4/8552 material are assumed to remain constant during cool down according to the data available (Johnston, 1996). The thermal residual stresses that develop when the composite is cooled down from 180 °C to room temperature (20 °C), predicted by both finite

element analysis and elasticity approach, are shown in Figures 4.14 to 4.16. In these figures, the various stress components at the fibre-matrix interface are plotted as a function of circumferential location around the interface (Figure 4.10).

The above results shows that the axisymmetric assumption is not good enough in predicting the stresses, particularly the normal and shear stresses. This is due to high fibre volume fraction of the material. It is shown by Hyer (1997) that for low fibre volume fractions (up to 40%), the axisymmetric assumption is quite accurate and the accuracy decreases with increasing fibre volume fraction. Even though the axisymmetric condition is not valid for materials with high fibre volume fraction, the elasticity approach provides a quick and reasonably good estimation of the residual stresses compared to the more time consuming finite element analysis.

4.7 TRANSFERRING MACRO-LEVEL STRESSES TO MICRO-LEVEL

High residual stresses coupled with the low ductility of the matrix may lead to the fracture of the fibre-matrix interface. In order to quantify the residual stresses at the fibre-matrix interface, the macro-level stresses should be transferred to the micro-level. These macro-level stresses are applied as mechanical loads on the RVE. The application of a unit mechanical stress (any component) on the RVE produces stresses (all six component) at the interface. The ratio of the applied stress and the resultant interfacial stress is called the multiplication factor or magnification ratio, i.e. corresponding to an applied stress component, there are six magnification factors for the six stress components at the interface. If the actual mechanical stress is known, then the interface stresses can be calculated by multiplying the mechanical stress with the multiplication factor corresponding to each stress component at the interface. Since the properties of the fibre and the matrix vary during the curing process, these magnification factors

are also not constant during the curing process. For AS4/8552 material, only the resin modulus varies during the curing process. So the multiplication factor also changes according to the changes in resin modulus as shown in Figure 4.17. Hence, the transfer of the mechanical stresses should be done at suitable intervals along the cure cycle. These intervals should be selected according to the composite materials used in the processing. For example, for the material AS4/8552 used here, the magnification factor changes only during a short period of time as shown in Figure 4.17. The time step that was used to calculate the degree of cure (2 min) is used during this period for transferring the macro stresses to micro-level.

4.8 PREDICTION OF ENGINEERING PROPERTIES USING MICROMECHANICS

The interactions of the elastic properties of the fibre and the matrix produce the elastic properties of the composite material. Several micromechanical equations have been proposed for the prediction of composite properties from those of the constituent fibre and matrix using variational principles. A survey of the existing micromechanical models was carried out by Hashin (1983).

In COMPRO, the engineering properties are calculated by using the micromechanics equations found in the paper by Bogetti and Gillespie (1992) that was originally proposed by Rosen and Hashin (1964). These equations are based on classical elasticity solution by assuming that the volume of fibres and matrix in a composite can be filled with an assemblage of cylindrical fibres and surrounding matrix material, with the fibres being of various sizes to the degree that the fibre-matrix combinations of cylinders completely filled the volume of the composite. This

notion is called the composite cylinders model. The ratio of the diameter of the fibre to the diameter of the surrounding matrix represents the fibre volume ratio.

In this section, the engineering properties calculated by both the elasticity approach and numerical approaches are compared. Since the resin elastic properties change during the autoclave processing, the results are compared for different values of resin modulus.

First we consider an isotropic case. In this case, both the fibre and the matrix are isotropic. The material properties of fibre and matrix are selected arbitrarily and given in Table 4.1. The effective material properties from different approaches are given in Table 4.2. All these methods quite accurately predicted the longitudinal engineering properties (E_1, v_{12}). Even the simple rule of mixture predicts the same results. But there are discrepancies in the prediction of transverse engineering properties as shown in Figure 4.18. In this figure, the transverse modulus predicted by all three approaches is compared for different matrix modulus. At high matrix modulus, both approaches (Hexagonal and Square) agree well with the elasticity approach. But at lower matrix modulus, the difference between the square and elasticity approaches is much greater (around 30%) compared to the difference between hexagonal and elasticity approaches (around 5%). This can be justified by comparing the unit cells of all these approaches. The unit cells for all three approaches (elasticity, square, hexagonal) are shown in Figure 4.19. The cross-sectional areas of all three unit-cells are equal and the fibre volume fraction is 0.573. All these three unit-cells are superposed on top of each other and are shown in Figure 4.20. By observing this figure, we can see that the unit cell considered in the elasticity approach is somewhat closer to the hexagonal than the square array unit cells.

The predicted composite engineering properties for the AS4/8552 material by hexagonal array and elasticity approach are listed in Table 4.3.

4.9 SUMMARY AND CONCLUSIONS

From the above study, it is clear that apart from the residual stresses due to the thermal mismatch between the fibre and the resin, the cure shrinkage also contributes to residual stress formation. Although the cure shrinkage strains are higher than the thermal strains, for this resin data set, most of the cure shrinkage occurs when the resin modulus is low thus resulting in low residual stresses. For another material the contribution of the cure shrinkage may be greater.

Significant amount of thermal residual stresses develop only during the cooling down part of the curing process. Therefore, the thermal residual stresses can be calculated with reasonable accuracy by only considering the cooling down part of the processing cycle.

The micro-level residual stresses can be predicted using the simple concentric cylinders model even though the accuracy of the model reduces with increasing fibre volume fraction.

4.10 TABLES

Table 4.1: Material properties of isotropic fibre and matrix

Property	Isotropic Fibre	Isotropic Matrix
Young Modulus (GPa)	100	1 - 100
Poisson's Ratio	0.25	0.25

Table 4.2: Material properties of composite for fibre volume fraction of 0.573. Both fibre and matrix are isotropic

Resin Modulus (GPa)	Elasticity Approach				Numerical Approach							
					Square Array				Hexagonal Array			
	E_1 (GPa)	E_2 (GPa)	ν_{12}	ν_{23}	E_1 (GPa)	E_2 (GPa)	ν_{12}	ν_{23}	E_1 (GPa)	E_2 (GPa)	ν_{12}	ν_{23}
1	57.73	3.13	0.250	0.329	57.73	4.01	0.250	0.173	57.73	3.26	0.250	0.301
10	61.57	25.44	0.250	0.299	61.57	29.30	0.250	0.208	61.57	26.03	0.250	0.283
20	65.84	42.42	0.250	0.280	65.84	46.03	0.250	0.226	65.84	42.93	0.250	0.271
30	70.11	54.88	0.250	0.268	70.11	57.62	0.250	0.235	70.11	55.23	0.250	0.264
40	74.38	64.65	0.250	0.261	74.38	66.54	0.250	0.241	74.38	64.86	0.250	0.259
50	78.65	72.67	0.250	0.256	78.65	73.89	0.250	0.245	78.65	72.78	0.250	0.255
60	82.92	79.48	0.250	0.253	82.92	80.21	0.250	0.247	82.92	79.54	0.250	0.253
70	87.19	85.44	0.250	0.252	87.19	85.81	0.250	0.248	87.19	85.46	0.250	0.252
80	91.46	90.75	0.250	0.251	91.46	90.90	0.250	0.249	91.46	90.75	0.250	0.251
90	95.73	95.57	0.250	0.250	95.73	95.60	0.250	0.250	95.73	95.57	0.250	0.250
100	100.00	100.00	0.250	0.250	100.00	100.00	0.250	0.250	100.00	100.00	0.250	0.250

Table 4.3: Material properties for an AS4/8552 lamina. Material properties are calculated at both initial (uncured) and final (cured) resin modulus.

Resin Modulus (GPa)	Elasticity Approach						Hexagonal Array					
	E_1 (GPa)	E_2 (GPa)	ν_{12}	ν_{23}	CTE1 μm/m/C	CTE3 μm/m/C	E_1 (GPa)	E_2 (GPa)	ν_{12}	ν_{23}	CTE1 μm/m/C	CTE3 μm/m/C
4.67E-3	120.3	0.017	0.263	0.525	0.031	28.7	120.3	0.018	0.263	0.479	0.031	25.9
4.67	122.4	9.900	0.268	0.471	0.714	28.5	122.4	9.862	0.269	0.431	0.811	27.3

4.11 FIGURES
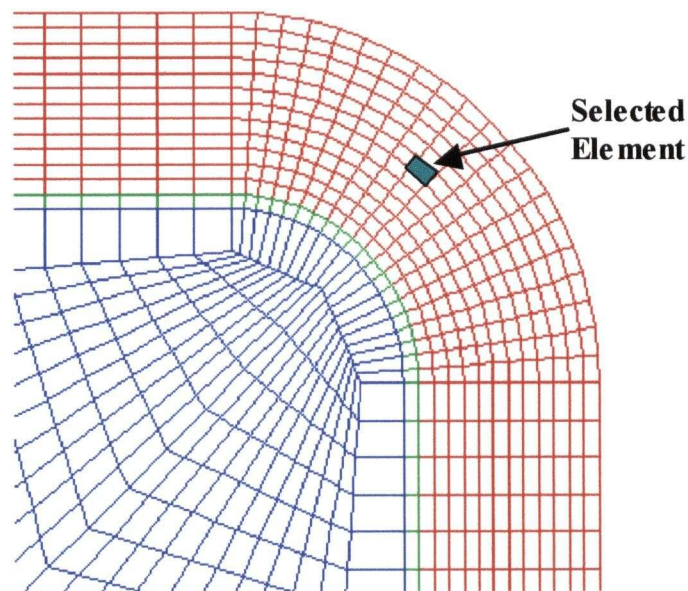
Figure 4.1: The element selected for micro stress analysis in an L-shaped part.
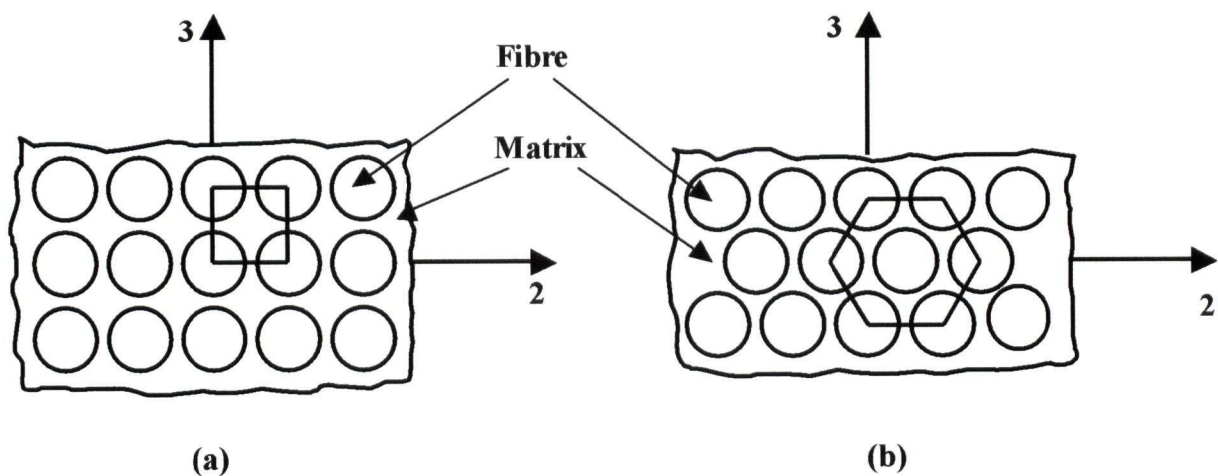
Figure 4.2: The cross section of a unidirectional ply with commonly used periodic fibre arrangements: (a) square array (b) hexagonal array.
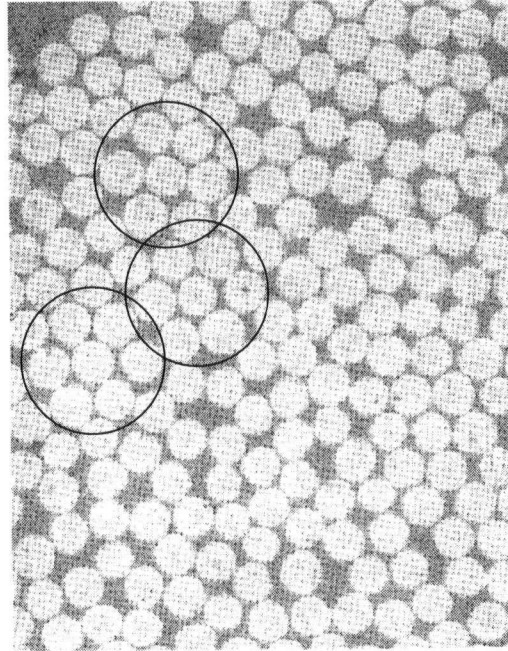
Figure 4.3: Cross section of graphite-reinforced composite material (Hyer, 1997).

(a)

(b)
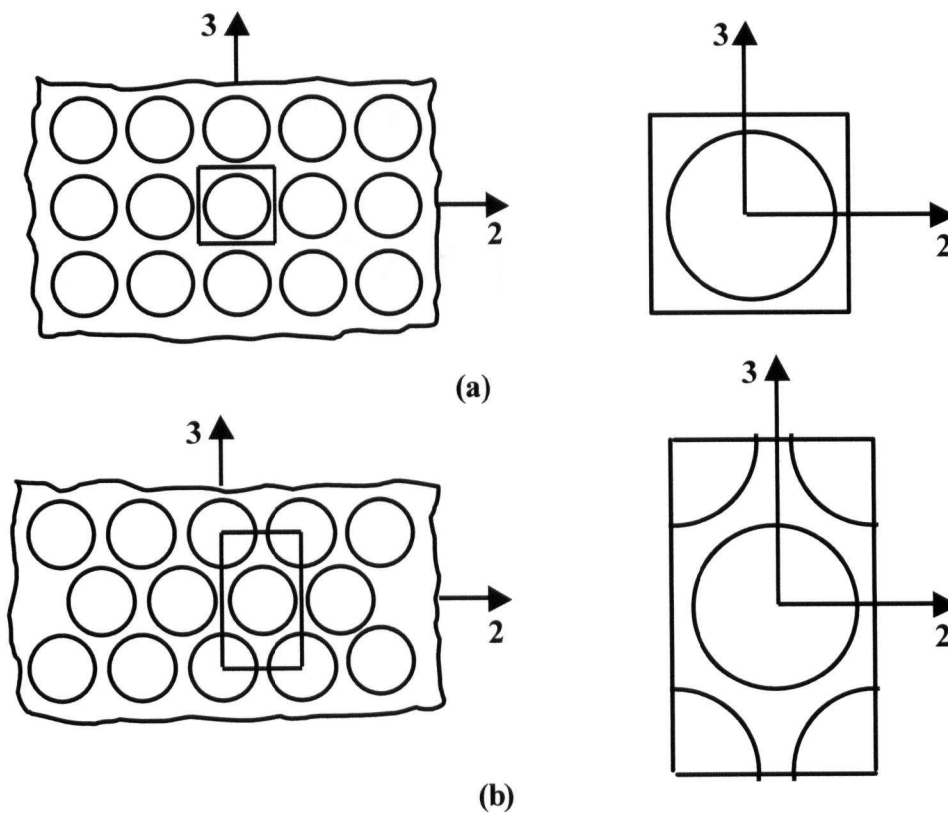
Figure 4.4: The representative volume element (RVE) concept for (a) *square array* **(b)** *hexagonal array.*
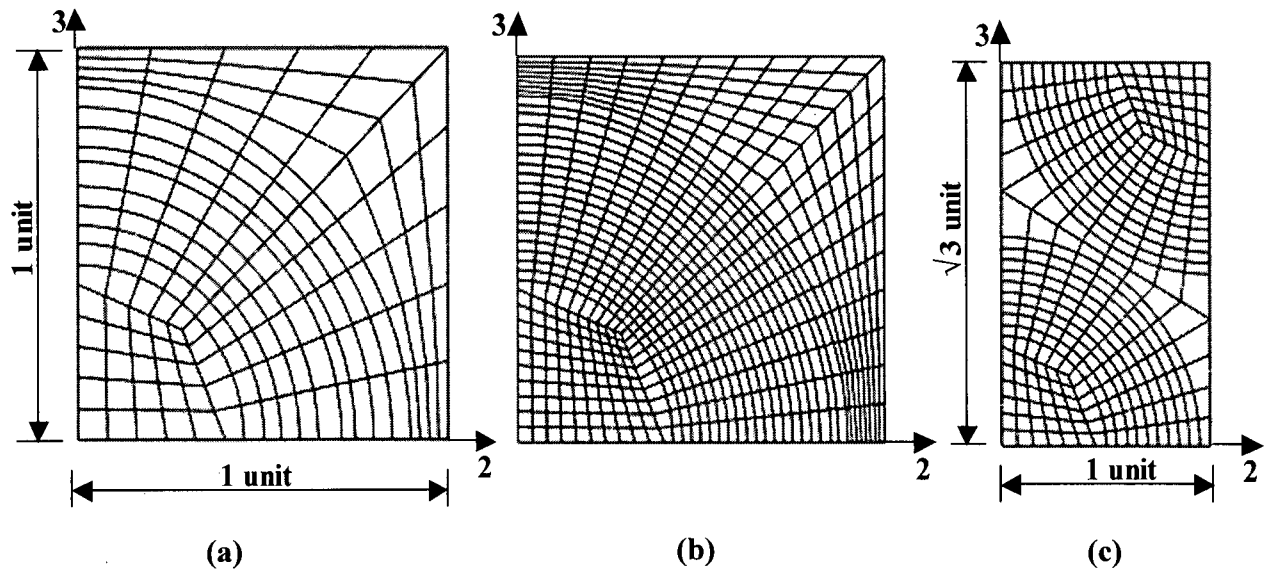
Figure 4.5: Finite element mesh used for the micro stress analysis: (a) square array   (b) square array (fine mesh) (c) hexagonal array.
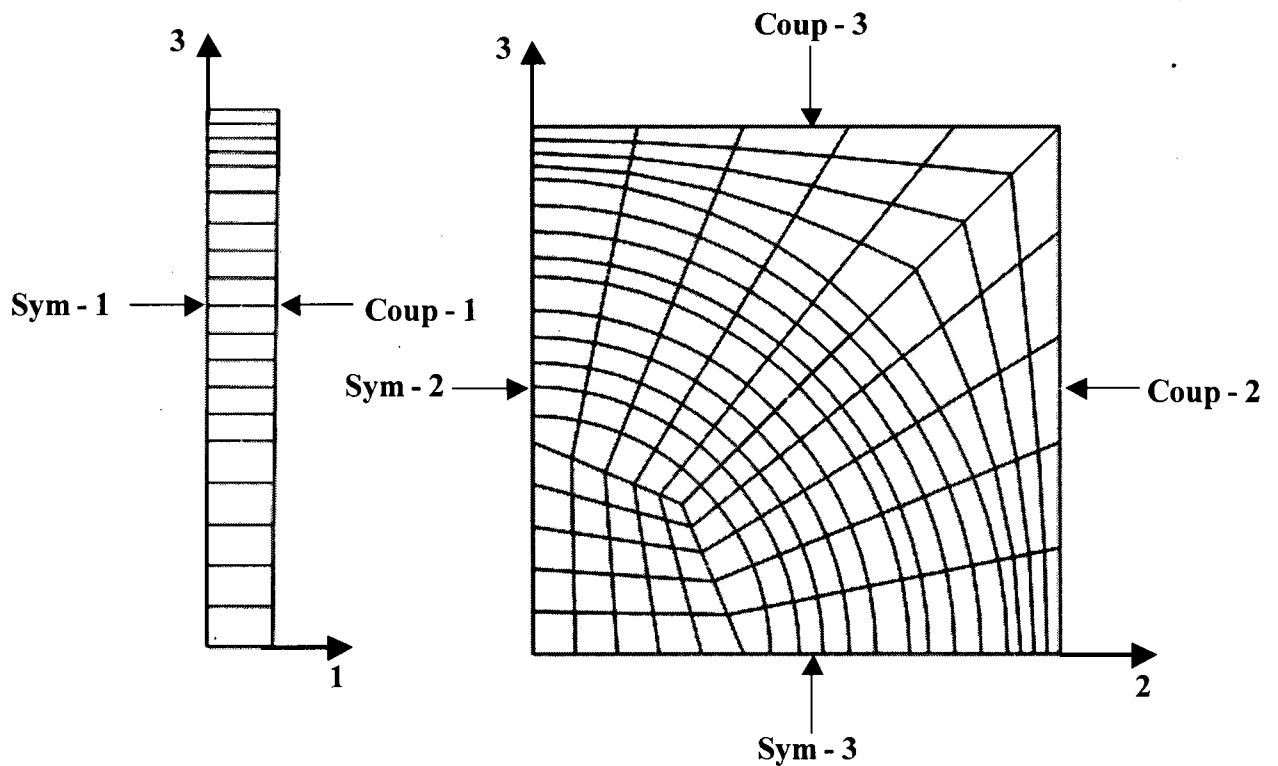
Figure 4.6: The applied boundary condition for the RVE. Due to the symmetry only a quarter of the RVE is considered. "Sym" stands for symmetric boundary and "Coup" stands for the couple boundary.
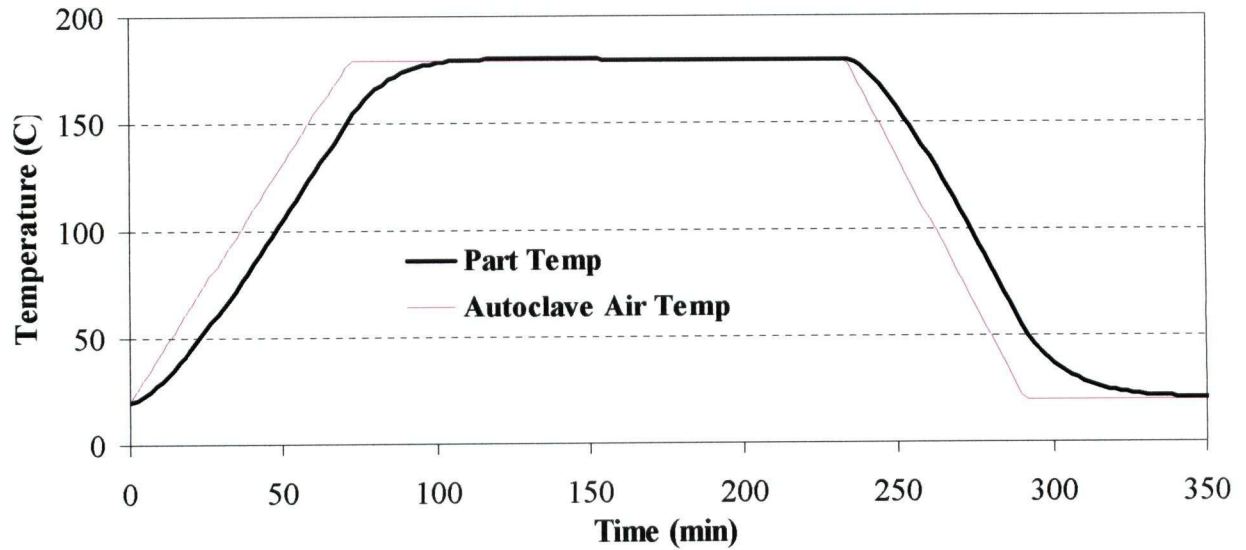
Figure 4.7: The temperature-time history of the element shown in Figure 4.1 as obtained from COMPRO.
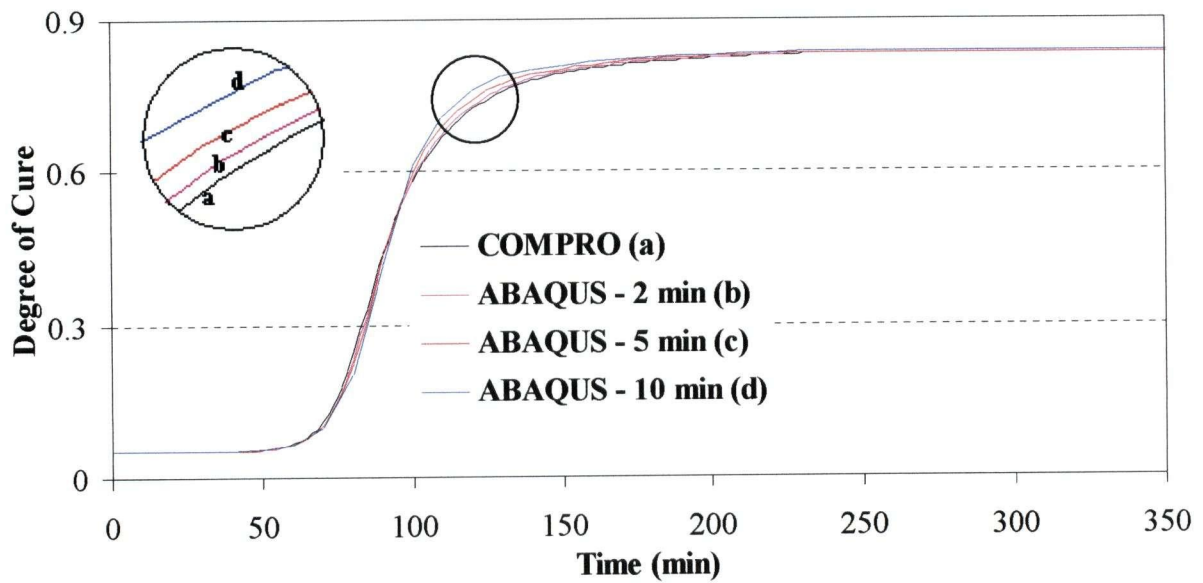
Figure 4.8: The development of degree of cure of resin as it cures during the autoclave processing of the L-shaped composite part: the ABAQUS results for three different time steps (10 min, 5 min and 2 min) are compared with COMPRO results. The circled portion of the graph is magnified and shown.
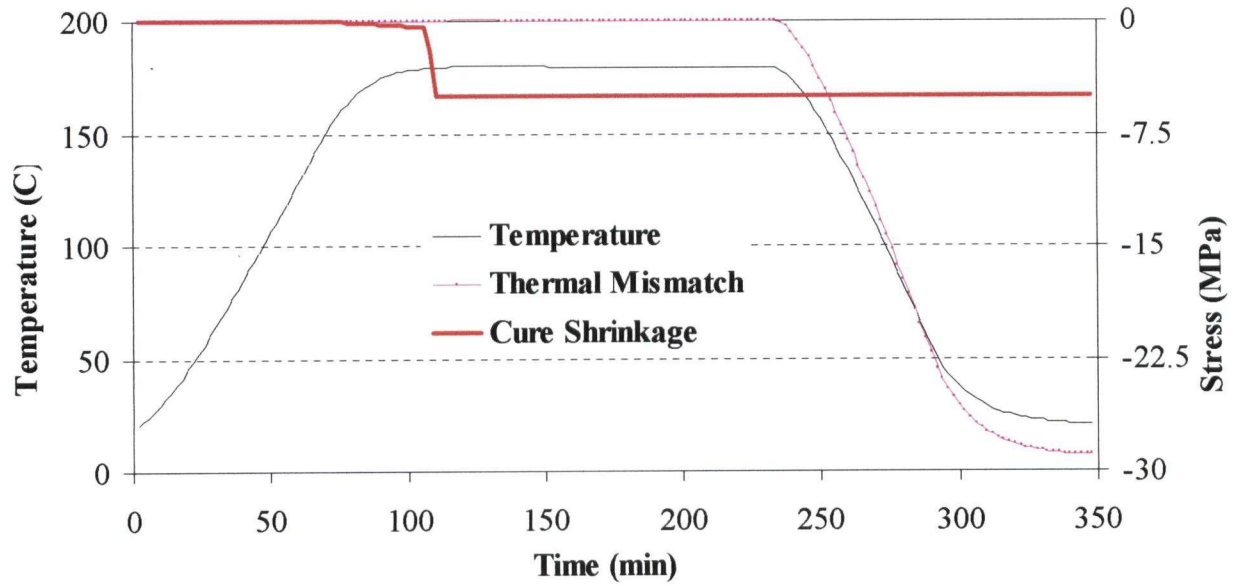
Figure 4.9: The development of stresses due to CTE mismatch between the fibre and the matrix and cure shrinkage of resin as the resin cures during processing of an L-shaped composite part.
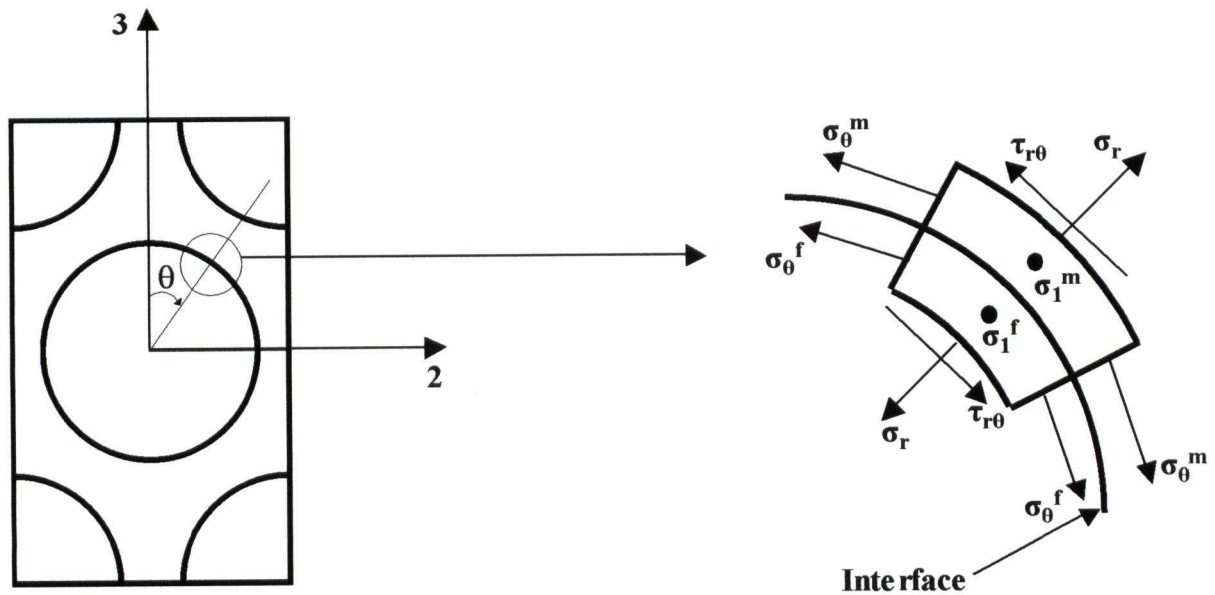
Figure 4.10: The axial (1), normal (r), and the circumferential (θ) stress components at the fibre matrix interface. The maximum stress occurs at the interface.
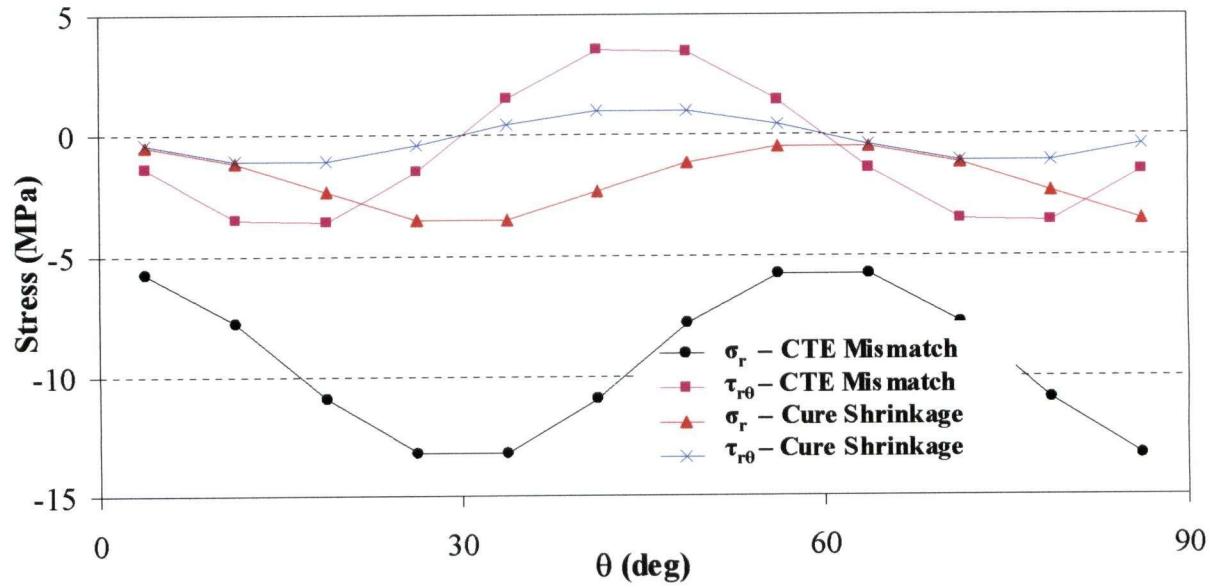
Figure 4.11: The distribution of normal (σ_r) and shear ($\tau_{r\theta}$) stress components along the fibre-matrix interface due to the CTE mismatch and resin cure shrinkage.
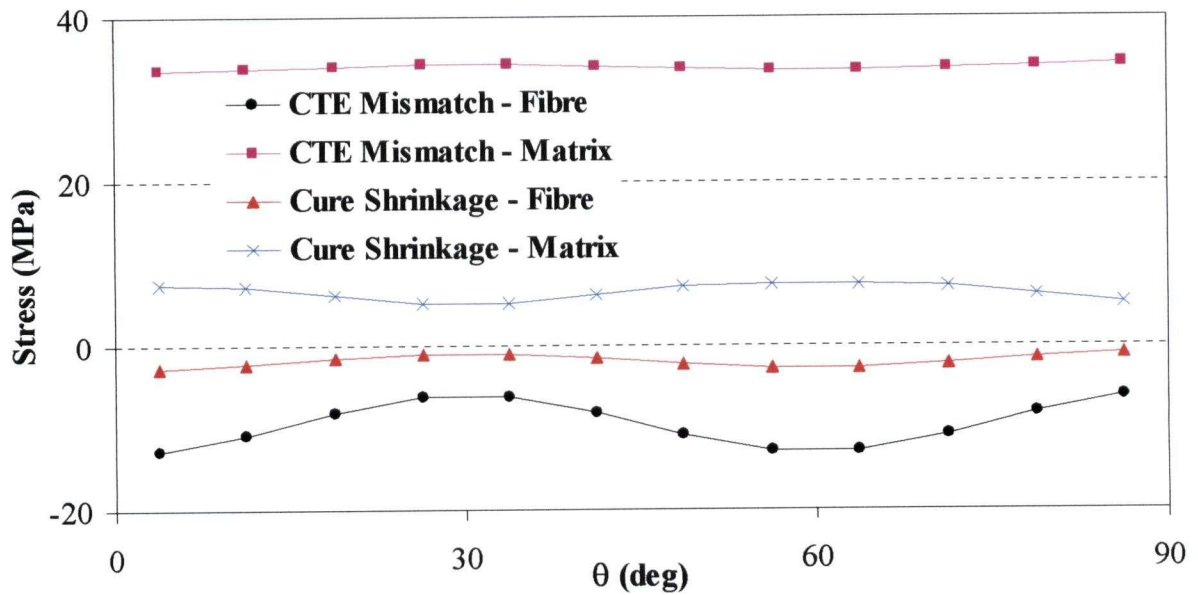
Figure 4.12: The distribution of circumferential (σ_θ) stress components along the fibre-matrix interface due to the CTE mismatch and resin cure shrinkage.
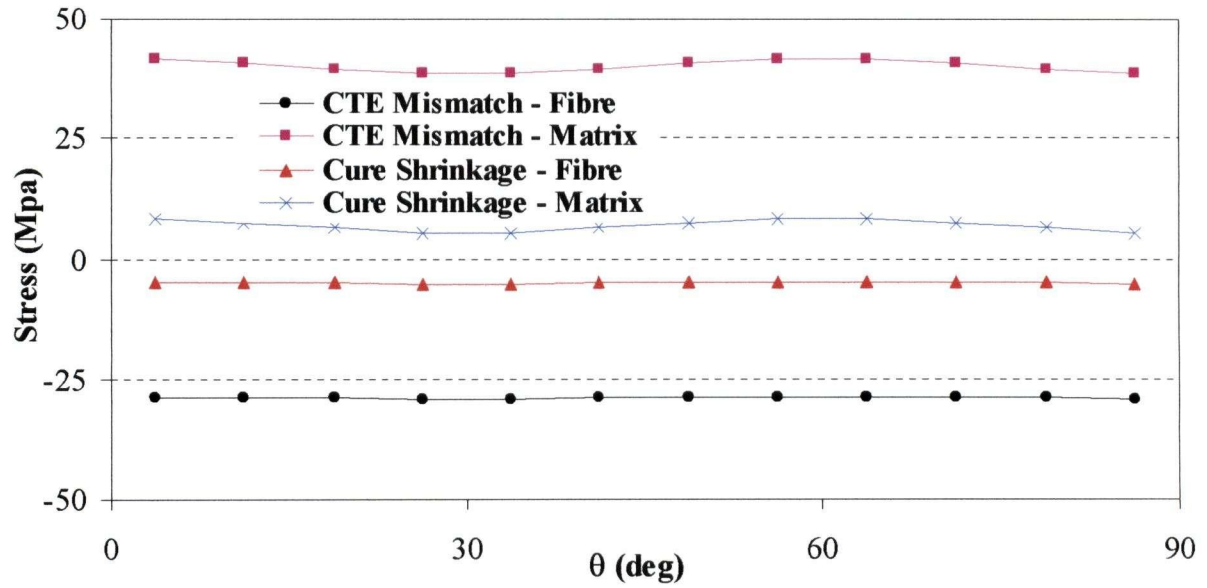
Figure 4.13: The distribution of the axial stress components, σ_1, along the fibre-matrix interface due to the CTE mismatch and resin cure shrinkage.
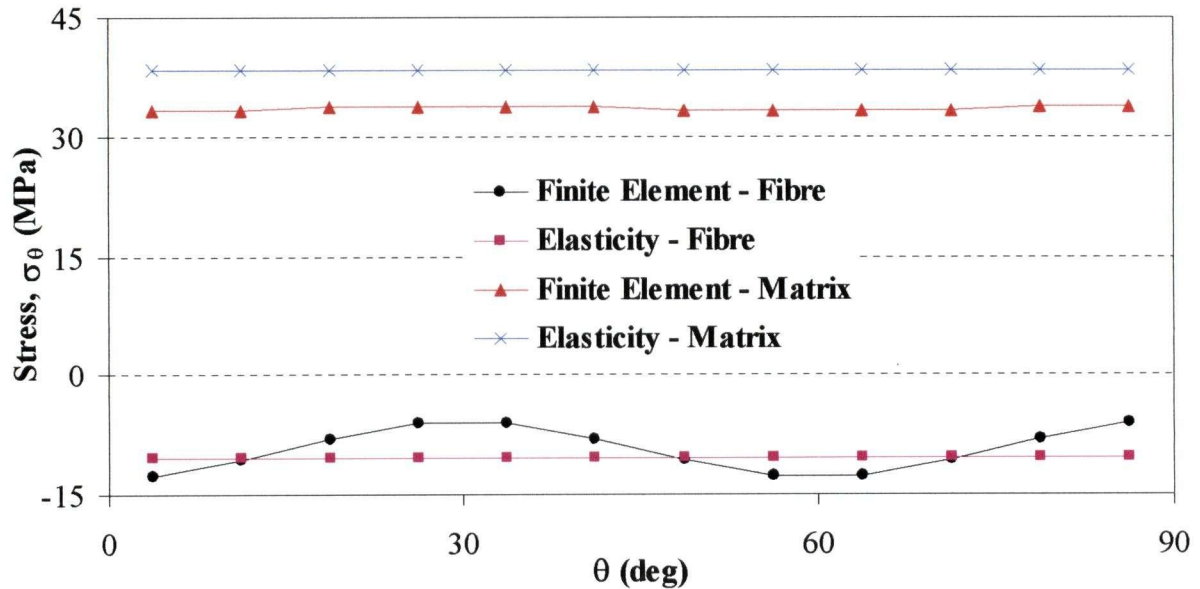
Figure 4.14: Comparison of circumferential stresses between concentric cylinders model (elasticity approach) and finite element solution for a temperature change of -160 °C.
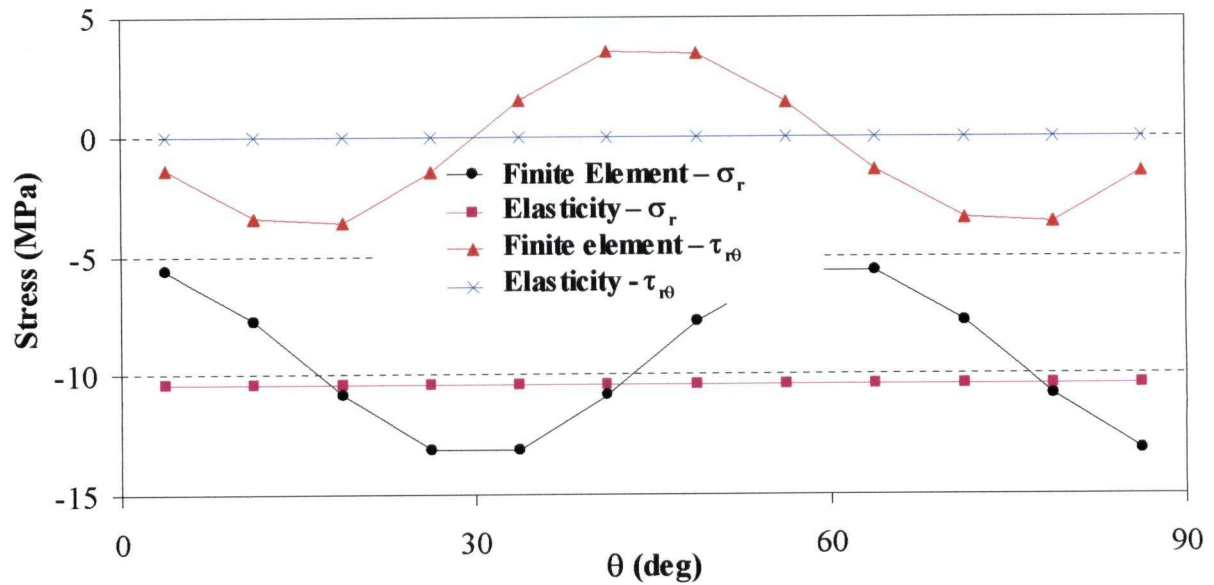
Figure 4.15: **Comparison of normal and shear stresses between concentric cylinders model (elasticity approach) and finite element solution for a temperature change of -160 °C.**
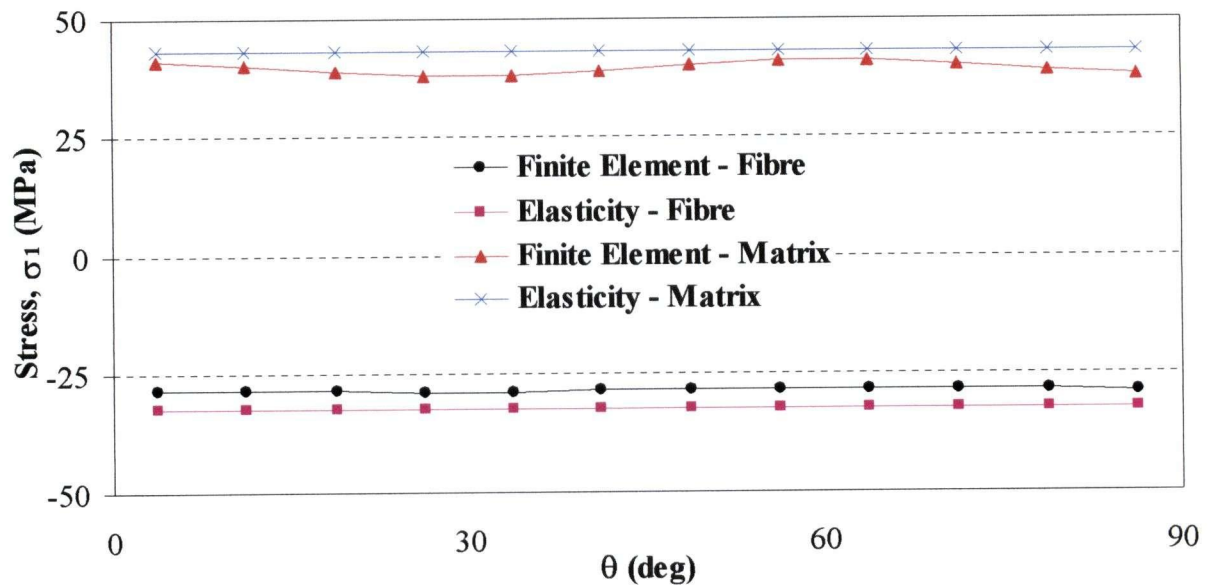
Figure 4.16: **Comparison of axial stresses between concentric cylinders model (elasticity approach) and finite element solution for a temperature change of -160 °C.**
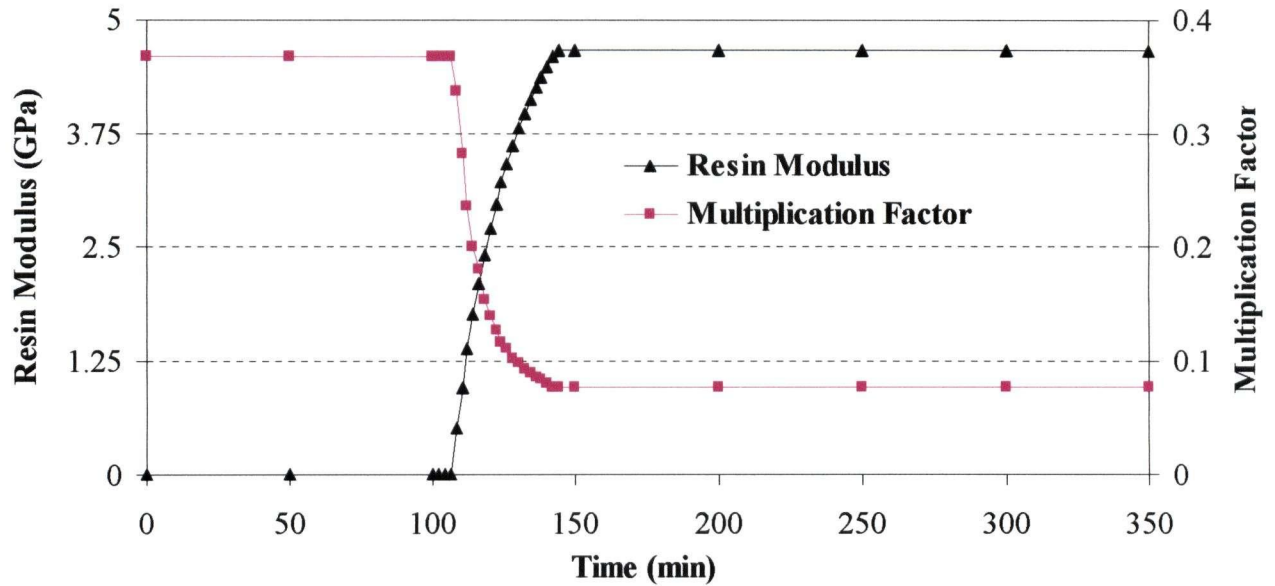
Figure 4.17: The variation of the stress multiplication factor for axial stress at the interface during the cure cycle. The multiplication factor is for the fibre at $\theta = 0$ (Figure 4.10) for an applied axial mechanical stress.
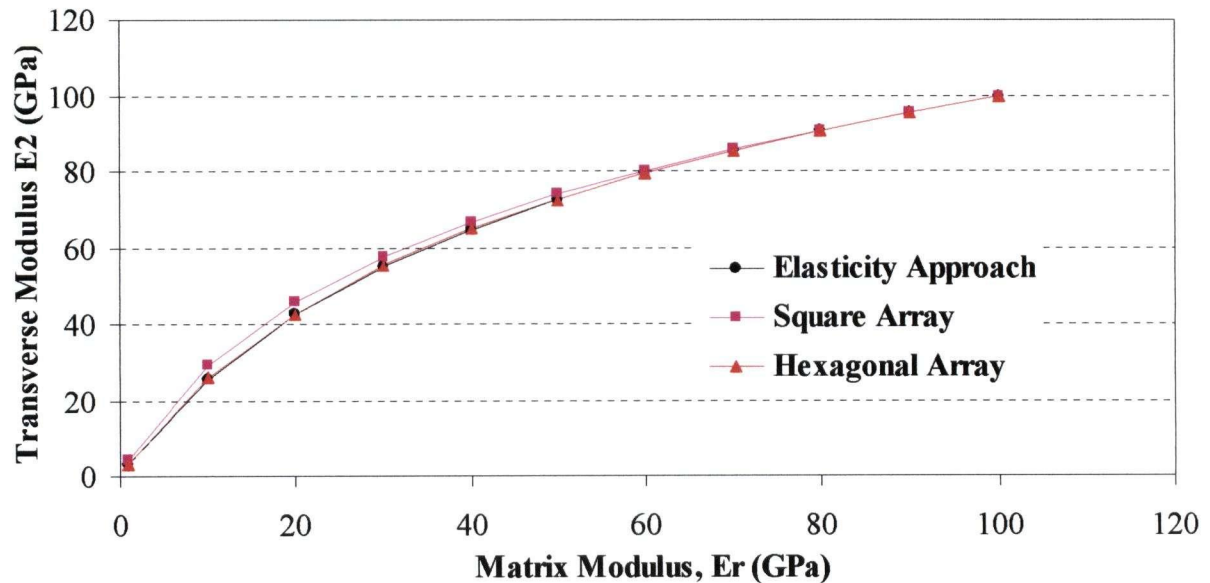
Figure 4.18: Comparison of transverse modulus, E_2 by three different approaches for different matrix modulus. Both fibre and matrix are isotropic.
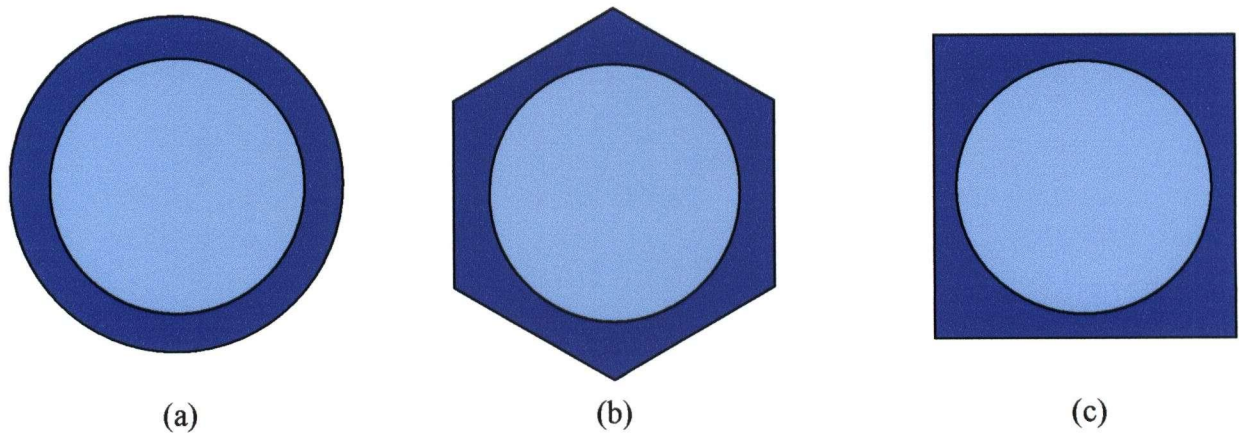
Figure 4.19: Unit cells considered in: (a) elasticity approach (b) hexagonal array and (c) square array.
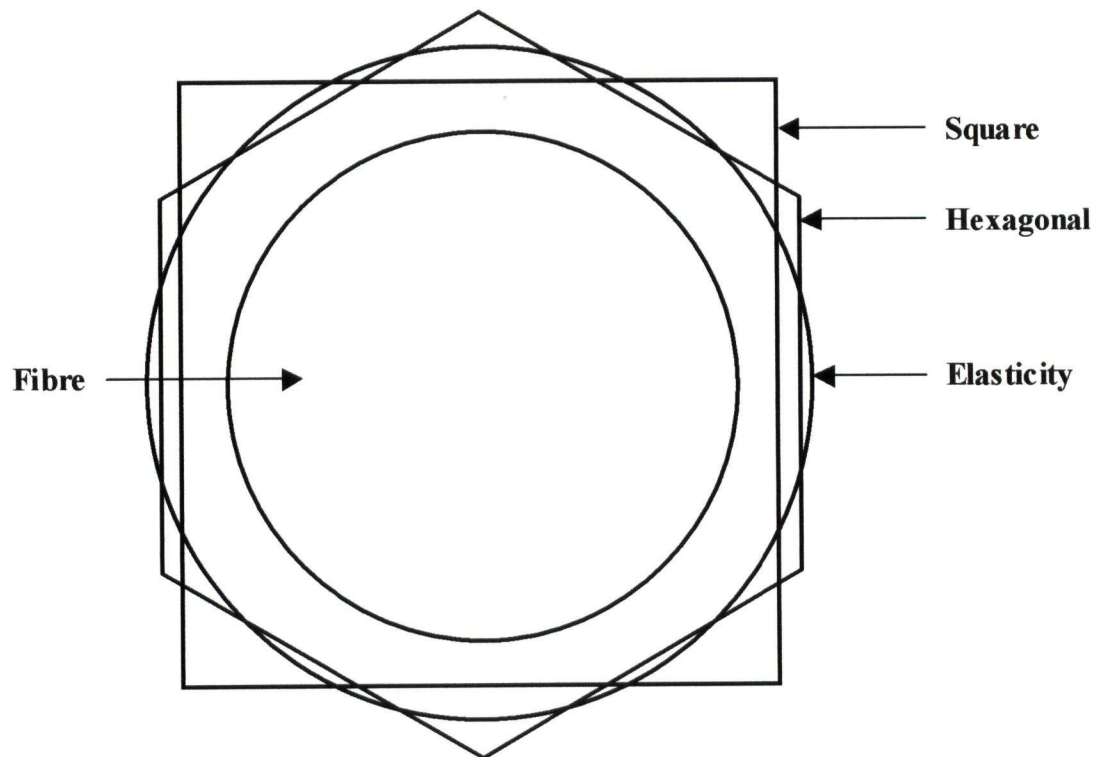
Figure 4.20: All unit cells superposed on top of each other to reveal the difference between different approaches.

CHAPTER 5:   CONCLUSIONS AND FUTURE WORK

The objective of this thesis was to investigate the processing effect on the performance of composite structures. Since the experimental investigation is costly and time consuming, in this work, investigation was done using a combination of available software. The major accomplishments of the current work include:

- **A probabilistic design tool was proposed to determine the variability in the processing parameters to achieve the target performance reliabilities.**

A computational framework using commercially available and in-house developed numerical software was proposed for analysing the complete sequence of events from the *manufacturing* stage to the *in-service* structural performance of a composite structure.

The in-house developed processing software, COMPRO, was used to predict the process-induced deformation and stresses on 2D cross section of the composite structure. An approximate superposition method was used to develop the 3D effects based on the 2D plane strain results obtained from COMPRO. The commercial finite element software, ABAQUS, was used to analyse deterministically the process effect on the structural behaviour. A parametric study was carried out to determine the most influential process parameters and the inverse reliability analysis software, IRELAN, was used to determine the process parameters that must be controlled to meet structural performance standards with target reliabilities.

- **The parameters and mechanisms that affect the spring-in of angled thermoset composite parts during processing were investigated.**

In the design example presented earlier, only a limited number of process parameters that affect the structural performance of a simple composite structure, flat plate, was considered for simplicity. In this case, the intrinsic and extrinsic parameters that affect the dimensional stability of a more complex composite structure, angle laminate, were investigated using COMPRO. The prediction capability of COMPRO was examined by comparing the predicted results with available experimental results. Although, using a shear layer to model the tool-part interaction is not a physically reasonable method, it was shown that the shear layer could be used to predict most of the trends observed in the experimental study. A crude method of introducing a gap in the corner was proposed to overcome the corner-locking problem in the C-shaped parts.

- **The residual stresses developed during processing at micro-level were investigated.**

The process-induced residual stresses may lead to the premature failure of a composite structure. To apply any failure criteria available in the literature, the stresses at the material point should be known. Apart from the stresses that develop at the laminate level, the mismatch between the fibre and the matrix also produces additional stresses. Stresses due to the CTE mismatch and cure shrinkage were calculated. It is shown that for this particular resin material, the stresses due to cure shrinkage were not significant compared to the stresses due to CTE mismatch. A simple concentric cylinder model available in the literature was suggested to determine the stresses due to CTE mismatch with reasonable accuracy. A magnification factor method was proposed to transfer the laminate level stresses to micro-level during the curing process.

5.1 FUTURE WORK

The proposed design tool is only an initial attempt to incorporate the processing effect explicitly into the design as a more scientific method to replace knockdown factors that attempt to do this

in an empirical fashion. Knockdown factors are typically established through an extensive experimental study that often may not be totally relevant to the current design problem.

The following are some points to be considered in the future work:

- The difficulty found during the course of this study was to find a realistic design problem where the processing effects were actually observed. To develop the confidence level in the proposed design approach, a realistic design problem should be analysed and compared by both the proposed probabilistic design approach and the traditional knockdown factor approach.

- The spatial variation of the variabilities in the material and dimensional parameters should be incorporated through a more sophisticated stochastic finite element approach.

- The variability of all possible parameters from the raw material level to structural level should be taken into account. For this, a robust inverse reliability system should be established to handle the huge amount of random variables.

REFERENCES

ABAQUS, (5.8), Hibbitt, Karlsson & Sorensen, Inc., 1998.

Albert, C.I., "Spring-In of Angled Thermoset Composite Laminates", M.A.Sc. Thesis, The University of British Columbia, 2001.

Arbocz, J. and Hol, M.A.M., "Collapse of Axially Compressed Cylindrical Shells with Random Imperfections", AIAA Journal, Vol. 29, No. 12, 1991, pp. 2247-2256.

Bogetti, T.A. and Gillespie, J.W., Jr., "Process-Induced Stress and Deformation in Thick-Section Thermoset Composite Laminates", Journal of Composite Materials, Vol. 26, No. 5, 1992, pp. 626-659.

Bowles, D.E. and Griffin, O.H., Jr., "Micromechanics Analysis of Space Simulated Thermal Stresses in Composites. Part I: Theory and Unidirectional Laminates", Journal of Reinforced Plastics and Composites, Vol. 10, 1991, pp. 504-521.

Cederbaum, G. and Arbocz, J., "On the Reliability of Imperfection-Sensitive Long Isotropic Cylindrical Shells", Structural Safety, Vol. 18, No. 1, 1996, pp. 1-9.

Chen, P.C. and Ramkumar, R.L., "RAMPC – An Integrated Three-Dimensional Design Tool for Processing Composites", 33rd International SAMPE Symposium, March 7-10, 1988, pp. 1697-1708.

Chen, Y., Xia, Z. and Ellyin, F., "Evaluation of Residual Stresses Induced during Curing Processing Using a Viscoelastic Micromechanical Model", Journal of Composite Materials, Vol. 35, No. 6, 2001, pp. 522-542.

Chryssanthopoulos, M.K., Giavotto, V. and Poggi, C., "Characterization of Manufacturing Effects for Buckling-Sensitive Composite Cylinders", Composites Manufacturing, Vol. 6, No. 2, 1995, pp. 93-101.

Elseifi, M.A. and Gürdal, Z., Nikolaidis, E., "Convex/Probabilistic Models of Uncertainties in Geometric Imperfections of Stiffened Composite Panels", AIAA Journal, Vol. 37, No. 4, April, 1999, pp. 468-474.

Fernlund, G., Rahman, N., Courdji, R., et al., "Experimental and Numerical Study of the Effect of Cure Cycle, Tool Surface, Geometry and Lay-up on the Dimensional Fidelity of Autoclave-Processed Composite Parts", Submitted to Composites Part A: Manufacturing.

Foschi, R.O., Folz, B., Yao, F., Li, H. and Baldwin, J., "RELAN: Reliability Analysis Software", Department of Civil Engineering, The University of British Columbia, 1999a.

Foschi, R.O. and Li, H., "IRELAN: Inverse Reliability Analysis Software", Department of Civil Engineering, The University of British Columbia, 1999b.

Foschi, R.O. and Li, H., "Reliability and Performance-Based Design in Earthquake Engineering", Proceedings, Int. Conf. for Structural Safety and Reliability, ICOSSAR, Newport Beach, CA, 2000.

Hashin, Z., "Analysis of Properties of Fibre Composites with Anisotropic Constituents", ASME Journal of Applied Mechanics, Vol. 46, 1979, pp. 543-550.

Hashin, Z., "Analysis of Composites Materials – A Survey", ASME Journal of Applied Mechanics, Vol. 50, 1983, pp. 481-505.

Hayer, M.W., "Stress Analysis of Fiber – Reinforced Composite Materials", WCB/McGraw – Hill, 1997.

Hexcel Corporation Product Data Sheet, "8552 Epoxy Matrix", Hexcel Corporation, Retrieved 16 February 2002 <http://www.hexcelcomposites.com/downloads/techdata/PRE8552D.PDF>.

Hubert, P. "Aspects of Flow and Compaction of Laminated Composite Shapes During Cure", Ph.D. Thesis, University of British Columbia, 1996.

Hubert, P., and Poursartip, A., "Study of the Interaction Between Percolation and Shear Flow in Processing of Thermoset Matrix Composites", American Society for Composites, College Station, Texas, September 2000.

Johnston, A., "An Integrated Model of the Development of Process Induced Deformation in Autoclave Processing of Composite Structures", Ph.D. Thesis, The University of British Columbia, 1997.

Johnston, A., Vaziri, R., and Poursartip, A., "A Plane Strain Model for Process-Induced Deformation of Laminated Composite Structures", Journal of Composite Materials, Vol. 35, No.16, 2001, pp. 1435-1469.

Kaw, A. K., "Promal", (1.0), CRC Inc., Boca Raton, FL, 1997.

Li, H., "An Inverse Reliability Method and its Applications in Engineering Design", Ph.D. Thesis, The University of British Columbia, 1999.

Li, Y.W., Elishakoff, I. and Starnes, J.H., "Axial Buckling of Composite Cylindrical Shells with Periodic Thickness Variation", Computers and Structures, Vol.56, No.1, 1995, pp. 65-74.

Long, M.W. and Narciso, J.D., "Probabilistic Design Methodology for Composite Aircraft Structures", Final Report, U.S. Department of Transportation, Federal Aviation Administration, June 1999.

Loos AC, Springer GS., "Curing of Epoxy Matrix Composites", Journal of Composites Materials, Vol.17, No. 2, 1983, pp.58-75.

Nelson RH and Cairns DS., "Prediction of dimensional changes in composite laminates during cure", International SAMPE Symposium and Exhibition Covina, Ca, Book 2, 1989, pp.2397-2410.

Osooly-Talesh, A., "Implementation of an 8-noded 2D element in COMPRO", Internal Report, Composite Group, The university of British Columbia, November 2001.

Radford DW and Diefendorf RJ., "Shape instabilities in composites resulting from laminate anisotropy", Journal of Reinforced Plastics and Composites, Vol.12, 1993, pp.58-75.

Radford, D.W. and Rennick, T., "Separating Sources of Manufacturing Distortion in Laminated Composites", Journal of Reinforced Plastics and Composites, Vol. 19, No. 8, 2000, pp. 621-641.

Rosen, B.W. and Hashin, Z., "Elastic Moduli of Fibre-Reinforced Materials", ASME Journal of Applied Mechanics, Vol. 31, 1964, pp. 223-232.

Rosen, B.W. and Hashin, Z., "Effective Thermal Expansion Coefficients and Specific Heats of Composite Materials", International Journal of Engineering Science, Vol. 8, 1970, pp. 157-173.

Schapery, R.A., "Thermal Expansion Coefficients of Composite Materials Based on Energy Principles", Journal of Composite Materials, Vol. 2, 1968, pp. 380-404.

Shiao M. C. and Chamis C.C., "Probabilistic Evaluation of Fuselage-Type Composite Structures", Probabilistic Engineering Mechanics, Vol. 14, 1999, pp. 179-187.

Starnes, J.H., Jr., Hilburger, M.W., and Nemeth, M.P., "The Effects of Initial Imperfections on the Buckling of Composite Shells", Paper presented at the ASTM Symposium on Composite Structures: Theory and Practice, Seattle, WA, May 17 – 18, 1999.

Twigg, GA., "Tool-part interaction in composites processing", M.A.Sc. Thesis, The University of British Columbia, 2001.

Wagner, H.D. and Nairn, J.A., "Residual Thermal stresses in Three Concentric Transversely Isotropic Cylinders: Application to Thermoplastic – Matrix Composites Containing a Transcrystalline Interphase", Composites Science and Technology, Vol. 57, 1997, pp. 1289-1301.

Zhu, T.L., "A Reliability-Based Safety Factor for Aircraft Composite Structures", Computers & Structures, Vol. 48, No. 4, 1993, pp. 745-748.

APPENDIX A: MATERIAL PROPERTIES OF HERCULES AS4/8552 UNIDIRECTIONAL PREPREG

These data are for a fibre volume fraction of 0.573 and are obtained from Johnston (1997).

A.1 FIBRE ELASTIC PROPERTIES

The fibre is a transversely isotropic material and the isotropic axes are the 2-3 axes. These properties are independent of temperature.

Description	Units	Value
Longitudinal Modulus, E1	GPa	210
Transverse Modulus, E2	GPa	17.24
Major Poisson Ratio, v12		0.2
Minor Poisson Ratio, v23		0.25
Longitudinal Shear Modulus, G13	GPa	27.6

A.2 RESIN CURE KINETICS MODEL

$$\frac{d\alpha}{dt} = \frac{K\alpha^m(1-\alpha)^n}{1+e^{C\{\alpha-(\alpha_{C0}+\alpha_{CT}T)\}}} \tag{A.1}$$

$$K_i = A_i e^{-\Delta E_i/RT} \tag{A.2}$$

Variable	Description	Units	Values
α	Resin degree of cure.	-	
T	Resin temperature	K	
H_R	Total resin heat of reaction (α = 0 to 1)	J/kg	5.40E5
A_i	Pre-exponential factor.	/s	1.528E5
ΔE_i	Activation energy.	J/mol	6.65E4
m	Equation superscript.	-	0.8129
n	Equation superscript.	-	2.736

R	Gas constant	J/(mol K)	8.3143
C	Diffusion constant	-	43.09
α_{C0}	Diffusion constant	-	-1.684
α_{CT}	Diffusion constant	/K	5.475E-3

A.3 RESIN CURE SHRINKAGE MODEL

$$V_r^S = 0.0 \quad \alpha < \alpha_{C1}$$

$$V_r^S = A\alpha_S + \left(V_r^{S\infty} - A\right)\alpha_S^2 \quad \alpha_{C1} \leq \alpha < \alpha_{C2}$$

$$V_r^S = V_r^{S\infty} \quad \alpha \geq \alpha_{C2}$$

$$\alpha_S = \frac{\alpha - \alpha_{C1}}{\alpha_{C2} - \alpha_{C1}}$$

(A.3)

Variable	Description	Units	Values
V_r^S	Resin volumetric cure shrinkage	-	
$V_r^{S\infty}$	Total volumetric resin shrinkage from α = 0 to 1.	-	0.099
α_S	The 'cure shrinkage' degree of cure.	-	
α_{C1}	Degree of cure after which the resin shrinkage begins.	-	0.055
α_{C2}	Degree of cure after which the resin shrinkage stops.	-	0.670
A	Linear cure shrinkage coefficient	-	0.173

A.4 RESIN MODULUS DEVELOPMENT MODEL

$$E_r^{'} = E_r^0 \quad T^* < T_{C1}^*$$

$$E_r^{'} = E_r^0 + \frac{T^* - T_{C1}^*}{(T_{C2}^* - T_{C1}^*)}\left(E_r^\infty - E_r^0\right) \quad T_{C1}^* < T^* < T_{C2}^*$$

$$E_r^{'} = E_r^\infty \quad T^* > T_{C2}^*$$

$$E_r = E_r^{'}\left[1 + a_{Er}(T - T_0)\right]$$

(A.4)

$$where : T^* = (T_{ga} + T_{gb} * \alpha) - T; T_{C1}^* = T_{C1a}^* + T_{C1b}^* * T$$

Variable	Description	Units	Values
α	The resin degree of cure.	-	
E_r^{0}	The resin elastic modulus at very low degrees of cure.	Pa	4.67E6
E_r^{∞}	The resin elastic modulus at T_0 and $\alpha = 1.0$	Pa	4.67E9
T	Resin temperature.	°C	
T^{*}	Difference between resin temperature and resin instantaneous T_g	°C	
T_{ga}	Glass transition temperature at $\alpha = 0$	K	2.68E2
T_{gb}	Factor expressing the degree of cure dependence of resin glass transition temperature.	K	2.20E2
T_{C1a}	T^{*} above which resin modulus begins to increase at $T = 0$ K.	K	-45.7
T_{C1b}	Factor expressing the temperature dependence of the T^{*} above which resin modulus begins to increase.	-	0.00
T_{C2}	T^{*} above which resin modulus has reached its full value.	K	-12
T_0	Resin modulus development reference temperature.	°C	20
a_{Er}	Factor expressing the temperature dependence of resin modulus.	Pa/°C	0.00

A.5 RESIN POISSON'S RATIO DEVELOPMENT MODEL

$$v_r = \frac{1}{2}\left[1 - \frac{E_r\left(1 - 2v^{\infty}\right)}{E_r^{\infty}}\right]$$
(A.5)

Variable	Description	Units	Values
v_r	Resin Poisson's ratio	-	
E_r	Resin elastic modulus.	Pa	
E^{∞}	Resin elastic modulus at $\alpha = 1.0$.	Pa	4.67E9
v^{∞}	Resin Poisson's ratio at $\alpha = 1.0$.		0.37

A.6 THERMAL EXPANSION COEFFICIENT

Lumped Ply Coefficients

$CTE_1 = 0.60 \ \mu/°C$

$CTE_2 = CTE_3 = 28.6 \ \mu/°C$

APPENDIX B: PLY MICROMECHANICAL EQUATIONS

The following equations are extracted from Johnston (1997). However, the original sources of these equations are the papers by Bogetti and Gillespie (1992) and Rosen and Hashin (1964).

B.1 CALCULATION OF ELASTIC CONSTANTS

Given as inputs the transversely isotropic mechanical properties of the fibres (E_{11f}, E_{33f}, G_{13f}, v_{13f}, and v_{23f}), the properties of the isotropic resin (E_r, v_r) and the fibre volume fraction, V_f, ply mechanical properties are calculated as follows:

B.1.1 IN-PLANE MODULI

The longitudinal modulus is given by[1]

$$E_{11} = E_{11f}V_f + E_r(1-V_f) + \left[\frac{4(v_r - v_{13f})^2 k_f k_r G_r (1-V_f)V_f}{(k_f + G_r)k_R + (k_f - k_r)G_r V_f} \right] \tag{B.1}$$

where
$$G_r = \frac{E_r}{2(1+v_r)} \tag{B.2}$$

and the transverse modulus is given by

$$E_{22} = E_{33} = \frac{1}{(1/4k_T) + (1/4G_{23}) + (v_{12}^2 / E_{11})} \tag{B.2}$$

---

[1] There is a typographical error in the equation shown in the paper by Bogettie and Gillespie (1992):

$$E_{11} = E_{11f}V_f + E_r(1-V_f) + \left[\frac{4(v_r - v_{13f}^2)k_f k_r G_r (1-V_f)V_f}{(k_f + G_r)k_R + (k_f - k_r)G_r V_f} \right]$$. The correct equation is obtained from the

original source, Rosen and Hashin (1964).

B.1.2 SHEAR MODULI

$$G_{12} = G_{13} = G_r \left[\frac{(G_{13f} + G_r) + (G_{13f} - G_r)V_f}{(G_{13f} + G_r) - (G_{13f} - G_r)V_f} \right] \tag{B.3}$$

$$G_{23} = \frac{G_r[k_r(G_R + G_{23f}) + 2G_{23f}G_r + k_r(G_{23f} - G_r)V_f]}{k_r(G_{23f} + G_r) + 2G_{23f}G_r - (k_r + 2G_r)(G_{23f} - G_r)V_f} \tag{B.4}$$

where: $G_{23f} = \dfrac{E_{33f}}{2(1 + v_{23f})}$ \hfill (B.5)

B.1.3 POISSON'S RATIOS

$$v_{12} = v_{13} = v_{13f}V_f + v_r(1 - V_f) + \left[\frac{(v_r - v_{13f})(k_r - k_f)G_r(1 - V_f)V_f}{(k_f + G_r)k_r + (k_f - k_r)G_rV_f} \right] \tag{B.6}$$

$$v_{23} = \frac{2E_{11}k_T - E_{11}E_{22} - 4v_{13}^2 k_T E_{22}}{2E_{11}k_T} \tag{B.7}$$

In the above, k is the so-called (by Bogetti and Gillespie) 'isotropic plane strain bulk modulus' defined by:

$$k = \frac{E}{2(1 - v - 2v^2)} \tag{B.8}$$

and k_T is the effective plane strain bulk modulus of the composite defined by:

$$k_T = \frac{(k_f + G_r)k_r + (k_f - k_r)G_rV_f}{(k_f + G_r) - (k_f - k_r)V_f} \tag{B.9}$$

B.2 CALCULATION OF THERMAL AND CURE SHRINKAGE STRAINS

Ply strains in the material principal directions arising from strains of the constituent resin and

fibre are calculated from the fibre and resin·mechanical properties and strains as follows:

$$\varepsilon_1 = \frac{\varepsilon_{1f} E_{11f} V_f + \varepsilon_r E_r (1 - V_f)}{E_{11f} V_f + E_r (1 - V_f)} \qquad (B.10)$$

$$\varepsilon_2 = \varepsilon_3 = (\varepsilon_{2f} + v_{13f}\varepsilon_{1f})V_f + (\varepsilon_r + v_r\varepsilon_r)(1 - V_f)$$

$$(B.11)$$

$$- [v_{13f}V_f + v_r(1 - V_f)]\left[\frac{\varepsilon_{1f} E_{1f} V_f + \varepsilon_R E_r (1 - V_f)}{E_1 V_f + E_r (1 - V_f)} \right]$$

To calculate thermal expansion coefficients (CTE_i), replace resin and fibre strains by their

respective thermal expansion coefficients.

APPENDIX C: RESIDUAL THERMAL STRESSES IN TWO CONCENTRIC TRANSVERSELY ISOTROPIC CYLINDERS

The following equations are obtained from Wagner (1997). In this case, the fibre is transversely isotropic and the matrix is isotropic.

The strain – stress relationship for transversely isotropic materials has the following form in cylindrical coordinates,

$$
\begin{Bmatrix} \varepsilon_r \\ \varepsilon_\theta \\ \varepsilon_1 \end{Bmatrix} = \begin{bmatrix} \dfrac{1}{E_r} & -\dfrac{v_{r\theta}}{E_r} & -\dfrac{v_{1r}}{E_1} \\ -\dfrac{v_{r\theta}}{E_r} & \dfrac{1}{E_r} & -\dfrac{v_{1r}}{E_1} \\ -\dfrac{v_{1r}}{E_1} & -\dfrac{v_{1r}}{E_1} & \dfrac{1}{E_1} \end{bmatrix} \begin{Bmatrix} \sigma_r \\ \sigma_\theta \\ \sigma_1 \end{Bmatrix} + \begin{Bmatrix} \alpha_r \\ \alpha_\theta \\ \alpha_1 \end{Bmatrix} \Delta T
$$

(C.1)

where $\Delta T = (T - T_0)$ and T , T_0 are the current and initial temperatures.

The stresses in the fibre are given by

$$
\sigma_r^f = \sigma_\theta^f = A^f
$$
$$
\sigma_1^f = C^f
$$

(C.2)

where A^f and A^f are constants and the stresses on the matrix are given by

$$
\sigma_r^m = A^m + B^m (R_1 / r)^2
$$
$$
\sigma_\theta^m = A^m - B^m (R_1 / r)^2
$$
$$
\sigma_1^m = C^m
$$

(C.3)

where A^m, B^m and C^m are constants, R_1 is the fibre radius and r is any arbitrary radius on the matrix. The force balance in the longitudinal direction gives the relationship between these constants:

$$B^m = -\frac{A^m}{V_f}$$

$$A^f = -A^m \frac{V_m}{V_f}$$

$$C^f = -C^m \frac{V_m}{V_f}$$

(C.4)

Now the two unknowns A^m and C^m can be found by applying the no-slip condition at the interface and the strain/stress relationship given in Equation A.18:

$$A^m = -\frac{K_4 M_1 - K_2 M_2}{K_1 K_4 - K_2 K_3}(T - T_0)$$

$$C^m = -\frac{K_1 M_2 - K_3 M_1}{K_1 K_4 - K_2 K_3}(T - T_0)$$

(C.5)

where:

$$K_1 = 2\left(\frac{v_m}{E_m} + \frac{v_{1rf}}{E_{1f}}\frac{V_m}{V_f}\right)$$

$$K_2 = -\left(\frac{1}{E_m} + \frac{1}{E_{1f}}\frac{V_m}{V_f}\right)$$

$$K_3 = -\left(\frac{1-v_{r\theta f}}{E_m}\frac{V_m}{V_f} + \frac{1-v_m}{E_m} + \frac{1+v_m}{E_m}\frac{1}{V_f}\right)$$

(C.6)

$$K_4 = \frac{v_m}{E_m} + \frac{v_{1rf}}{E_{1f}}\frac{V_m}{V_f}$$

$$M_1 = (\alpha_{1f} - \alpha_m)$$

$$M_2 = (\alpha_{rf} - \alpha_m)$$

V_f and V_m are fibre and matrix volume fractions respectively.

APPENDIX D: TOOL-PART INTERACTION

D.1 BI-METALLIC STRIP

Consider a bi-metallic strip under a temperature change of ΔT as shown in Figure D.1. Due to the mismatch of the thermal expansion coefficient of both materials, the strip will expand and bend. But in the autoclave processing of a flat part on a tool, the bending of the tool-part combination is prevented by the application of high autoclave pressure. Hence, in this case only the expansion of the bi-metallic strip is considered. The expansion, δ, can be written as

$$\delta = \frac{(t_1 E_1 \alpha_1 + t_2 E_2 \alpha_2)\Delta T}{(t_1 E_1 + t_2 E_2)} \qquad (D.1)$$

where E is the Young's modulus, α is the coefficient of thermal expansion and t is the thickness. The normal stresses in strip 1 and 2, namely σ_1 and σ_2 respectively, are given by

$$\sigma_1 = \frac{t_2 E_1 E_2 (\alpha_2 - \alpha_1)\Delta T}{(t_1 E_1 + t_2 E_2)}$$

$$\sigma_2 = \frac{t_1 E_1 E_2 (\alpha_1 - \alpha_2)\Delta T}{(t_1 E_1 + t_2 E_2)} \qquad (D.2)$$

D.2 TOOL-PART INTERACTION DURING HEATING UP

Consider a composite part with 4 plies on an aluminum tool as shown in Figure D.2. During the heating up portion of the cure cycle, the degree of cure of the resin is very low. Hence the resin has a very low modulus. Due to the very low modulus of the resin, most of the stress due to tool-

part interaction occurs at the first ply level and it drastically reduces with distance away from the first ply. The normal stress distribution across the part thickness may be approximated by a triangular distribution with maximum stress at the bottom ply as shown in Figure D.3. This maximum stress can be calculated by assuming first ply slip as shown in Figure D.2. According to Equation D.2, by assuming a unit thickness for the tool, the maximum stress in the part will be given by

$$\sigma_1 = \frac{E_{p,i} E_t \left(\alpha_t - \alpha_{p,i} \right) \Delta T}{\left(t_{ply} E_{p,i} + E_t \right)} \tag{D.3}$$

where $E_{p,i}$ initial longitudinal modulus of the part

   E_t modulus of the tool

   $\alpha_{p,i}$ initial longitudinal coefficient of thermal expansion of the part

   α_t coefficient of thermal expansion of the tool

   t_{ply} thickness of a ply

D.3   TOOL-PART INTERACTION DURING COOLING DOWN

During the cooling down portion of the cure cycle, the resin is fully cured. Hence the resin modulus is high. Due to the high resin modulus, there is no slip between the plies and the whole part is involved in the interaction with the tool as shown in Figure D.4. Hence, the normal stress due to the tool part interaction is constant through the part thickness (Figure D.5). The normal stress in the part will be given by

$$\sigma_2 = \frac{E_{p,f} E_t \left(\alpha_t - \alpha_{p,f} \right) \Delta T}{\left(t_{lam} E_{p,f} + E_t \right)} \tag{D.4}$$

where $E_{p,f}$ final longitudinal modulus of the part

   $\alpha_{p,f}$ final longitudinal coefficient of thermal expansion of the part

t_{lam} thickness of the part

D.4   TOOL REMOVAL

Upon removal of the tool, the resultant normal stress in the part can be calculated by adding σ_1 and σ_2 as shown in figure D.6. The part warps due to this resultant stress. The moment that causes the part to warp is given by

$$M = F(\frac{t_{lam}}{2} - Z) \tag{D.5}$$

where F is the resultant force and Z is the lever arm and given by

$$F = \frac{t_{lam}}{2}(2\sigma_2 - \sigma_1)$$
$$Z = \frac{t_{lam}}{3}(3\sigma_2 - 2\sigma_1) \tag{D.6}$$

The warpage of the part can be calculated from the moment-curvature relationship

$$\frac{d^2w}{dx^2} = \frac{M}{EI} \tag{D.7}$$

D.5 FIGURES
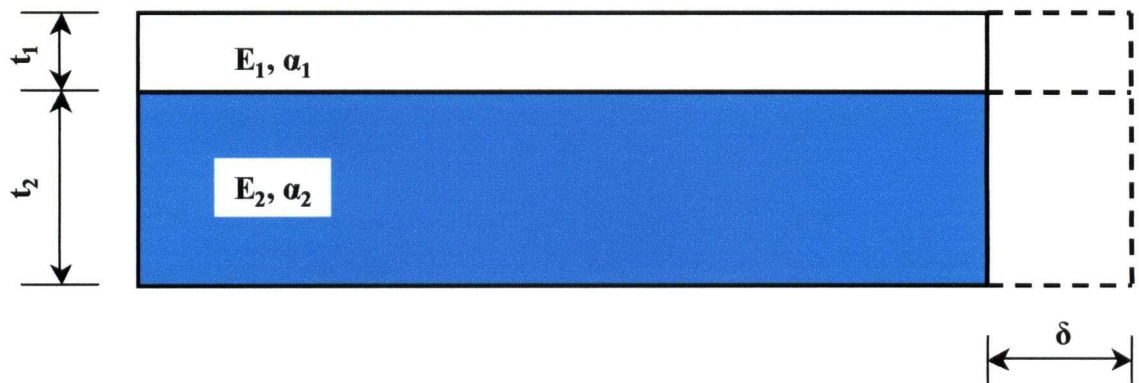
Figure D. 1 Bi-metallic strip under temperature change, ΔT.
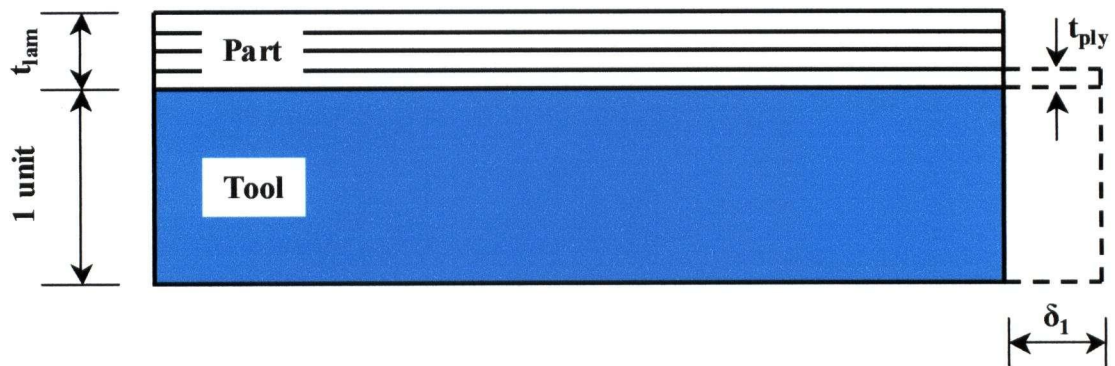

Figure D. 2 First ply slip during the initial stage of curing process (heating up). The resin is not cured and it has very low modulus.
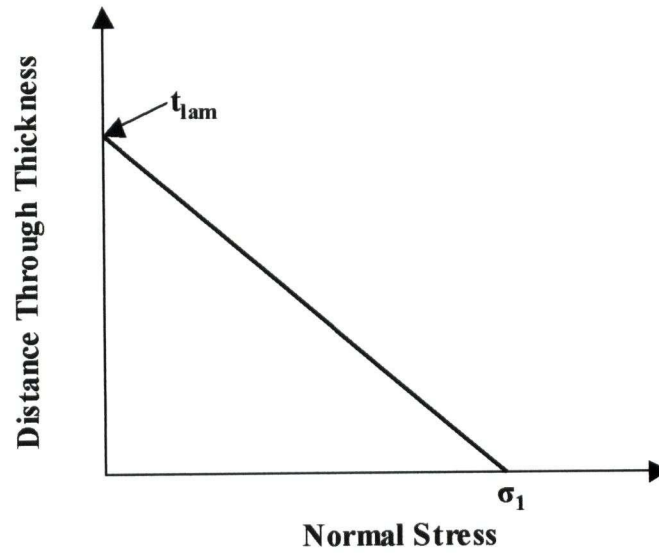
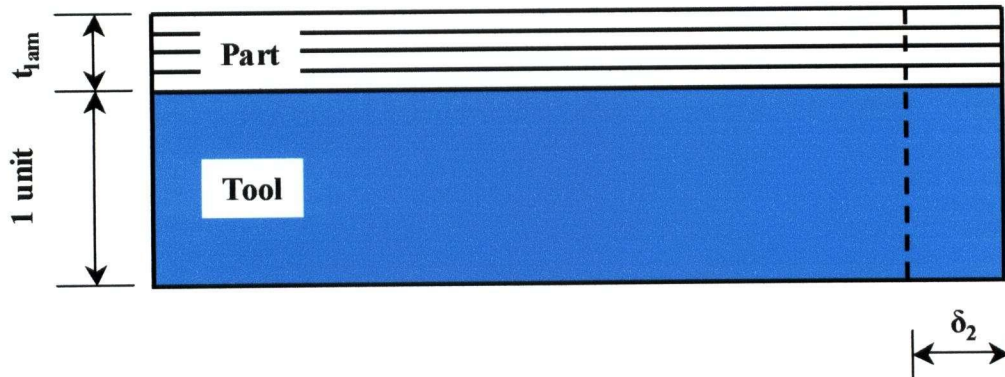**Figure D. 3 The normal stress distribution through part thickness during heating up.**

Figure D. 4 Tool-part interaction at the final stage of the curing process (cooling down). The resin is fully cured and it has high modulus. The entire part is moved with the tool.
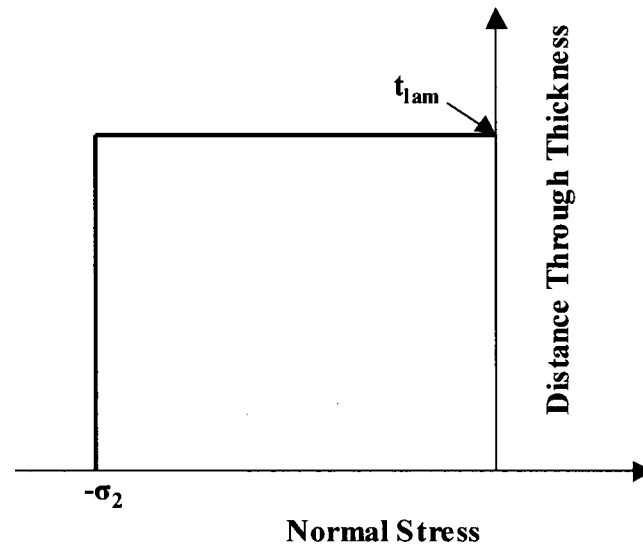
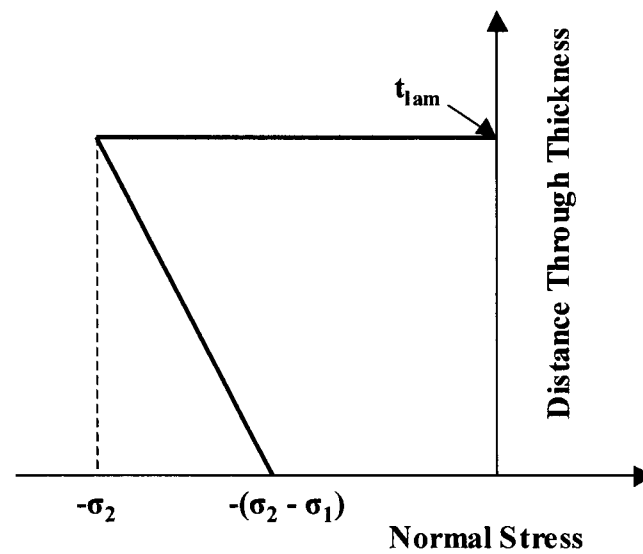**Figure D. 5 The normal stress distribution through part thickness during cooling down.**

Figure D. 6 Resultant normal stress distribution through part thickness.